

MODELING OF SCRAP HEATING BY BURNERS

MODELING OF SCRAP HEATING BY BURNERS

BY

KAMALESH MANDAL, M. TECH, IIT KANPUR, B.MET.E., JADAVPUR UNIVERSITY, INDIA

A Thesis
Submitted to the School of Graduate Studies
in Partial Fulfillment of the Requirements for the Degree of
Doctor of Philosophy

MCMASTER UNIVERSITY
© Copyright by Kamalesh Mandal, June 2010

DOCTOR OF PHILOSOPHY (2010)
Department of Materials Science and Engineering
McMaster University
Hamilton, Ontario
Canada

Title: MODELING OF SCRAP HEATING BY BURNERS
Author: Kamalesh Mandal, M. Tech (IIT Kanpur), B. Met. E. (Jadavpur
University), India
Supervisor: Professor Gordon A. Irons
Number of Pages: xxiv, 184

Abstract

The efficiency and productivity of Electric Arc Furnace steelmaking has improved with a number of new technologies. One of these is the use of oxy-fuel burners to assist the electric heating. Initially burners were just used to melt the scrap at the slag door where arc heating is inefficient. At present virtually all modern EAF use oxy-fuels burners to decrease electric energy consumption and increase productivity. Despite the impressive performance of these burners there is little information on the efficiency of the heat transfer between the combustion gas and the steel scrap in the furnace. The purpose of this research was to measure and model the heating efficiency for a range of scrap types. The ultimate goal of this study is to assist operators with the selection of energy inputs and scrap grades from different sources, so as to optimize the operation.

Experimentally, steel scrap heating phenomena were studied using an oxy-fuel burner in a small scale furnace (1m^3) for a range of burner power, scrap type and furnace configuration.

An in-house computer model was developed, considering non-uniform porosity inside the furnace, turbulence, dynamic behavior of porosity due to localized melting. The model was tuned using the experimental data of scrap heating by oxy-fuel burners in a small-scale furnace (1 m^3). Due to lack of literature of

porous media fluid flow and heat transfer for irregular shaped particles and complexity of the problem a detail analysis and considerations of the model parameters e.g., porosity variation inside the furnace, permeability of the bed, drag coefficient of the bed, effective thermal conductivity of the bed, fluid to solid heat transfer coefficient and radiation inside the bed, were performed. Model parameters were dependent upon porosity of the bed and characteristic particle diameter. Sensitivity analysis was performed to study the effectiveness of heating with model parameters. Measured porosity variations were used for numerical simulation and characteristic particle diameter for different scrap was tuned to match the experimental results with numerical simulation. Thermocouple temperatures were also modeled since it was between the gas and solid temperatures. Using tuned characteristic particle diameter simulations were performed for different scrap with different furnace configuration.

Experimental and numerical modeling results were used to analyze heat transfer and fluid flow phenomena during scrap heating by burners. This appears to be the first time a numerical model for heat transfer between flame and scrap was developed and validated with experimental data.

Acknowledgements

I express deep sense of gratitude and sincere thanks to Professor Gordon A. Irons, for his guidance, valuable suggestions, remarkable patience and constant encouragement throughout the course of this study.

I would like to thank the members of my supervisory committee, Professor Ken Coley and Professor Marilyn F. Lightstone for their comments and suggestions at different stages of this research.

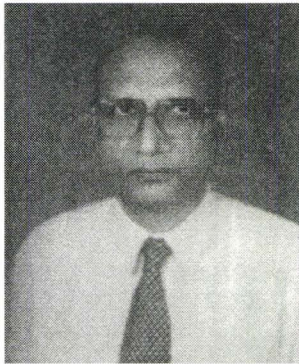
I would like to thank Dr. Guo, Mr. Own Kelly and Dr. Ji for their help during the experiments.

I truly appreciate the great help from my friends. Specially, I owe thanks to Kumar Krishnashapirody and Ho Young Hwang for their suggestions and ideas during this study. Also, I would like to thank my friends Basab Bhattacharya, Rahul Das, Judy Li, Fernando Guevara and Kevin Graham for creating wonderful environment. Also, thanks to JHE A304 residents.

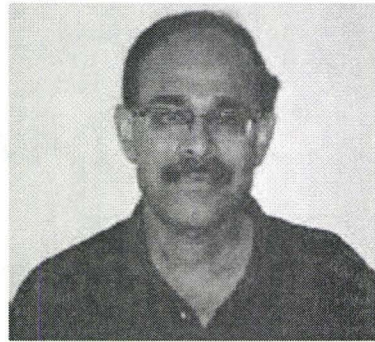
I could not have reached this stage in my life without the sacrifice and constant encouragement from my family.

To my Teachers

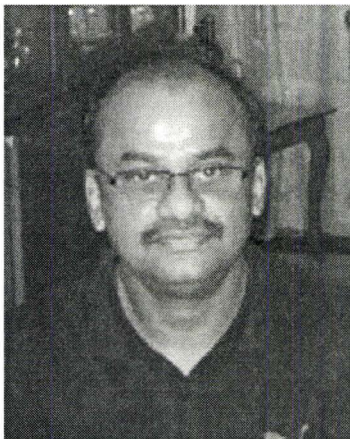
Professor Ahindra Ghosh



Professor Dipak Mazumdar



Dr. Biswajit Basu



Professor Gordon A. Irons

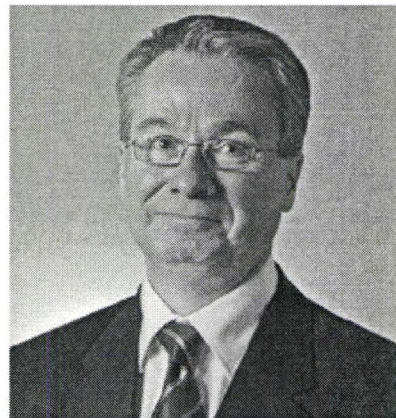


Table of Contents

Abstract	iii
Acknowledgements	v
List of Figures	x
List of Tables	xx
List of Symbols	xxi
Chapter 1 Introduction and Objectives	1
1.1 Steelmaking Processes.....	1
1.2 Basic Oxygen Furnace Steelmaking (BOF Steelmaking).....	4
1.3 Electric Arc Furnace Steelmaking (EAF Steelmaking).....	6
1.4 Electric Arc Furnace Materials and Energy Balance.....	10
1.5 Preheating – A Literature Review.....	13
1.5.1 Scrap Preheater.....	13
1.5.2 The Fuchs Shaft Furnace.....	15
1.5.3 Nippon Steel Shaft Type Preheating System UL-BA (Ultimate Batch System).....	16
1.5.4 Twin Shell Electric Arc Furnace.....	21
1.5.5 Consteel.....	22
1.6 Problems During Scrap Preheating.....	23
1.7 Objectives and Overall Structure – of the Present Study.....	26
1.7.1 Objectives.....	26
1.7.2 Overall Structure of the Present Research.....	26
Chapter 2 Experimental	28
2.1 Introduction.....	28
2.2 Furnace Design.....	28
2.3 Ancillary Equipment.....	31

Table of Contents (Continued)

2.3.1 Burner.....	31
2.3.2 Thermocouples and Data Acquisition System	34
2.3.3 Gas Analyzer.....	37
2.4 Materials.....	38
2.5 Measurements.....	39
2.5.1 Scrap size and density measurements	39
2.5.2 Porosity measurements	41
2.5.3 Experiments to determine the extent of combustion	50
2.5.4 Scrap Heating Experiments	56
2.6 Experimental Results and Discussion.....	57
2.7 Summary of Scrap Heating Experiments.....	70
Chapter 3 Numerical Modeling	73
3.1 Introduction.....	73
3.2 Porous Media Flow and Heat Transfer – Literature Review.....	74
3.2.1 Porous Media Flow Models.....	75
3.2.2 Turbulence Modeling in Porous Media.....	84
3.2.3 Porous Media Thermal Model.....	88
3.3 Model Equations.....	90
3.4 Model Parameters.....	97
3.4.1 Porosity.....	97
3.4.2 Permeability, K and Drag Coefficient, F	101
3.4.3 Effective Thermal Conductivity.....	104
3.4.4 Fluid to Solid Heat Transfer Coefficient, h_{fs} and Specific Surface area A_s	107
3.4.5 Radiation.....	110

Table of Contents (Continued)

3.5	Numerical Solution Procedure.....	114
3.6	The Computer Program.....	116
3.7	Evaluation of Computational Procedure.....	119
3.8	Boundary Conditions.....	120
3.8.1	Fluid Flow and Turbulence.....	120
3.8.2	Temperature.....	120
3.9	Tuning and Validation of Numerical Model.....	122
3.10	Simulation Results and Discussion.....	134
3.11	Sensitivity Analysis of Burner Efficiency.....	144
3.11.1	Sensitivity of Burner Efficiency on Porosity and Characteristic Particle Diameter.....	144
3.11.2	Sensitivity of Burner Efficiency on Scrap Distribution inside the Furnace	147
3.11.3	Sensitivity of Burner Efficiency on Radiation.....	151
3.11.4	Sensitivity of Burner Efficiency on Turbulence	152
Chapter 4	Conclusions	153
Appendix A	CO₂ Adsorption/Elution Phenomena by Different Drying Agents	158
Appendix B	Tri-Diagonal Matrix Algorithm (TDMA)	167
Appendix C	Partial Elimination Algorithm (PEA)	169
Appendix D	Assessments of Computational Procedure	171
References		177

List of Figures

Figure	Figure Caption	Page
1.1	World Steel Production by Processes (Steel Statistical Yearbook, IISI, 2007)	1
1.2	Flowchart of a modern steelmaking operation (www.postech.ac.kr/dept/mse/cml/Kor/flowchart1.htm)	2
1.3	Operational steps of BOF Steelmaking (The Making, Shaping and Treating of Steel, 11 th Edition, 1998)	5
1.4	Several components of Electric Arc Furnace (The Making, Shaping and Treating of Steel, 11 th Edition, 1998)	7
1.5	Electric Arc Furnace operation sequence, a) Scrap Charging, b) Heating, c) Refining and d) Tapping (steeluniversity.org)	10
1.6	Schematic of Scrap Preheater for an EAF (Rudzki et al., 1973)	14
1.7	Schematic of Fuchs Shaft Furnace (Clayton, 1993)	16
1.8	Schematic of Nippon Steel Corporation UL-BA (Nakano et al., 1999)	17
1.9	Outline of the pilot plant, UL-BA (Nakano et al., 1999)	17
1.10	Scrap temperature with heating time (#2 heavy scrap) (Nakano et al., 1999)	19
1.11	Schematic of Twin Shell EAF at Nippon Steel (The Making Shaping and Treating of Steel, 11 th Edition, 1998)	22
1.12	Components of CONSTEEL process (The Making, Shaping and Treating of Steel, 11 th Edition, 1998)	23
1.13	Overall Structure of the Research	27
2.1	A schematic of present Area of Research Interest	29

Figure	Figure Caption	Page
2.2	A Picture of Scrap Heating Furnace	30
2.3	A Schematic View of the Scrap Heating Furnace (mm) (not to scale)	31
2.4	A Schematic of the Burner used for Scrap Heating (mm) (not to scale)	33
2.5	Burner used for heating	33
2.6	Thermocouples arrangement of the Scrap Heating Furnace (Centerline), mm (Not to scale)	36
2.7	Data acquisition system (View from the thermocouple side)	36
2.8	HORIBA VIA-510 general purpose gas analyzer	38
2.9	Size Distribution of Small Shredded Scrap	40
2.10	Size Distribution of Large Shredded Scrap	41
2.11	Plexiglass porosity measurement vessel	44
2.12	Segments in a) Y direction, b) Z direction and c) X direction	45
2.13	Porosity variations from the wall to the center for small shredded scrap (average scrap length 80 mm) in X-direction	46
2.14	Porosity variation from the wall to the center for small shredded scrap (average scrap length 80 mm) in Y-direction	46
2.15	Porosity variation from the wall to the center for small shredded scrap (average scrap length 80 mm) in Z-direction	47
2.16	Porosity variation from the wall to the center for large shredded scrap (average scrap length 150 mm) in Y-direction	47
2.17	Porosity variation from the wall to the center for Busheling in Y-direction	48

Figure	Figure Caption	Page
2.18	Porosity variation from the wall to the center for small spherical particles (diameter~63mm) in Y-direction	49
2.19	Porosity variation from the wall to the center for large spherical particles (diameter~195mm) in Y-direction	49
2.20	A schematic of the off gas analysis Experimental Set-up	51
2.21	Gas sampling positions in the cross section of the center of the furnace	51
2.22	Oxygen percentage inside the furnace in different positions	53
2.23	Percent of combustion for different propane and oxygen flow rate	54
2.24a	Temperature (°C) contour of the furnace after 30 minutes of the experiment with Large Shredded Scrap with top cover on, Burner Power 17.3 kW	57
2.24b	Temperature (°C) contour of the furnace after 60 minutes of the experiment with Large Shredded Scrap with top cover on, Burner Power 17.3 kW	58
2.24c	Temperature (°C) contour of the furnace after 90 minutes of the experiment with Large Shredded Scrap with top cover on, Burner Power 17.3kW	58
2.25a	Temperature (°C) contour of the furnace after 60 minutes of the experiment with Large Shredded Scrap with top cover on, Burner Power 8.3 kW	59
2.25b	Temperature (°C) contour of the furnace after 60 minutes of the experiment with Large Shredded Scrap with top cover on, Burner Power 12.8 kW	59
2.26a	Temperature (°C) contour of the furnace after 90 minutes of the experiment with Small Shredded Scrap with top cover on, Burner Power 12.8 kW	60

Figure	Figure Caption	Page
2.26b	Temperature (°C) contour of the furnace after 90 minutes of the experiment with Small Shredded Scrap with top cover off, Burner Power 12.8 kW	61
2.27a	Temperature (°C) contour of the furnace after 60 minutes of the experiment with Small Shredded Scrap, top cover on, Burner Power 12.8 kW	62
2.27b	Temperature (°C) contour of the furnace after 60 minutes of the experiment with Large Shredded Scrap, top cover on, Burner Power 12.8 kW	62
2.27c	Temperature (°C) contour of the furnace after 60 minutes of the experiment with Heavy Melt, top cover on, Burner Power 12.8 kW	63
2.28	Plot of Exhaust Gas Temperature and Apparent Efficiency with heating time for Shredded (Small and Large) and Heavy Melt, Burner Power 12.8kW	63
2.29	Sheet metal layer position during the experiment	64
2.30a	Temperature (°C) contour of the furnace after 60 minutes of the experiment with Small Shredded scrap, top cover on, Burner Power 12.8 kW	65
2.30b	Temperature (°C) contour of the furnace after 60 minutes of the experiment with small Shredded scrap and sheet metal layer, top cover on, Burner Power 12.8 kW	65
2.31	Plot of exhaust gas temperature and apparent efficiency with heating time, small shredded scrap, with sheet metal addition and without sheet metal addition, Burner Power 12.8 kW	66
2.32	Scrap layering during the experiment	67
2.33a	Temperature (°C) contour of the furnace after 30 minutes of the experiment with Scrap Layers, top cover on, Burner Power 12.8 kW	67

Figure	Figure Caption	Page
2.33b	Temperature (°C) contour of the furnace after 60 minutes of the experiment with scrap layers, top cover on, Burner Power 12.8 kW	68
2.33c	Temperature (°C) contour of the furnace after 90 minutes of the experiment with Scrap Layers, top cover on, Burner Power 12.8 kW	68
2.34	Exit gas temperature Vs time for test 1 and test two with small shredded scrap, top cover on, Burner Power 8.3 kW	69
2.35	Summary of temperature deviation between test 1 and test 2 with small shredded scrap, top cover on, Burner Power 8.3kW	70
3.1	Experimental porosity variation from the wall to the center of the furnace for small shredded scrap	98
3.2	Experimental porosity variation from the wall to the center of the furnace for large shredded scrap	99
3.3	Experimental porosity variation from the wall to the center of the furnace for small shredded scrap and exponential decay function of porosity variation from the wall to the center of the furnace	100
3.4	Experimental porosity variation from the wall to the center of the furnace for large shredded scrap and exponential decay function of porosity variation from the wall to the center of the furnace	100
3.5	Variation of Permeability with Porosity ($d_p=0.05m$) and Particle Characteristic Diameter (Porosity = 0.5) of the particle	102
3.6	Variation of Geometric Factor, F with Porosity	103
3.7	Plot of fluid effective thermal conductivity with particle Reynold's number ($K_f=0.022$). The models are shown in Table 3.3	106
3.8	Fluid effective thermal conductivity with porosity ($K_f=0.022$). The Models are shown in Table 3.3.	106

Figure	Figure Caption	Page
3.9	Fluid effective thermal conductivity with particle diameter ($K_f=0.022$). The models are shown in Table 3.3.	107
3.10	Correlation of Nusselt numbers with Re and Pr (Wakao et al. 1979)	108
3.11	The sequential steps of the computer program	118
3.12	Cross section in X-X direction (mm)	124
3.13	Temperature ($^{\circ}C$) contour of the furnace after 30 minutes of the experiment with Shredded Small Scrap, Power=8.3 kW, Furnace lid on, a=Measured thermocouple temperatures, b=Predicted gas temperatures	125
3.14	Temperature ($^{\circ}C$) contour of the furnace after 60 minutes of the experiment with Shredded Small Scrap, Power=8.3 kW, Furnace lid on, a=measured thermocouple temperatures, b=predicted gas temperatures	126
3.15	Numerically predicted gas and scrap temperatures, predicted thermocouple temperatures and measured thermocouple temperatures with time of heating for point 1 (Shown in Figure 3.12).	128
3.16	Numerically predicted gas and scrap temperatures, predicted thermocouple temperatures and measured thermocouple temperatures with time of heating for point 2 (Shown in Figure 3.12).	129
3.17	Numerically predicted gas and scrap temperatures, predicted thermocouple temperatures and measured thermocouple temperatures with time of heating for point 12 (Shown in Figure 3.12).	129
3.18	Numerically predicted gas and scrap temperatures, predicted thermocouple temperatures and measured thermocouple temperatures with time of heating for point 14 (Shown in Figure 3.12).	130

Figure	Figure Caption	Page
3.19	Summary of deviation between predicted thermocouple temperatures and measured thermocouple temperatures for all points, shown in Figure 3.12.	130
3.20	Summary of deviation between predicted thermocouple temperatures and measured thermocouple temperatures for all points, shown in Figure 3.12 (Large shredded scrap, Burner power=8.3kW).	131
3.21	Summary of deviation between predicted thermocouple temperatures and measured thermocouple temperatures for all points, shown in Figure 3.12 (Busheling, Burner power=8.3kW).	131
3.22	Summary of deviation between predicted thermocouple temperatures and measured thermocouple temperatures for all points, shown in Figure 3.12 (Small Shredded scrap, Large shredded scrap and Busheling, Burner power=8.3kW).	132
3.23	Effect of emissivity on modeled thermocouple temperature.	133
3.24	Effect of heat transfer coefficient on modeled thermocouple temperature.	133
3.25	Heating efficiency of the burner, Power = 8.3 kW, Small Shredded Scrap.	134
3.26	Temperature (°C) contour of the furnace after 30 minutes of the experiment with Small Shredded Scrap, Power=12.8 kW, Furnace lid on, a=Measured thermocouple temperatures, b=Predicted thermocouple temperatures	136
3.27	Temperature (°C) contour of the furnace after 60 minutes of the experiment with Small Shredded Scrap, Power=12.8 kW, Furnace lid on, a=Measured thermocouple temperatures, b=Predicted thermocouple temperatures	137
3.28	Temperature (°C) contour of the furnace after 30 minutes of the experiment with Small Shredded Scrap, Power=17.3 kW, Furnace lid on, a=Measured thermocouple temperatures, b=Predicted thermocouple temperatures	138

Figure	Figure Caption	Page
3.29	Heating efficiency of small shredded scrap using burner power 8.3kW, 12.8kW and 17.3 kW	139
3.30	Temperature (°C) contour of the furnace after 60 minutes of the experiment with Large Shredded Scrap, Power=8.3 kW, Furnace lid on	140
3.31	Heating efficiency of small shredded scrap, larger shredded scrap, busheling, sheet metal additions and layers of busheling, small shredded, large shredded and heavy melt. Burner Power: 8.3 kW	141
3.32	Picture in front of the burner after a) 35 seconds of heating and b) 90 seconds of heating	142
3.33	Modeled scrap temperature with heating time at thermocouple number one and thermocouple number two. Small Shredded Scrap and Burner Power: 12.8 kW	143
3.34	Heating efficiency of burner for Small Shredded Scrap, With Scrap melting and without scrap melting, Burner Power = 12.8kW, Porosity = Measured Value	143
3.35	Heating efficiency of the burner for different characteristic particle diameter, Burner Power = 12.8kW, Porosity = Measured Value, Small Shredded Scrap.	145
3.36	Heating efficiency of the burner for different porosity, Power = 12.8kW, $d_p = 0.027$ m, Small Shredded Scrap.	145
3.37	Vector plot and temperature contour after 60 minutes of heating, Power = 12.8kW, Porosity = Measured Value.	148
3.38	Heating efficiency of burner for Small Shredded Scrap (uniform distribution of scrap and flame blocking by scrap), Burner Power = 12.8kW, Porosity = Measured Value.	149
3.39	Heating efficiency of burner for Small Shredded Scrap, with different porosity of the furnace, Power = 12.8kW.	149

Figure	Figure Caption	Page
3.40	Vector plot and temperature contour after 60 minutes of heating, Burner Power = 12.8kW, Porosity = Measured Value, A solid scrap in the middle of the furnace.	150
3.41	Heating efficiency of burner for Small Shredded Scrap (uniform distribution of scrap and a solid scrap in the middle of the furnace), Burner Power = 12.8kW, Porosity = Measured Value.	150
3.42	Heating efficiency of small shredded scrap using burner power 12.8kW considering radiation and without radiation	151
3.43	Heating efficiency of small shredded scrap using burner power 12.8kW considering extra turbulence due to porous media and without extra turbulence	152
A1	Experimental Setup for CO ₂ measurement error analysis	161
A2	Response time for the anhydrous drying agents to CO ₂ adsorption from a gas mixture of 25% CO ₂ and 75% N ₂ . The gas flow rate 1.6 l/m and the mass of the drying agents 105 gm for H/D of 17	162
A3	Response time for the anhydrous drying agents to CO ₂ elution from a gas mixture of 25% CO ₂ and 75% N ₂ , The N ₂ flow rate was 1.6 l/m and the mass of the drying agent was 105 gm for H/D of 17	162
A4	Response time for anhydrous silica gel for different height-to-diameter ratios on CO ₂ adsorption from a gas mixture of 25% CO ₂ and 75% N ₂ . The gas flow rate was 1.6 l/m and the mass of the drying agent was 105 gm	163
A5	The response time for anhydrous Silica Gel for gas flow rates 0.8, 1.6 and 3.2 l/m to CO ₂ adsorption from a gas mixture of 25% CO ₂ and 75% N ₂ , for a mass of 105 gm	164
A6	Percent of response time for hydrous silica gel, on CO ₂ adsorption from a gas mixture of 25% CO ₂ and 75% N ₂ , gas flow rate 1.6 l/m mass of the silica gel is 105.00 gm	165

Figure	Figure Caption	Page
D1	Cubic cavity (a=1 m) used for computational domain	172
D2	Comparison of present numerical predictions of horizontal velocity component, u , along the center vertical line, Y , with those computed by FLUENT for steady laminar flow in a cubic cavity	172
D3	Comparison of present numerical predictions of vertical velocity component, v , along the center horizontal line, X , with those computed by FLUENT for steady laminar flow in a cubic cavity	173
D4	Comparison of present numerical predictions of horizontal velocity component, u , along the center vertical line, Y , with those computed by FLUENT 6.0 for steady turbulent flow in a cubic cavity	174
D5	Calculated Temperature field from Present Model and FLUENT	175
D6	Central Horizontal Distance, X Vs Temperature	175

List of Tables

Table	Table Caption	Page
1.1	Typical pig iron composition in % (Ghosh and Chatterjee, 2008)	3
1.2	Typical Materials Balance for EAF (Camdali and Tunc, 2002)	11
1.3	Typical Energy Balance for Modern Electric Arc Furnace (The Making, Shaping and Treating of Steel, 11 th Edition, 1998)	12
2.1	Temperature coefficients, temperature range, voltage range and error range for B type thermocouples	35
2.2	Temperature coefficients, temperature range, voltage range and error range for K type thermocouples	35
2.3	Scrap Characteristics	39
2.4	Propane and oxygen flow rates with corresponding burner power (FactSage5.5., 2007)	55
3.1	Turbulence Models (Versteeg and Malalasekera, 2007)	85
3.2	Comparison of a , b and L_c for spherical shaped particles, large shredded scrap and small shredded scrap	99
3.3	Summary of different models for K_{eff}	105
3.4	Summary of different models for h_{fs}	109
3.5	Experimental Conditions and Tuned Parameters	123
3.6	Quantitative values of K , F and h_{fs} for small shredded scrap with different characteristic particle diameter and porosity ($P_r=0.688$)	147
D1	Properties of working fluid for natural convection study	176

List of Symbols

Abbreviations

R_{eP}	<i>Pore Reynolds number</i>
Re	<i>Reynolds number</i>
Gr	<i>Grashof Number</i>
N_u	<i>Nusselt Number</i>
Pr	<i>Prandtl Number</i>
Ra	<i>Rayleigh Number</i>

Subscript

f	<i>Fluid</i>
m	<i>mixture</i>
s	<i>Solid</i>
i	<i>Vector notation for u, v and w</i>
j	<i>Coordinates $x, y,$ and z</i>

Greek

α_s	<i>Heat transfer coefficient (1.9)</i>
β	<i>Thermal expansion coefficient (3.7)</i>
ϕ	<i>Local porosity</i>
ϕ_∞	<i>Porosity from the far away from the boundary or wall</i>
σ	<i>Stefan Boltzmann Constant (1.9)</i>
σ_k	<i>k-ϵ Model constant (3.9)</i>
σ_ϵ	<i>k-ϵ Model constant (3.10)</i>
ρ	<i>Fluid density (3.1)</i>
ϵ	<i>Dissipation rate of turbulent kinetic energy (3.10)</i>

η_{SC}	<i>Scrap preheating efficiency (1.9)</i>
η_{app}	<i>Apparent efficiency</i>
μ	<i>Fluid viscosity (3.3)</i>
μ_{eff}	<i>Effective fluid viscosity (3.3)</i>
μ_i	<i>Laminar fluid viscosity (3.3)</i>
μ_T	<i>Turbulent fluid viscosity (3.8)</i>
ν_f	<i>Kinematic viscosity of the fluid</i>
ΔP	<i>Pressure gradient (3.3)</i>
ΔT	<i>Temperature difference between the local and reference temperatures (3.7)</i>
ΔT_W	<i>Temperature difference of water (1.7)</i>
ΔT_R	<i>Temperature difference of refractory (1.8)</i>
Δx	<i>Control volume length in x- direction</i>
Δy	<i>Control volume length in y- direction</i>
Δz	<i>Control volume length in z- direction</i>

Roman

<i>a</i>	<i>Parameter (page 42)</i>
<i>a_f</i>	<i>Fraction of area available for flow per unit cross sectional area (3.16, 3.17, 3.18)</i>
<i>b</i>	<i>Parameter (page 42)</i>
<i>A_S</i>	<i>Surface area (1.11, 3.14)</i>
<i>C</i>	<i>Specific heat (3.13)</i>
<i>C_{P(gas)}</i>	<i>Specific heat of gas (1.6)</i>
<i>C_{P(W)}</i>	<i>Specific heat of water (1.7)</i>
<i>C_{P(R)}</i>	<i>Specific heat of refractory (1.8)</i>
<i>C_μ</i>	<i>k-ε Model constant</i>
<i>C_k</i>	<i>Porous media k-ε model constant (page 85)</i>
<i>d_P</i>	<i>Particle diameter</i>

E	Emissivity (1.9, page 111)
F	Drag coefficient or Geometric factor (3.6)
g	Acceleration due to gravity (3.1)
g	Acceleration due to gravity in y -direction (3.23)
G_K	Volumetric rate of turbulent production
h_v	Volumetric heat transfer coefficient (page 108)
h_{fs}	Heat transfer coefficient between fluid and solid (1.11, 3.14)
K	Permeability (3.3)
K_{eff}	Effective thermal conductivity (3.13)
K_s	Thermal conductivity of solid (page 86)
K_r	Radiative conductivity
K_f	Thermal conductivity of fluid (page 86, 104)
K_{feff}	Effective thermal conductivity of fluid (3.14)
K_{seff}	Effective thermal conductivity of solid (3.15)
k	Turbulent kinetic energy
L	Characteristic length (3.22)
q^r	Heat flux due to radiation (3.15)
Q_{SC}	Heat storage to the scrap (1.4)
Q_{gas_in}	Sensible heat of inlet gas (1.5)
$Q_{gas-out}$	Sensible heat of exhaust gas (1.6)
Q_W	Heat loss to the cooling water (1.7)
Q_R	Heat storage to the refractory (1.8)
Q_r	Diffused heat into the air (1.9)
S_K	Source term in turbulent kinetic energy equation (3.9)
S_ϵ	Source term in the dissipation rate of turbulent kinetic energy equation (3.10)
t	Time
T_{Sur}	Surrounding temperature (1.9)
T_O	Reference temperature (1.9)
T_S	Solid temperature (3.14)

T_f	<i>Fluid temperature (3.14)</i>
T_{flame}	<i>Flame temperature</i>
$T_{exhaust}$	<i>Exhaust gas temperature</i>
$T_{ambient}$	<i>Ambient temperature</i>
T_{gas}	<i>Gas temperature (1.11)</i>
T_{SC}	<i>Scrap temperature (1.11)</i>
T_{gas-in}	<i>Temperature of inlet gas (1.5)</i>
$T_{gas-out}$	<i>Temperature of outlet gas (1.6)</i>
u'	<i>Fluctuating component of fluid velocities</i>
u	<i>Volume averaged fluid velocity in x-direction</i>
u_f	<i>Fluid velocity in x-direction</i>
v	<i>Volume averaged fluid velocity in y-direction</i>
v_f	<i>Fluid velocity in y-direction</i>
V	<i>Fluid velocity (3.1)</i>
V_d	<i>Darcy velocity</i>
V_P	<i>Pore velocity</i>
V_{gas-in}	<i>Volume of inlet gas (1.5)</i>
$V_{gas-out}$	<i>Volume of outlet gas (1.6)</i>
V_W	<i>Volume of water (1.7, 2.6)</i>
V_R	<i>Volume of refractory (1.8)</i>
V_S	<i>Volume of scrap (1.11, 2.6)</i>
w	<i>Volume averaged fluid velocity in z-direction</i>
w_f	<i>Fluid velocity in z-direction</i>
x	<i>Distance from the wall (page 42)</i>

Chapter 1

Introduction and Objectives

1.1 Steelmaking Processes

Due to the wide range of alloy composition, properties and available forms of product, steel is a versatile material. In recent years the world steel industry has entered in a new era. Over the past six years, world finished steel consumption has risen by an average of 6.5%, annually (IISI, 2007a). Figure 1.1 shows the world crude steel production over the last few decades by different steelmaking processes. It is evident from Figure 1.1 that world crude steel production has grown considerably over the past few decades.

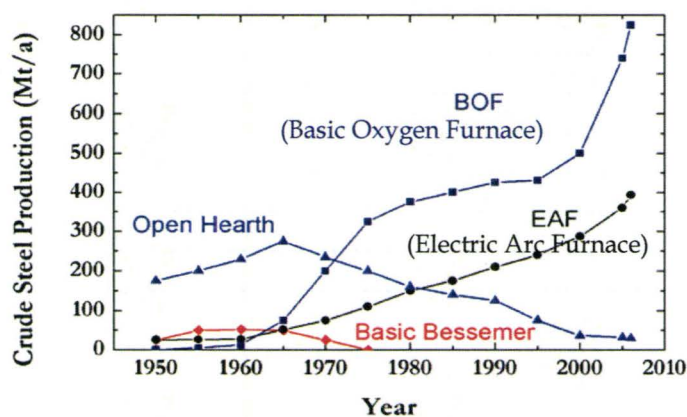


Figure 1.1: World Steel Production by Processes (IISI, 2007b)

It is seen from Figure 1.1, currently there are mainly two different methods of producing steel. One is Basic Oxygen Furnace (BOF) steelmaking, i.e., integrated steelmaking, which has liquid ironmaking capability from iron ore as well as steelmaking capability. The other is Electric Arc Furnace (EAF) steelmaking, which is a scrap based process. Figure 1.2 shows the flowchart of a modern steelmaking operation. The major operations to produce finished steel from the raw materials are summarized below;

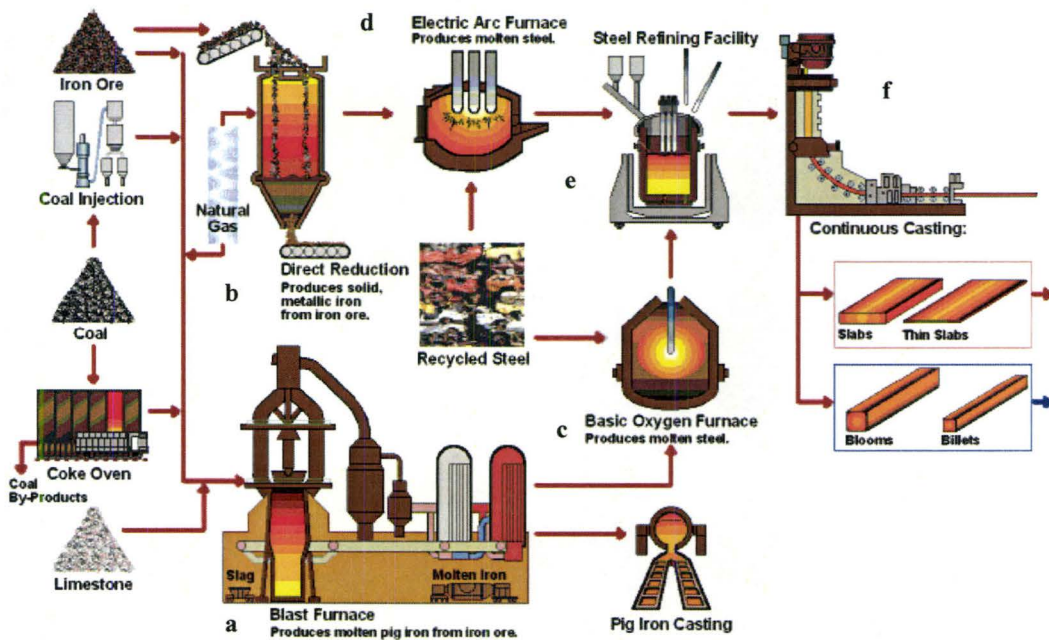


Figure 1.2: Flowchart of a modern steelmaking operation
 (www.postech.ac.kr/dept/mse/cml/Eng/flowchart1.htm)

Ironmaking: Iron can be produced either liquid state (Figure 1.2 - a) or solid state (Figure 1.2 - b). The blast furnace is the main reactor where liquid iron or “pig iron” is produced using iron ore, coke and limestone. Pig iron contains about 4% carbon, and some amount of silicon, manganese, sulfur and phosphorous. A typical pig iron composition is shown in Table 1.1. Iron produced as a solid by the reduction of iron ore (lumps or pellets) is known as sponge iron or Direct Reduced Iron (DRI). Carbon percentage of DRI varies over a wide range (0.1 – 2.5%) depending upon the process.

Table 1.1: Typical pig iron composition in % (Ghosh and Chatterjee, 2008)

	Japan	Europe	USA	India
Carbon	4.0-4.5	4.0-4.5	4.0-4.5	4.0-4.5
Silicon	0.30-0.45	0.30-0.45	0.40-0.70	0.70-1.30
Manganese	0.20-0.40	0.20-0.65	0.50-0.75	0.04-0.10
Phosphorus	0.095-0.105	0.060-1.50	0.04-0.08	0.10-0.30
Sulphur	0.02-0.025	0.02-0.04	0.025-0.065	0.055-0.080

Steelmaking: Steel can be produced either in the BOF process or in the EAF process. In BOF steelmaking (Figure 1.2 - c), pig iron is refined to produce steel. In this process impurities in pig iron e.g., carbon, silicon, manganese, are reduced to a desired level using pure oxygen blowing into the liquid iron. In EAF (Figure 1.2 - d) steelmaking, recyclable steel scrap and sometimes solid iron, are melted and refined using oxygen blowing to produce steel. The above described BOF and EAF steelmaking processes

are known as primary steelmaking. After primary steelmaking liquid steel is then tapped into a cylindrical shaped vessel called a ladle. In the ladle, liquid steel is further processed to obtain final composition and temperature (Figure 1.2 - e), which is called secondary steelmaking.

Continuous Casting: Finally, the liquid steel is then continuously cast into slabs, blooms or billets (Figure 1.2 - f).

1.2 Basic Oxygen Furnace Steelmaking (BOF Steelmaking)

The Basic Oxygen Furnace is the key unit for producing steel, and produces about 66% of total world steel production (IISI, 2007b). In this process liquid pig iron and some amount of scrap (approximately 5-25%) (Turkdogan 1996) are refined to the desired composition using pure oxygen. During the refining process pure oxygen reacts with carbon, manganese, silicon and other impurities in the liquid pig iron and forms oxides, which is called slag. The exothermic reactions raise the liquid steel temperature to approximately 1650^o C. A schematic of the BOF operating cycle is shown in Figure 1.3. The BOF operating cycle is made up of charging scrap and hot metal (Figure 1.3a and 1.3b), refining (Figure 1.3c), chemical testing (1.3d), tapping (Figure 1.3e) and pouring slag (Figure 1.3f). A typical steel tap-to-tap cycle in BOF steelmaking is 45 minutes.

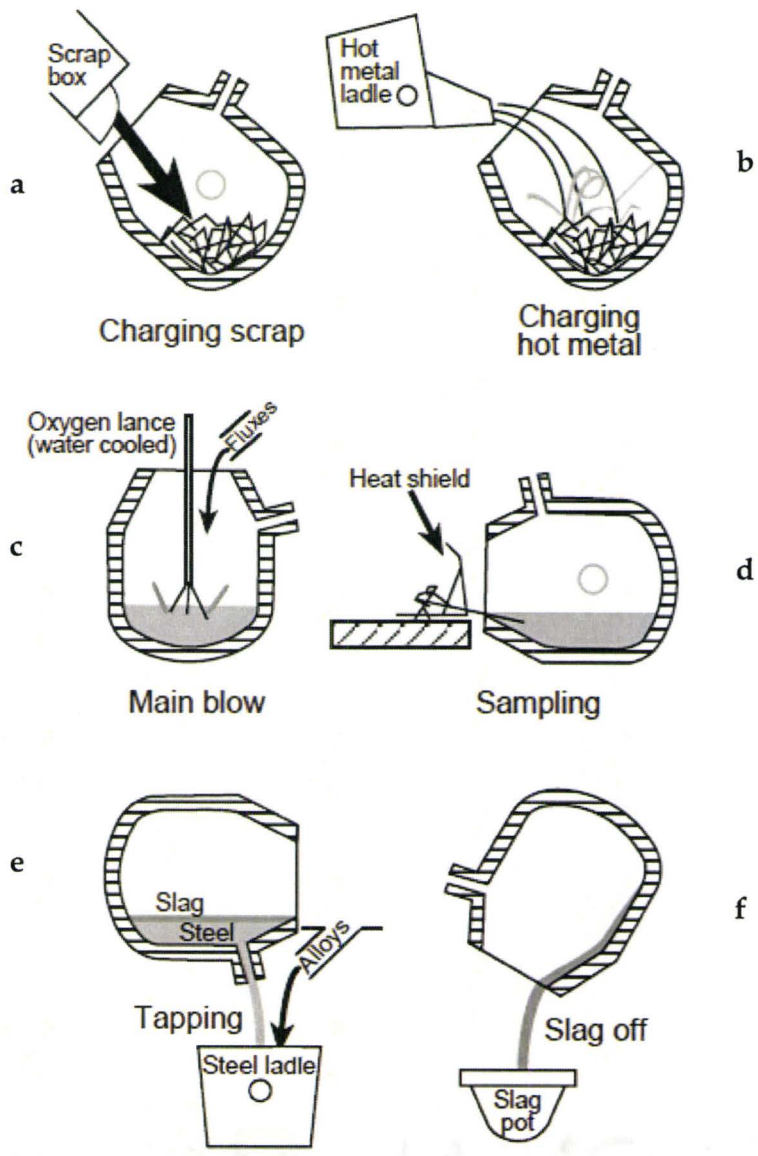


Figure 1.3: Operational steps of BOF Steelmaking (Fruehan, 1998)

1.3 Electric Arc Furnace Steelmaking (EAF Steelmaking)

EAF steelmaking production is smaller in the world steel production compared to BOF steelmaking, Figure 1.1. However, due to the low capital cost, environmental concerns and operating cost the use of EAF steelmaking has increased rapidly over the BOF steelmaking in developed countries. Over the past decade EAF steelmaking has increased from 45% to 58% of total crude steel production in North America (IISI, 2007b). Unlike the BOF steelmaking route, the EAF does not generally use hot metal. In EAF steelmaking scrap is melted using electrical and chemical energy and then refined to produce steel. The classification and design and process of EAF steelmaking are described below.

Electric Arc Furnaces can be classified into two types. One is Alternating Current (AC) Electric Arc Furnace and the other is Direct Current (DC) Electric Arc Furnace. In AC Electric Arc Furnace generally three electrodes are used to heat the scrap by the alternating current. A schematic of an AC Electric Arc Furnace are shown in Figure 1.4.

The DC Electric Arc Furnace has a single graphite electrode in the furnace center, which acts as a cathode while the bottom of the furnace acts as an anode.

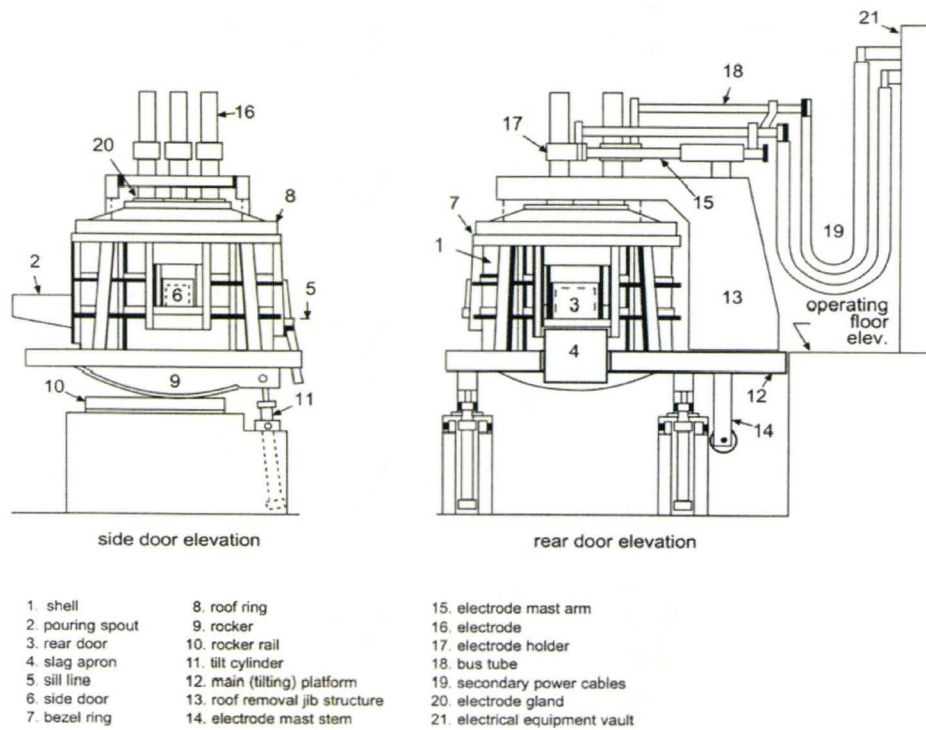


Figure 1.4: Several components of Electric Arc Furnace (Fruehan, 1998)

The Electric Arc Furnace (EAF) consists of spherical bottom, cylindrical shell and a dome shaped water-cooled roof as shown in Figure 1.4. It has several components. These components fall into several functional groups of a) furnace structure, b) components which allow for the movement of the furnace, c) components that support and supply the power of the furnace, and d) some auxiliary process equipment. Generally, the size of Electric Arc Furnace varies in shell diameter from 2.4 m to 11.6 m. The furnace shell (Figure 1.4) is of reinforced steel plate construction, cylindrical in shape with axis vertically oriented, and closed on the bottom

with a spherically-dished steel plate, which is bolted or welded to the cylindrical structure. The shell is lined with a refractory material suitable for the temperature and chemistry requirements of the process and product for which the furnace is used. The top of the shell is open, and is covered during the arcing operation with a tight fitting, removable dome-shaped refractory roof structure. The cooling of the furnace roof is done by water-cooled panels. The center of the roof is called the roof delta, which is also water-cooled. The furnace bottom consists of a spherical shaped steel shell with several layers of refractory material suitable for the temperature and chemistry (Fruehan, 1998).

The Electric Arc Furnace (EAF) operates as a batch melting process producing batches of molten steel known as 'heats'. The EAF operating cycle is made up of furnace charging, melting, refining, de-slagging, tapping and furnace turnaround. The main furnace operation stages are shown in Figure 1.5. In recent times the tap-to-tap cycle is less than 60 minutes. The first step in the cycle is charging. Before charging, steel scrap must be layered in a container known as the 'bucket' according to size and density. During charging, the scrap falls into the furnace. Most operations aim for two to three buckets of scrap charge per heat. Some operations achieve a single bucket charge. After charging, melting starts, where scrap melts via electric energy and/or chemical energy. Electrical energy is

supplied via the graphite electrodes and is usually the largest contributor of energy in melting operations. Chemical energy may be supplied via several sources including fuel-air burners, oxy-fuel burners, oxygen lances and post combustion. Fuel-air burners burn natural gas and air. Oxy-fuel burners burn natural gas and oxygen. Heat is transferred to the scrap by flame radiation and convection by the hot products of combustion. Once enough scrap is melted to accommodate the second charge, the scrap charging process is repeated. The refining starts after the melting process. During refining oxygen is blown into the liquid steel using a lance and appropriate flux (e.g., lime) addition is done. The refining process involves the removal of impurities in steel, namely phosphorous, sulfur, carbon, and manganese. After refining, de-slagging is done. Once the desired steel composition and temperature are achieved, the tap hole is opened, then furnace is tilted, and steel pours into a ladle; this is called tapping. After tapping the furnace is ready to take a new charge. The time between the completion of tapping and the first scrap charge in the furnace for the next heat is known as furnace turnaround time, which includes repairs and maintenance. A typical 60 minutes tap-to-tap cycle can be presented as: First Charge (3 minutes), First Meltdown (20 minutes), Second Charge (3 minutes), Second meltdown (14 minutes), Refining (10 minutes), Tapping (3 minutes) and Turnaround (7 minutes) (Fruehan, 1998).

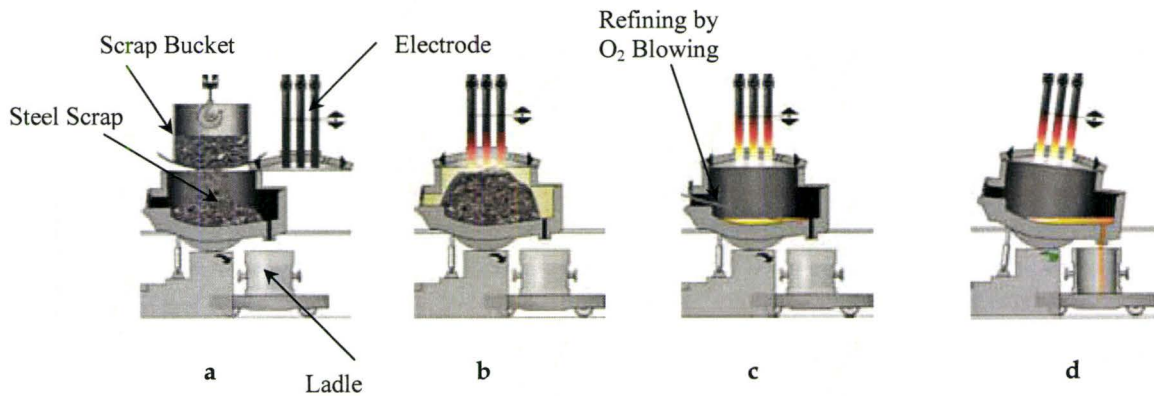


Figure 1.5: EAF Operation sequence, a) Scrap Charging, b) Heating, c) Refining and d) Tapping (steeluniversity.org)

1.4 Electric Arc Furnace Materials and Energy Balance

In general the materials that go into the Electric Arc Furnace (EAF) are steel scrap, pig iron, fluxes, coke, deoxidation materials, natural gas and oxygen. The materials that come out from the EAF are liquid steel, slag, dust and off gas. The material balance depends upon the specific practice and materials quality. Recently, Camdali and Tunc, 2002, presented a typical material balance which is reproduced in Table 1.2

Table 1.2 Typical Materials Balance for EAF (Camdali and Tunc, 2002)

	Materials	Percent (wt%)
INPUTS	Steel Scrap	77.64
	Pig Iron	11.31
	Fluxes	3.20
	Coke	1.37
	Deoxidation Materials	0.52
	Electrodes	0.23
	Natural Gas	0.24
	Oxygen	5.47
	TOTAL	100%
	OUTPUTS	Liquid Steel
Slag		6.34
Dust		1.20
Off Gas		6.79
Steel in the slag		0.46
TOTAL		100%

The energy costs are ~30% of the total costs for Electric Arc Furnace (EAF) steelmaking (Mapelli and Baragiola, 2006). Theoretically, a minimum of 300 kWh/ton is needed to melt the scrap. Additional energy is required to provide superheat of the liquid steel. So, the total theoretical energy required to produce steel is in the range of 350-370 kWh/ton. The energy efficiency, i.e., the ratio of energy utilized to heat the scrap, melt the scrap and superheat the molten metal, to actual total energy supplied, of modern Electric Arc Furnace (EAF) lies in between 55-65% and therefore the total energy required to produce steel in EAF is usually 560-680 kWh/ton (Fruehan, 1998). Baukal et al., 1990, summarized the energy distribution during the EAF operation as approximately 75% of the total energy utilized is used to heat the scrap; about 20% of the energy is used

to melt the scrap and about 5% of the energy is used to superheat the molten metal. This energy is supplied to the EAF through electrical energy, oxy-fuel burners and chemical reactions. Electrical energy is supplied through graphite electrodes. Oxy-fuel burners are introduced into the EAF through wall. The chemical energy, which is added to the EAF via exothermic reactions as;



The energy distribution of the EAF is highly dependent upon the local raw material costs and electrical energy costs. A typical energy balance is shown in Table 1.3 for a modern Electric Arc Furnace (EAF).

Table 1.3 Typical Energy Balance for Modern Electric Arc Furnace (Fruhean, 1998)

	Energy Source	Percent of energy
INPUTS	Electrical Energy	50 - 60 %
	Burners	5 - 10 %
	Chemical Reactions	30 - 40 %
	TOTAL	100%
OUTPUTS	Steel	55 - 60 %
	Slag	8 - 10 %
	Cooling Water	8 - 10 %
	Off Gas	17 - 28 %
	Miscellaneous	1 - 3 %
	TOTAL	100%

1.5 Preheating - A Literature Review

Recently there has been a greater interest in processes that reduce the electrical energy consumption during Electric Arc Furnace steelmaking. One of the processes which reduce the electrical energy consumption is scrap preheating. Scrap preheating can lead to reduce electrical energy consumption because most of the energy consumed in Electric Arc Furnace steelmaking is used to heat the solid scrap (Baukal et al., 1990). The benefits of scrap preheating are summarized here.

- Total electrical energy consumption decreases
- Productivity increases by reducing tap-to-tap time
- Low cost of electrode per ton of steel produced for reduced tap-to-tap time
- Eliminates the possibilities of charging wet scrap, which eliminates the possibilities of furnace explosions

A literature review of different processes, which preheat the scrap before charging to Electric Arc Furnace, is presented here.

1.5.1 Scrap Preheater

The concept behind the scrap preheating is before charging to EAF the scrap is preheated in a bucket using hot gas. The source of hot gases is either from burners or Electric Arc Furnace off gases. In this Section scrap preheating using burners is described. A schematic of scrap preheater for

an Electric Arc Furnace is shown in Figure 1.6; where on top of the charging bucket the burners are positioned to heat the scrap. It was mentioned earlier that about 75% of the energy is used to heat the scrap in Electric Arc Furnace, so energy can be saved by using a hot scrap charge. Using scrap preheating it is estimated that a total of 63-72 kWh/ton of electrical energy can be saved with a scrap preheating temperature around 425-540°C (Fruhean, 1998). Rudzki et al. 1973, observed at Stelton that using scrap preheating of around 425°C the EAF productivity was increased by 11.7%, electric power consumption was reduced by 11.9% and electrode consumption was decreased by 9.05%. Also, it is reported by Franklin (Franklin, 1991) that after using scrap preheater Harrison Steel Company reduced electrical consumption and tap-to-tap time by 9% and 7%, respectively

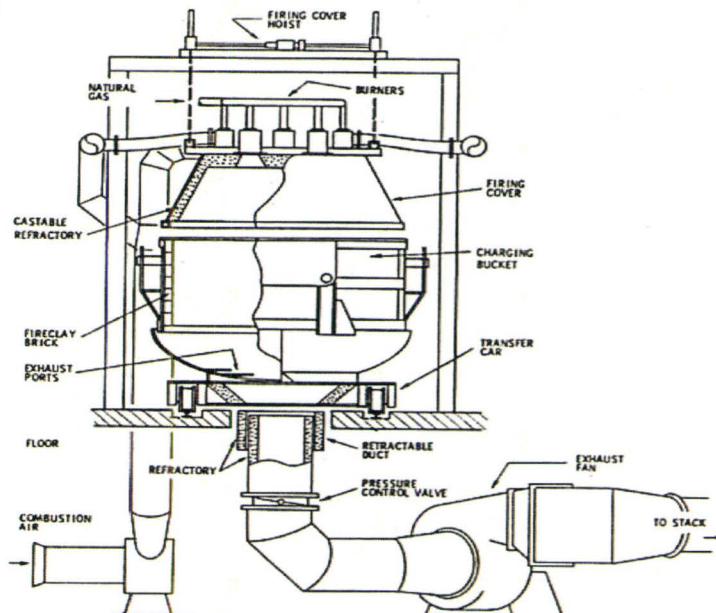


Figure 1.6: Schematic of Scrap Preheater for an EAF (Rudzki et al., 1973)

1.5.2 The Fuchs Shaft Furnace

Scrap preheating with Electric Arc Furnace off gases have the off gases passing through preheat chambers, which contain scrap. Scrap can be preheated using Electric Arc Furnace off gases in Fuchs Shaft Furnace. The Fuchs Shaft Furnace consists of vertical shaft that channels the off gases to preheat the scrap before falling into the Electric Arc Furnace. The schematic of the Co-Steel Sheerness (Clayton, 1993) shaft furnace is shown in Figure 1.7. The scrap stays in a column at one end of the furnace and can be fed continuously into the furnace as the scrap at the bottom of the column is melted away. In this system the scrap can be charged continuously or through a system called "fingers". The Fuchs system makes it possible to preheat all scrap. Using Fuchs Shaft furnace Co-Steel Sheerness claimed that 72 kWh/ton (Clayton, 1993) of energy could be recovered from the off gas. Also they increased burner power significantly in the furnace and observed that the burner efficiency is higher than that of conventional EAF since the flame contacted cold scrap for longer distance and longer time. None of these furnaces are operating because of maintenance issues.

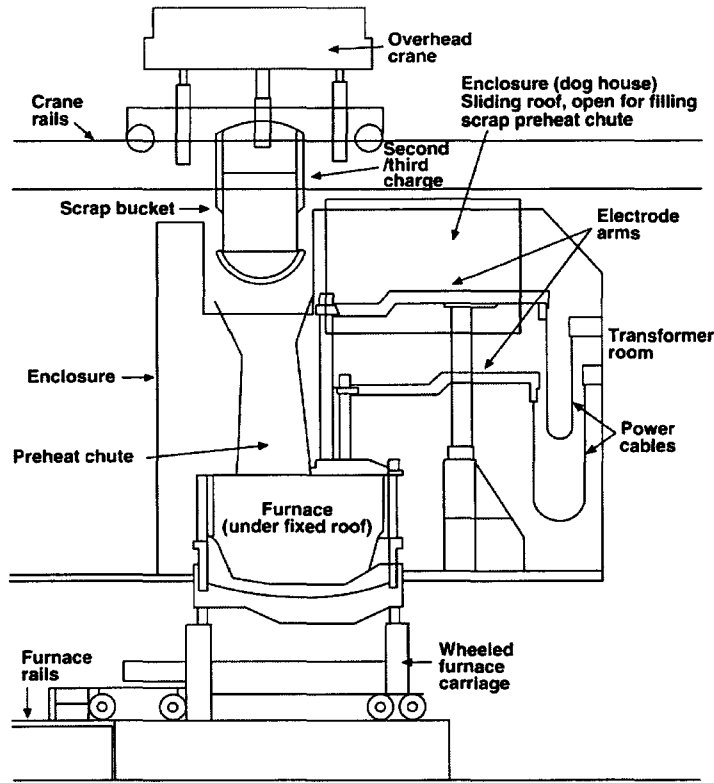


Figure 1.7: Schematic of Fuchs Shaft Furnace (Clayton, 1993)

1.5.3 Nippon Steel Shaft Type Preheating System UL-BA (Ultimate Batch System)

Nippon Steel Corporation has proposed the new conceptual shaft type preheating system, which is known as Ultimate Batch System (UL-BA), (Nakano et al., 1999). In 1997 Nippon Steel Corporation constructed a $\frac{1}{4}$ scale pilot plant to study the characteristic of scrap preheating. Figure 1.8 is a schematic of EAF equipment with UL-BA. In UL-BA system off gases from Electric Arc Furnace can be fed into the shaft via a connecting duct. A gas header is installed underneath the shaft, which fed off gases

uniformly into the shaft and preheats the scrap uniformly. Nakano et al., 1999, performed a heat balance and calculated the preheating efficiency for different scrap e.g., #2 heavy, mixture of turnings and heavy scrap (#2 heavy 85% and turnings 15%), mixture of heavy and shredded scrap (#2heavy 10% and shredded scrap 90%). The outline of the pilot plant by which they performed heat balance and preheating efficiency calculation is shown in Figure 1.9, where off gas is fed from the top of the shaft.

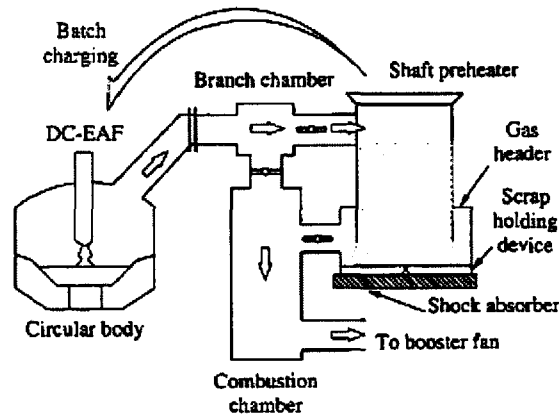


Figure 1.8: Schematic of Nippon Steel Corporation UL-BA (Nakano et al., 1999)

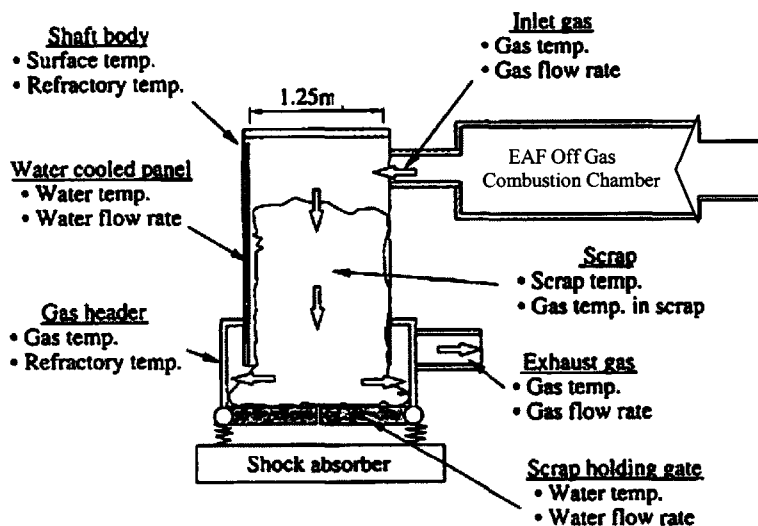


Figure 1.9: Outline of the pilot plant, UL-BA (Nakano et al., 1999)

In this study they monitored all of the parameters of the shaft body, water cooled panel, gas holder, scrap holding gate, scrap, exhaust gas and inlet gas. The total heat loss is the sum of heat losses to the refractory of shaft body, water cooled panel, air and exhaust gas. The heat storage in the scrap is the difference between total heat in through inlet gas and total heat loss. The mathematical representation of heat storage to the scrap is presented here.

$$\text{Heat storage to the scrap: } \frac{dQ_{sc}}{dt} = \dot{Q}_{gas-in} - \dot{Q}_{gas-out} - \dot{Q}_{losses} \quad \dots\dots (1.4)$$

In equation 1.4;

$$\text{Sensible heat of inlet gas: } \dot{Q}_{gas-in} = \frac{dQ_{gas-in}}{dt} = C_{P(gas)} V_{gas-in} T_{gas-in} \quad \dots\dots(1.5)$$

Sensible heat of exhaust gas:

$$\dot{Q}_{gas-out} = \frac{dQ_{gas-out}}{dt} = C_{P(gas)} V_{gas-out} T_{gas-out} \quad \dots\dots(1.6)$$

$$\text{Heat losses: } \dot{Q}_{losses} = \dot{Q}_W + \dot{Q}_R + \dot{Q}_r \quad \dots\dots(1.7)$$

$$\text{Heat loss to cooling water: } \dot{Q}_W = \frac{dQ_w}{dt} = C_{P(w)} V_w \Delta T_w \quad \dots\dots(1.8)$$

$$\text{Heat storage to the refractory: } \dot{Q}_R = \frac{dQ_R}{dt} = C_{P(R)} V_R \Delta T_R \quad \dots\dots (1.9)$$

Diffused heat into the air:

$$\dot{Q}_r = \frac{dQ_r}{dt} = \alpha_s S (T_{sur} - T_o) + \sigma ES \left[\left(\frac{T_{sur} + 273}{100} \right)^4 - \left(\frac{T_o + 273}{100} \right)^4 \right] \quad \dots\dots (1.10)$$

In equation 1.10, T_{sur} and T_0 are the surrounding temperature and wall temperature, respectively. So the diffusive heat is from the walls into the air.

Scrap preheating efficiency is:
$$\eta_{sc} = \frac{Q_{sc}}{Q_{gas-in}} 100 \quad \dots\dots\dots(1.11)$$

Nakano et al. 1999, measured the scrap temperature in different layers with different heating time. The scrap temperature transition with heating time of their calculation using #2 heavy scrap is shown in Figure 1.10. After 20 minutes of preheating with gas temperature of 1200° C and gas flow rate 48Nm³/min they found that the temperature of the top layer of scrap (h_{sc} =2.1 m) is 800° C and the average temperature of the scrap is 600° C. According to their heat balance the largest portion of heat goes to the scrap (~44%), followed by the heat loss to the water cooled panel (~37%) and the sensible heat of the exhaust gas (~18%).

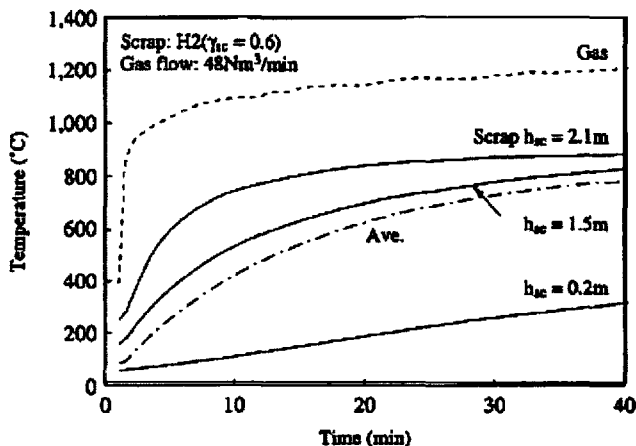


Figure 1.10: Scrap temperature with heating time (#2 heavy scrap) (Nakano et al., 1999)

Based on the experimental results, a preheating model was developed by Nakano et al, 1999. They assumed scrap temperature and gas temperature in each layer are constant and scrap is homogeneous. They used the following equation to calculate the scrap temperature.

$$\frac{dQ_{sc}}{dt} = A_S h_s V_S (T_{gas} - T_{SC}) \quad \dots\dots\dots (1.12)$$

In the above equation A_S , h_s , V_S , T_{gas} and T_{SC} are the heat transfer area per unit volume, heat transfer coefficient between scrap and gas, volume of the scrap, gas temperature and scrap temperature. Due to the complex geometry of the scrap they treated $A_S h_s$ together and which tuned to the preheating experimental results.

Nakano et al's study gives some promising results for scrap heating. The limitation of their model is that they assumed a constant temperature in layers, which is not true for all the cases. It is evident that the local temperature varies significantly according to the flow conditions. Also, in their heat transfer calculation using the experiments they first predicted a constant heat transfer coefficient between hot gas and scrap and later using that they performed the scrap temperature calculation. The local heat transfer coefficient is dependent upon the gas flow rate and temperature of the gas and which varies with location hence their assumption is debatable.

1.5.4 Twin Shell Electric Arc Furnace

One of the new technologies for Electric Arc Furnace, which is gaining popularity, is the twin shell furnace. It is similar to the scrap preheating but only difference is that scrap preheating takes place in a furnace rather than a scrap bucket. In the twin shell furnace, as shown in Figure 1.11, the operation consists of two furnace shells and one set of electrodes, which are used alternately on one shell and then other. In this system there is no melting process going on in one furnace shell which is charged with scrap and the scrap is preheated by the off gas from the melting furnace. Additional burners can be used during the scrap preheating. The more the scrap is preheated, the greater electric energy savings. In this process there is one charge per heat, which also reduces heat losses. This system increases the productivity by reducing tap-to-tap time and reducing heat losses per ton produced. It is important to mention here that in some twin shell Electric Arc Furnaces scrap is not heated by off gases from the melting furnace, e.g., ArcelorMittal DOFASCO twin shell Electric Arc Furnace. In this case scrap is heated in the shell, where melting is by burners.

Nippon Steel (Fruehan, 1998) mixed combustion gases from the burners in a combustion chamber with the off gas from the first shell to produce a constant temperature of 900^o C for preheating in the second shell. They

also used remaining heat in the off gas from both the furnaces to heat the scrap in the scrap bucket. They found that the net electrical power input requirement was 260 kWh/ton, which was 29% lower than that of a conventional furnace.

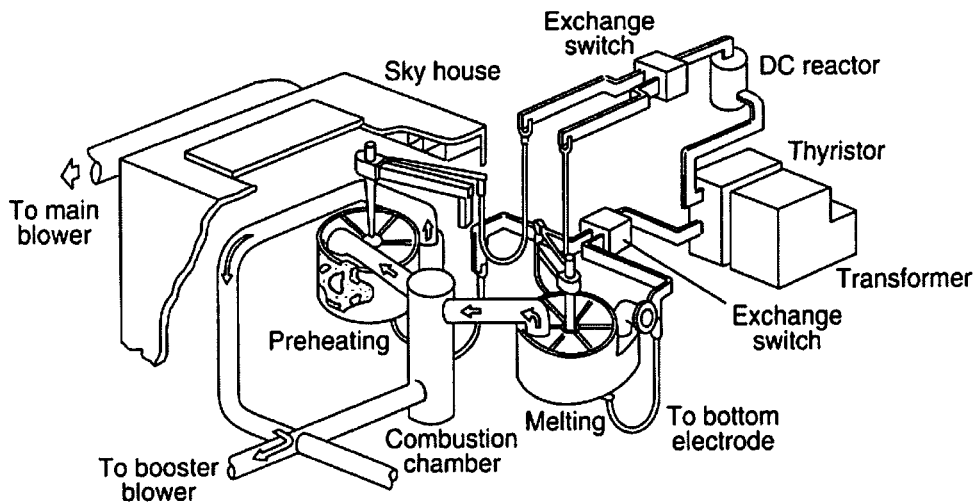


Figure 1.11: Schematic of Twin Shell EAF at Nippon Steel (Fruehan, 1998)

1.5.5 CONSTEEL

The basic concept of the CONSTEEL process is the continuous feeding system for scrap and slag foaming materials, a preheater and a melting and refining EAF, which is shown in Figure 1.12 (Vallomy, 1994). In this process the scrap is directly charged from the scrap yard to the charge conveyor. The charge is then continuously conveyed to the EAF, while being preheated in the preheater conveyor by the chemical and sensible

heat of the off gases that leave the furnace. The post combustion of the carbon monoxide produced by the oxygen injection in the EAF is carried out in the preheater and is an extra advantage of this technology. In CONSTEEL the role of post combustion and preheating of scrap with post combustion is very important. It is proven that by using this technology very high productivity and high steel quality can be achieved. In addition hot metal may be added as a part of the charge up to 20-40% (Vallomy, 1999).

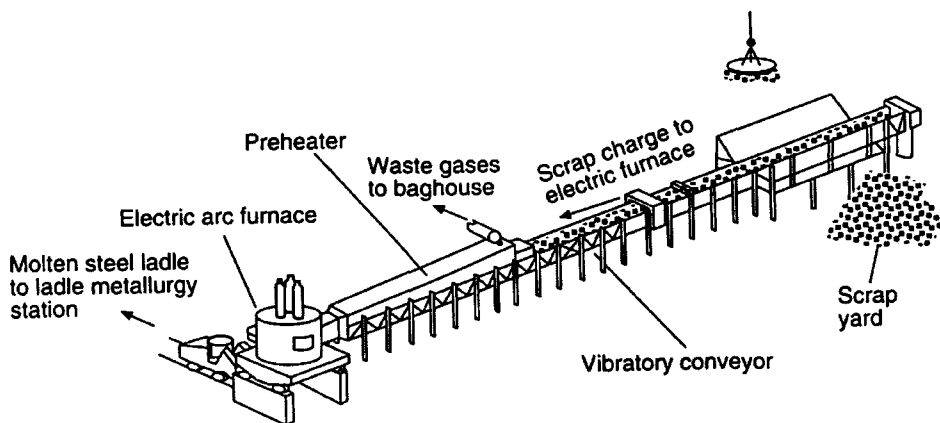


Figure 1.12: Components of CONSTEEL process (Fruehan, 1998)

1.6 Problems During Scrap Preheating

During scrap heating a problem arises due to the organic compounds associated with the scrap. Due to insufficient oxygen supply during scrap heating these organic hydrocarbons report to the off gas system. The best procedure to restrict volatile organic compounds emission during scrap

preheating is to operate the burners with excess oxygen. The other concern during scrap heating are dioxins, which are hydrocarbons that are usually formed in combustion process. The components of the off gas stream in the EAF are ideal for the formation of dioxins. Dioxins are toxic and it forms at a temperature of 500°C during cooling of the off gases. The factors that can reduce the dioxins emissions are; a) post combustion of organics in the furnace and b) absorbent injection in the off gas. Also dioxins emissions can be reduced by rapid quenching of the off gas from 800°C to 300°C (Fruehan, 1998).

The aforementioned development for EAF were essentially aimed to heat the scrap before charging to EAF using off gas or additional burners, which reduce the electrical energy consumption of EAF and increase productivity by reducing tap to tap time. Besides these, the most important techniques that can be used to reduce the electrical energy consumption of EAF are stirring the bath (Baukal, 1990) post combustion (Li and Fruehan, 2003, Tang et al, 2003 and Mathur and Daughtridge, 1994) and use of burners inside EAF (Baukal, 1990, Jones, 1994, Shifrin, 2001, Thomson et al, 2001, Teoh, 1989, Adolph et al, 1989 and Wells and Vonesh, 1986).

Understanding of the phenomena of heat transfer between hot gases either combusted or off gases and scrap is very important for the processes of scrap preheating, shaft furnace, twin shell furnace and CONSTEEL and use of burners inside the EAF. Oxy-fuel burners, which are now standard equipment in EAF, were first used to melt the scrap at the slag door where arc heating is inefficient, but it was quickly realized that productivity could be increased by more burner power. Generally, there are at least three burners positioned in the cold spots between electrodes (Jones, 1994). Typical productivity increases using burners inside the EAF are in the range of 5 to 20% as reported by different investigators (Teoh, 1989, Adolph et al, 1989 and Wells and Vonesh, 1986). Shifrin et al (Shifrin, 2001) found that 90 to 115 kWh/tonne could be saved by using oxygen and natural gas in the burners.

Recently, Guo and Irons (Guo and Irons, 2005, 2006) studied the fluid flow and scrap melting phenomena using combined effects of burner and arc heating in the Electric Arc Furnace. Their main assumption was the uniformity of the scrap properties i.e., average size of the scrap, scrap thickness, porosity and specific area. The above mentioned study reported that the heating efficiency of the burner decreases with time of heating and the burner power needs to be reduced once the heating efficiency decrease sufficiently. It was also reported by Guo and Irons (Guo and

Irons, 2005, 2006) that the burner heating efficiency was strongly affected by the volumetric heat transfer coefficient. However they were only able to estimate values for the heat transfer coefficients.

1.7 Objectives and Overall Structure - of the Present Study

1.7.1 Objectives

Despite the impressive performance of the burners, there is little information on the efficiency of the transfer of the combustion heat to the steel scrap in the furnace. The objectives of the present research are to understand the effects of scrap size, scrap density, burner power and different scrap bed configurations on steel scrap heating by burner combustion gases. The ultimate aim of the present study is to improve industrial steel scrap heating practice by burners. To this end an experimental and numerical study was carried out, which included heat transfer and fluid flow behavior in non-uniform porous media at high temperature.

1.7.2 Overall Structure of the Present Research

The overall structure of the present research is shown in Figure 1.13. The study is divided into two parts: one is experimental and the other is numerical modeling, which will be used to validate the numerical model.

The numerical modeling involves development of heat transfer and fluid flow model for 3-dimensional Cartesian co-ordinate system in porous media. The experimental work is divided into three parts, one is measurement of porosity and packing density distribution for different sizes of scrap, the second is measurement of the heat source term and the final one is experiments for temperature distribution inside a small-scale furnace heated with a burner.

The numerical model will be validated and tuned with the measured temperatures of the physical model.

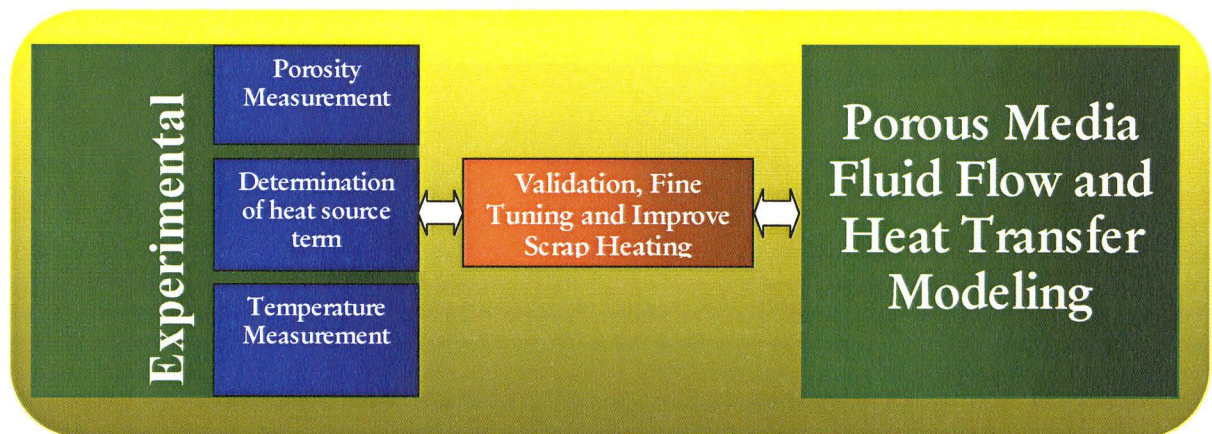


Figure 1.13: Overall Structure of the Research

Chapter 2

Experimental

2.1 Introduction

The main objectives of this experimental study were to measure heating of steel scrap using a burner and to validate the numerical model. Details of experimental studies during the present research are presented in this chapter.

2.2 Furnace Design

The present study is focused on the region of the Electric Arc Furnace around the burners, as shown schematically in Figure 2.1. The aim of the present study is to measure the efficiency of heat transfer between the flame and scrap in the initial stages, not to melt the scrap. Burner-to-burner interactions were not considered in this study. In this scaled down experimental study neither proper furnace to scrap size ratio was used nor proper power input according to the real Electric Arc Furnace was used. Also, electric power input was not considered in this study.

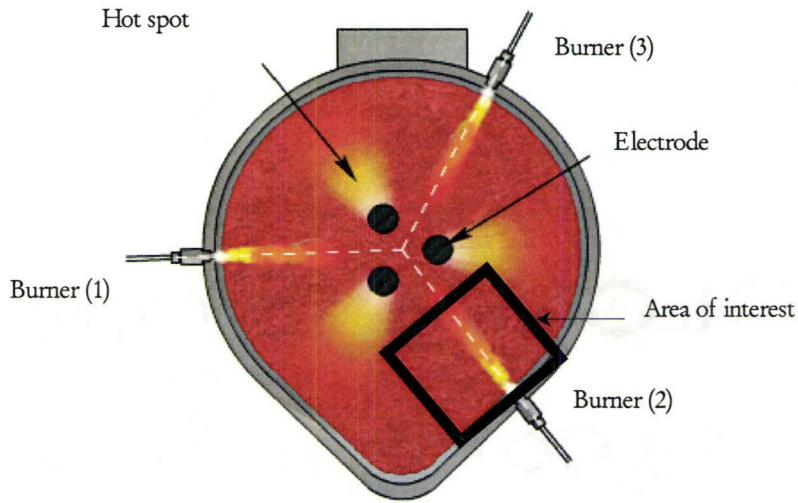


Figure 2.1: A schematic of present Area of Research Interest

The scrap-heating furnace was designed and built in the lab. A photograph of the scrap heating furnace is shown in Figure 2.2, along with its dimensions in Figure 2.3. The furnace shell is made of steel with refractory lining on bottom, and the front wall with the burner. There are two layers of refractory on the front wall; the first layer is made of 65 mm thick insulating brick and the hot face layer is made of 113 mm thick alumina brick. There is a removable lid with a chimney, which is not shown in Figure 2.2, but is shown in Figure 2.3. An in-house designed, premixed oxy-propane burner, located on the front centerline of the furnace as shown in Figure 2.2, is used. Above the burner, there is a hole for observation of the flame and scrap melting in front of the burner. To capture the temperature distribution inside the furnace, thermocouples

are introduced from one side of the furnace at locations shown in Figure 2.2. Thermocouples are connected with the data acquisition system, which recorded temperatures at 30 seconds intervals. Details of thermocouple types and the data acquisition system are explained in Section 2.3 i.e., ancillary equipment.

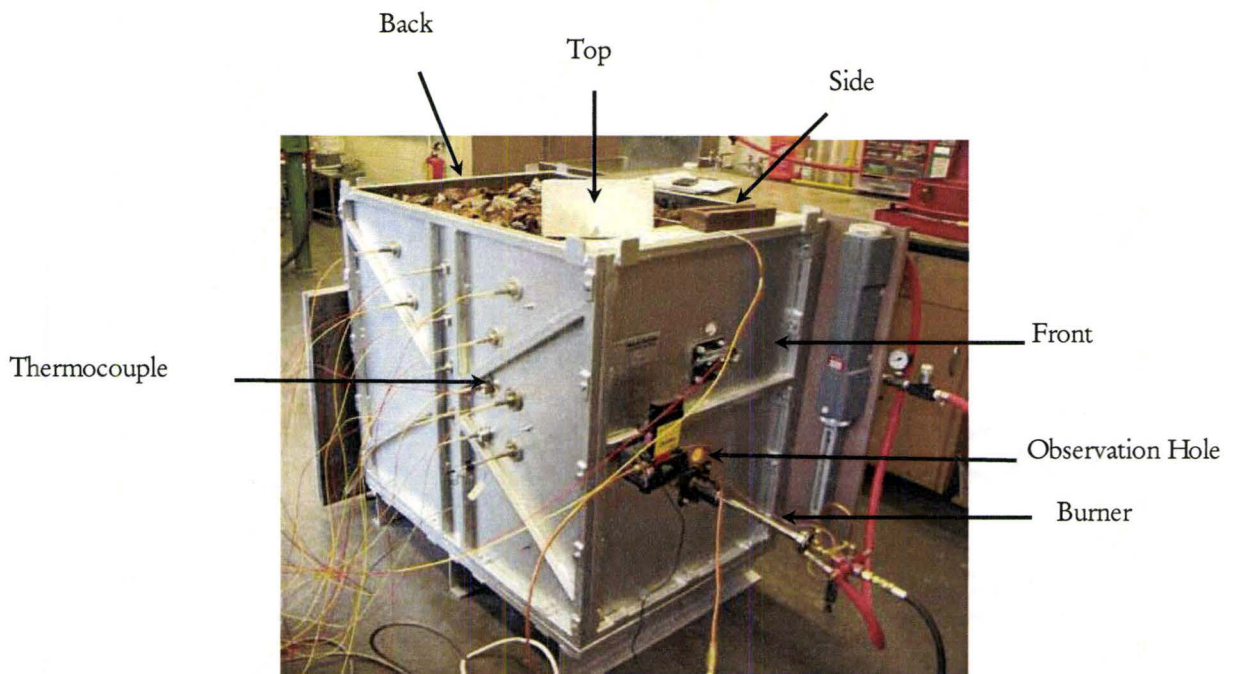


Figure 2.2: A Picture of Scrap Heating Furnace

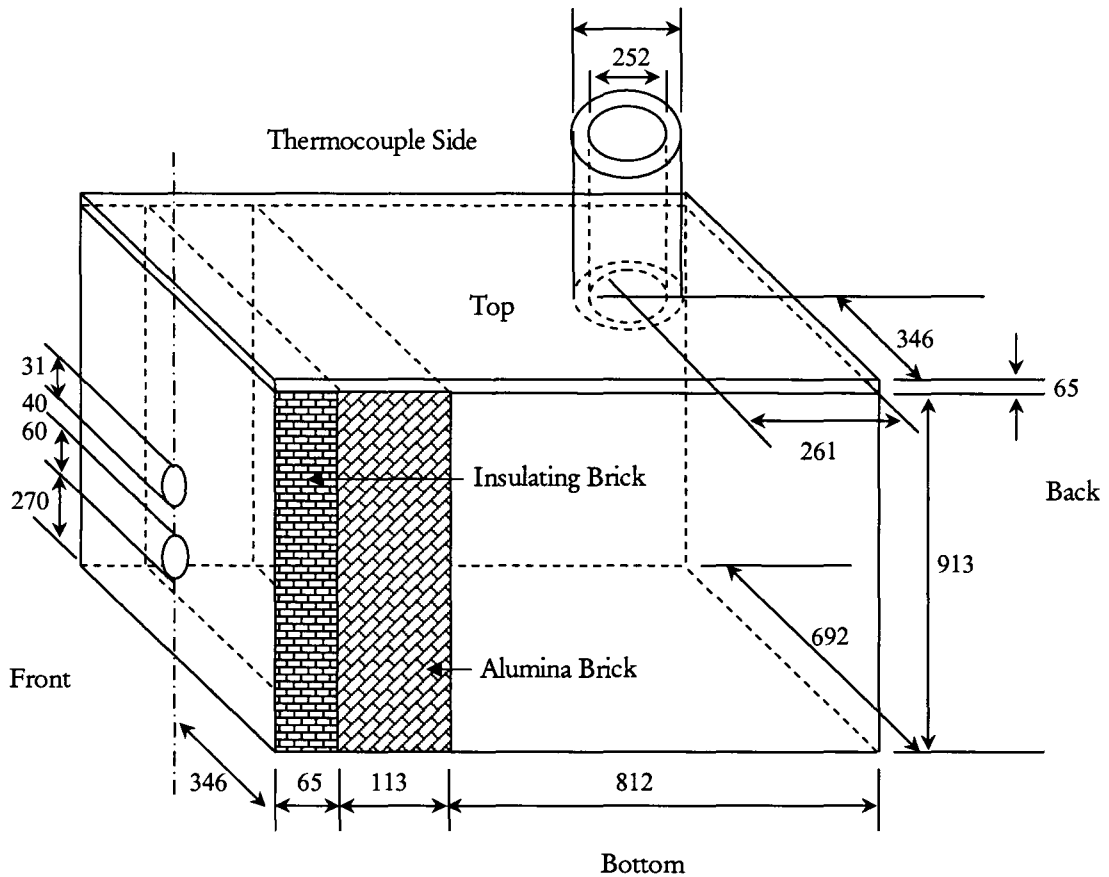


Figure 2.3: A Schematic View of the Scrap Heating Furnace (mm) (not to scale).

2.3 Ancillary Equipment

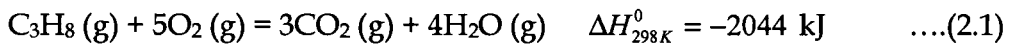
In this Section details about the burner, thermocouples, data acquisition system and gas analyzer are discussed.

2.3.1 Burner

An in-house premixed oxy-propane burner is used as a heat source during scrap heating experiments. A schematic of the burner is shown in Figure

2.4. Figure 2.5 shows a close-up photograph of the burner. There are two gas supply lines in the burner, one is for propane and the other is for oxygen. The burner is made with 4.00 mm diameter hollow steel rod and at the end with alumina refractory material to resist the high temperature of the flame.

When a hydrocarbon such as propane burns, the final products are carbon dioxide and water vapor, unless there is a shortage of oxygen, in which case the products may contain carbon monoxide and unburned hydrocarbon. The complete combustion reaction of propane and oxygen is as follows (FactSage 5.5, 2007);



In the above equation it was assumed that no hydrogen or carbon was produced in the combustion reaction of propane and oxygen. From equation 2.1 it is clear that for complete combustion of propane the ratio of volume of oxygen to volume of propane needed is 5. It is possible that, due to incomplete combustion some unburned propane and oxygen or some carbon monoxide and oxygen are present in the combustion products.

Incomplete or improper combustion may reduce the total heat released by the combustion reaction considerably. So, it is essential to determine the total heat release from gas analysis. In this research burner power is experimentally determined using off gas analysis with a known quantity of helium as a tracer gas, which is discussed in Section 2.5.3.

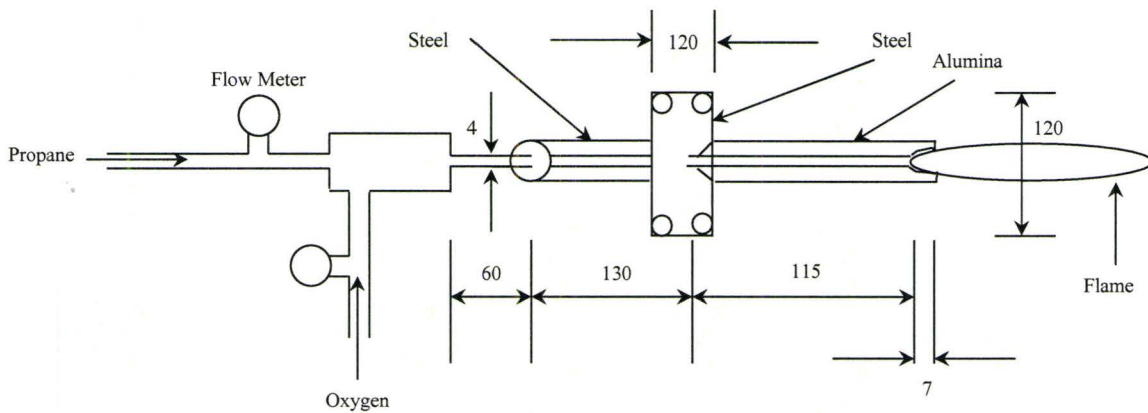


Figure 2.4: A Schematic of the Burner used for Scrap Heating (mm) (not to scale)

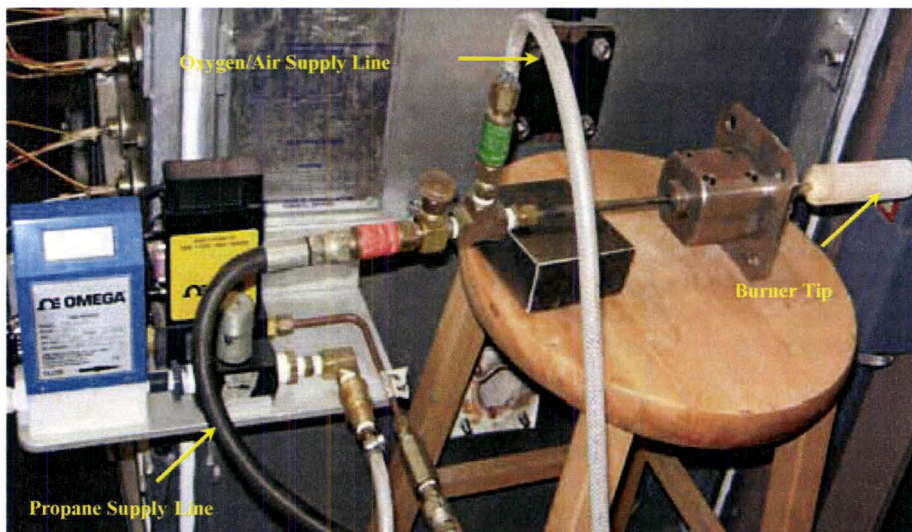


Figure 2.5: Burner used for heating

2.3.2 Thermocouples and Data Acquisition System

In the present scrap heating experiments temperatures were captured using two types of thermocouples. Near the burner pre-calibrated B type thermocouples supplied by OMEAGA, were used (Platinum - Platinum-6% Rhodium), which can measure temperatures as high as 1820° C. The rest of the thermocouples were K type i.e., Chromega - Alomega, which can measure temperatures as high as 1372° C. Temperatures were calculated according to the following relation;

$$T = c_0 + c_1E + c_2E^2 + c_3E^3 + \dots + c_nE^n \quad \dots\dots\dots(2.2)$$

In equation 2.2 , T is the temperature in degree Celsius, E is micro volts and c_0 to c_n are temperature coefficients. Values of temperature coefficients, temperature range, voltage range and error range for both B type and K type thermocouples are presented in Tables 2.1 and 2.2, respectively. K type thermocouple was calibrated using both ice water mixture and a boiling water bath. It was found that accuracy of temperature measurement were within $\pm 0.5\%$, for K type thermocouple. To capture the temperature distribution inside the furnace, thermocouples were introduced from one side of the furnace at locations shown in Figure 2.6. Thermocouples were connected to a data acquisition system Figure 2.7, which recorded temperatures at 30 seconds intervals.

Table 2.1. Temperature coefficients, temperature range, voltage range and error range for B type thermocouples

Temperature Range	250 to 700 ^o C	700 to 1820 ^o C
Voltage Range	291 to 2431 μ V	2431 to 13820 μ V
C ₀ =	9.842X10 ¹	-2.131X10 ²
C ₁ =	6.997X10 ⁻¹	2.851X10 ⁻¹
C ₂ =	-8.476X10 ⁻⁴	-5.274X10 ⁻⁵
C ₃ =	1.005X10 ⁻⁶	9.916X10 ⁻⁹
C ₄ =	-8.334X10 ⁻¹⁰	-1.296X10 ⁻¹²
C ₅ =	4.550X10 ⁻¹³	1.119X10 ⁻¹⁶
C ₆ =	-1.552X10 ⁻¹⁶	-6.062X10 ⁻²¹
C ₇ =	2.988X10 ⁻²⁰	1.866X10 ⁻²⁵
C ₈ =	-2.474X10 ⁻²⁴	-2.487X10 ⁻³⁰
Error Range	-0.02 ^o C to 0.03 ^o C	-0.02 ^o C to 0.02 ^o C

Table 2.2. Temperature coefficients, temperature range, voltage range and error range for K type thermocouples

Temperature Range	0 to 500 ^o C	500 to 1372 ^o C
Voltage Range	0 to 20644 μ V	20644 to 54886 μ V
C ₀ =	0.00	-1.318X10 ²
C ₁ =	2.508X10 ⁻²	4.830X10 ⁻²
C ₂ =	7.860X10 ⁻⁸	-1.646X10 ⁻⁶
C ₃ =	-2.503X10 ⁻¹⁰	5.464X10 ⁻¹¹
C ₄ =	8.315X10 ⁻¹⁴	-9.650X10 ⁻¹⁶
C ₅ =	-1.228X10 ⁻¹⁷	8.802X10 ⁻²¹
C ₆ =	9.804X10 ⁻²²	-3.110X10 ⁻²⁶
C ₇ =	-4.413X10 ⁻²⁶	
C ₈ =	1.057X10 ⁻³⁰	
C ₉ =	-1.052X10 ⁻³⁵	
Error Range	-0.05 ^o C to 0.04 ^o C	-0.05 ^o C to 0.06 ^o C

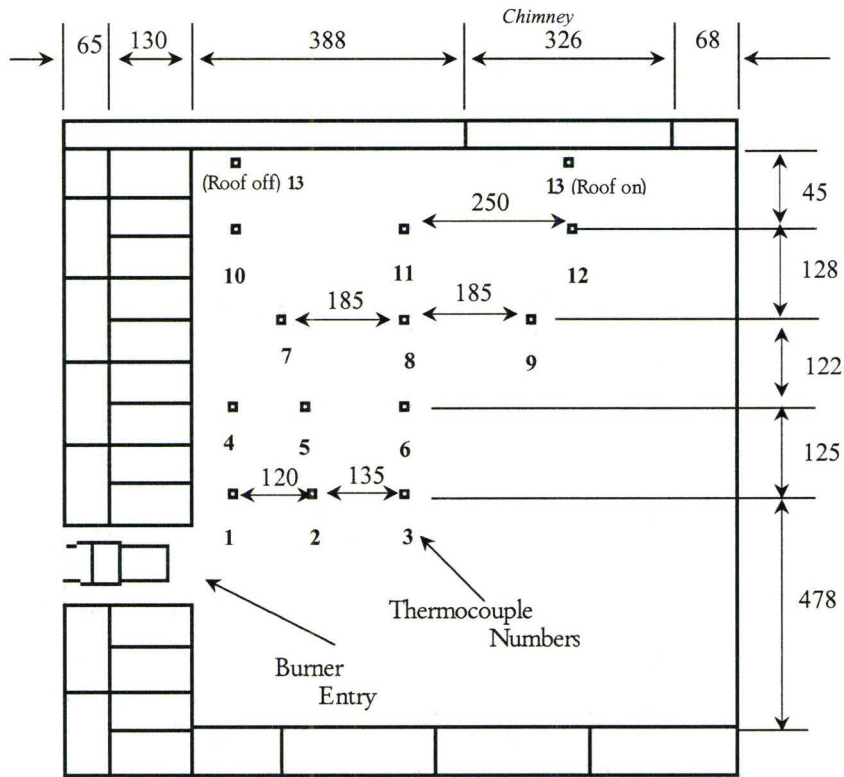


Figure 2.6: Thermocouples arrangement of the Scrap Heating Furnace (Centerline), mm (Not to scale).

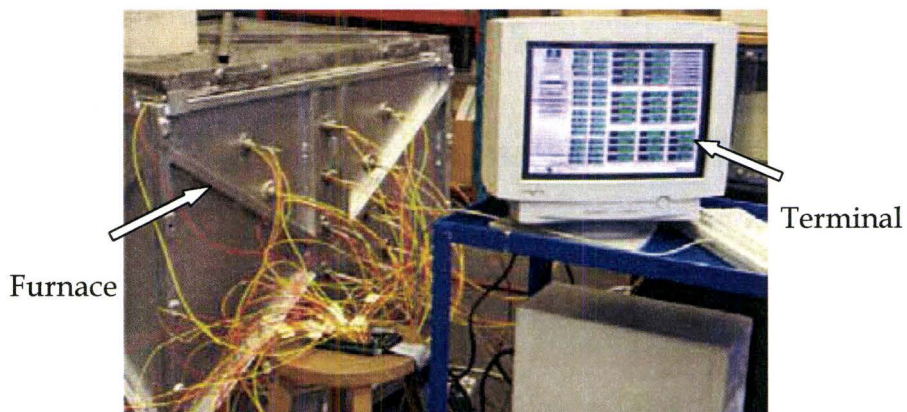


Figure 2.7: Data acquisition system (View from the thermocouple side).

2.3.3 Gas Analyzer

To measure the extent of combustion during scrap heating by burners a general purpose gas analyzer was used. A picture of the HORIBA VIA-510 gas analyzer is shown in Figure 2.8. It continuously measures the concentrations of specific gases with a non-dispersive infrared analysis method. It is known that molecules consisting of different atoms absorb infrared in their specific wavelength bands and that gases at constant pressure absorb infrared corresponding to their concentrations. Based on this principle, this analyzer utilizes the infrared absorption of the components to be measured and continuously monitors changes in the concentration of that component. The HORIBA VIA-510 general purpose gas analyzer has the capability to measure the gases of CO (0-100%), CO₂ (0-100%) and O₂ (0-50%). The equations, which were used to calculate O₂, CO and CO₂ percentage, are as follows;

$$\%O_2=0.20438+0.00488 \times E_{O_2} \quad \dots\dots\dots (2.3)$$

$$\%CO=0.13007+0.00998 \times E_{CO} \quad \dots\dots\dots (2.4)$$

$$\%CO_2=0.05501+0.00472 \times E_{CO_2} \quad \dots\dots\dots (2.5)$$

In equations 2.3 to 2.5, E is electrical potential in milli-volt (mV). Details of HORIBA gas analyzer calibration are presented in Appendix A.







Figure 2.8: HORIBA VIA-510 general purpose gas analyzer

2.4 Materials

Steel scrap from ArcelorMittal Dofasco was used for the present research. Steel scrap can be classified into three groups; obsolete scrap, industrial scrap and home scrap. Industrial scrap and home scrap are cleaner compared to obsolete scrap. In addition to above classification steel scrap can be classified according to its size, source and the way it is prepared e.g., bundles, shredded, heavy melt, busheling, turnings etc (Fruhean, 1998). Table 2.3 shows the characteristics of the shredded (small and large), busheling and heavy melt, which was used during scrap heating by burner. The details size and scrap density measurement are presented in section 2.5.1.

Table 2.3. Scrap Characteristics

← 690 mm →

			
Large Shredded Scrap	Small Shredded Scrap	Busheling	Selected Heavy Melt
Steel Density: 7200 kg/m ³ Scrap density: 9%	7500 kg/m ³ 14%	7710 kg/m ³ 7%	7300 kg/m ³ -

2.5 Measurements

In the present research, size and density of the scrap were characterized using measurements. Porosity variations from the wall to the center of the furnace were also measured in the laboratory. The extent of combustion was not known for our in-house burner. So, an experimental study was performed to determine the extent of combustion. Finally, temperature measurements were done during scrap heating by burner. In this Section details of measurements are discussed.

2.5.1 Scrap size and density measurements

Scrap characteristics were already shown in Table 2.3. Shredded scrap was sorted out into two different groups, small shredded scrap and large shredded scrap. Randomly, 50 pieces of scrap were chosen from both

small shredded scrap and large shredded scrap. The maximum length was measured for each piece of scrap. Figure 2.9 shows the distribution of maximum length for small shredded scrap. The average size for small shredded scrap was 80 mm. Similarly Figure 2.10 shows the measured maximum length for the large shredded scrap. The average size for large shredded scrap was 150 mm. Busheling and heavy melt were chosen from ArcelorMittal DOFASCO scrap yard that fit in our lab scale heating furnace, Figure 2.2.

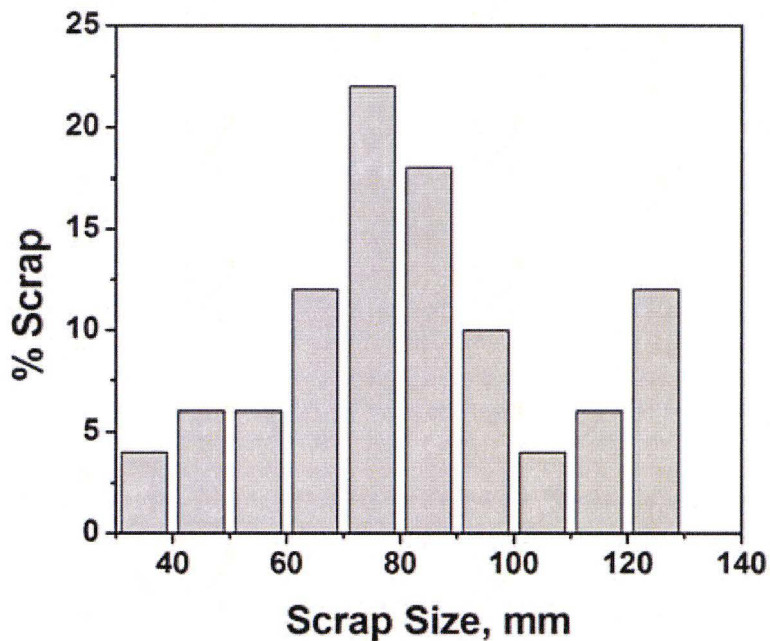


Figure 2.9: Size Distribution of Small Shredded Scrap

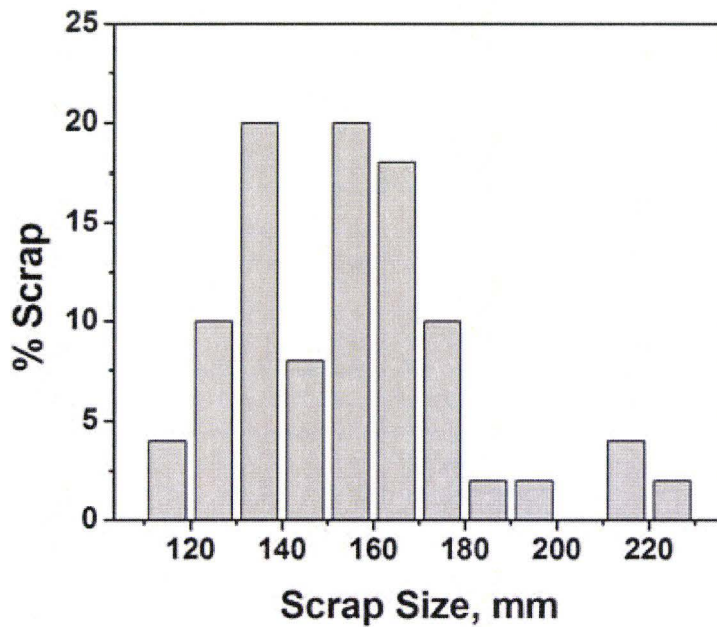


Figure 2.10: Size Distribution of Large Shredded Scrap

To measure the steel density of the scrap, initially the mass of a few pieces were taken. Then, those scrap were submerged into a plexi-glass box, which was full of water, and displaced water was collected. Using scrap mass (M_{scrap}) and collected water volume (V_{water}), steel density ($\rho_{scrap} = M_{scrap} / V_{water}$) for each group of scrap were calculated, which was already presented in Table 2.3.

2.5.2 Porosity measurements

Porosity, i.e., fractional voidage, is one of the most basic properties of an assemblage of particulate materials, which influences the fluid flow and heat transfer through a porous medium. The random packing of hard

particles has a long history of extensive study because of its importance as a model for the particulate systems. Over the years, many studies have been carried out on the packing of particles, which are summarized by Cumberland and Crawford (Cumberland and Crawford, 1987), and German (German, 1989). It is well established that the porosity of a particulate mixture is strongly affected by the particle size and distribution. The porosity distribution near the wall is also important. Earlier work on the dependency of porosity on distance from the boundary can be found in experimental results such as Roblee et al. (Roblee, Baird and Tierney, 1958) and Benenati and Brosilow (Benenati and Brosilow, 1962). Martin (Martin, 1978) and Muller (Muller, 1991) successfully modeled the porosity variation normal to the wall using randomly packed spherical particles. Although Martin and Muller modeled the porosity variation from the wall to the center of the bed using regular shaped spherical particles, it is a general trend among the researchers to use an exponential decay function, based on the experimental observation (Roblee et al. 1958 and Benenati and Brosilow, 1962). The typical exponential decay function is mathematically represented as; $\phi = \phi_{\infty} \left(1 + a e^{-bx/d_p}\right)$, where, ϕ is the local porosity, ϕ_{∞} is the porosity far away from the boundary or wall, and x is the distance from the wall. a and b are the parameters, which are adjusted according to the wall porosity, which is equal to 1 when x equals 0. d_p is the diameter of the

spherical particles. Values of a and b are 1.7 and 6 for particle diameter about 2 - 4 mm (Benenati and Brosilow, 1962). The exponential decay function for porosity variation from the wall to the center has been proven only for regular shaped particles. So, steel scrap packing inside a furnace needs to be investigated. In the present research an experimental study of steel scrap packing was carried out to determine the porosity variation from the wall to the center of the bed.

In our research a plexiglass vessel was used to measure porosity of steel scrap packing, which is shown in Figure 2.11. The plexiglass vessel was marked into different segments in X, Y and Z directions, which is shown in Figure 2.12. The vessel has two openings one is at the top and the other is at the bottom. The bottom opening has a valve.

In the beginning of the experiment steel scrap was packed randomly inside the vessel as shown in Figure 2.11. Then, known quantity of tap water was poured into the vessel and the amount of water poured into the vessel for each segment was monitored. Porosity in each segment was calculated by equation 2.6 using volume of water poured in each segment and volume of each segment.

$$\phi = \text{Porosity} = \frac{V_W}{V_S} \quad \dots\dots\dots (2.6)$$

where, V_W is volume of water poured in each segment and V_S is volume of each segment. When one direction, say Y, was filled with water, the water was then drained out through the bottom opening and the vessel was rotated to perform the same procedure for another direction, say X. The same procedure was also repeated for the third direction, i.e., Z. After each set of experiments, the steel scrap was taken out and dried. The same scrap was again randomly packed inside the vessel and the procedure was repeated to obtain five sets of measurements. The results for each experiment are designated as "Packing 1", "Packing 2", "Packing 3", "Packing 4" and "Packing 5" in the Figures 2.13 to 2.16. The same procedure was followed for shredded and busheling.

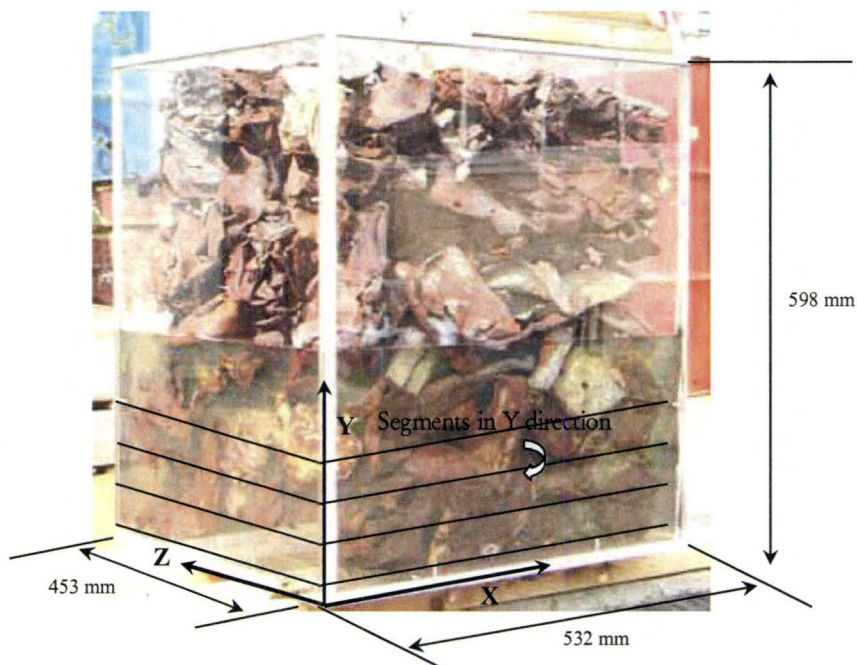


Figure 2.11: Plexiglass porosity measurement vessel

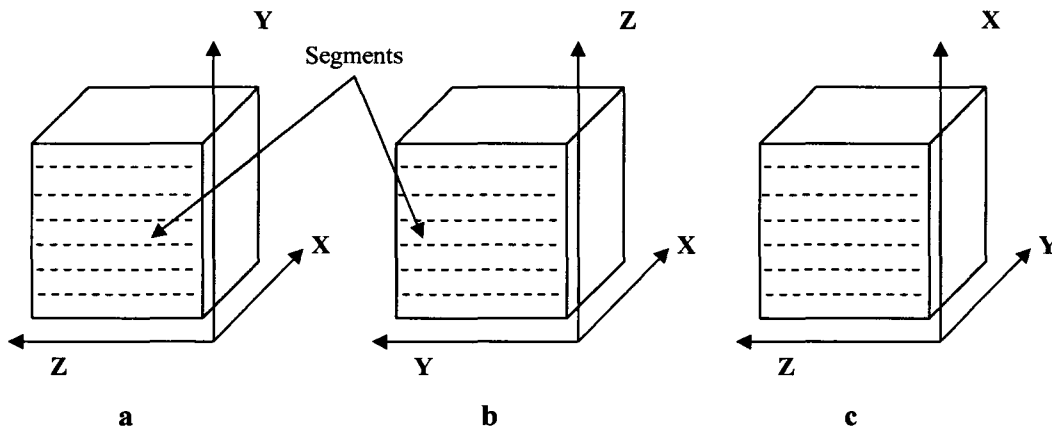


Figure 2.12: Segments in a) Y direction, b) Z direction and c) X direction

The measured porosity variations with distance from the wall to the center are shown in Figure 2.13 - 2.15, for small shredded scrap in X, Y and Z directions and different packing or tests. It is seen that the porosity varies from the wall to the center of the bed. At the wall the porosity approaches 1 and at a distance of the order of the average particle size, the porosity remains uniform, which is similar to the randomly packed spherical shaped particles. It is also seen from the same figures that porosity variation pattern is the same in all directions. Similar porosity distribution patterns were also observed with large shredded scrap, which is shown in Figure 2.16. For busheling the porosity variation is more random, as shown in Figure 2.17.

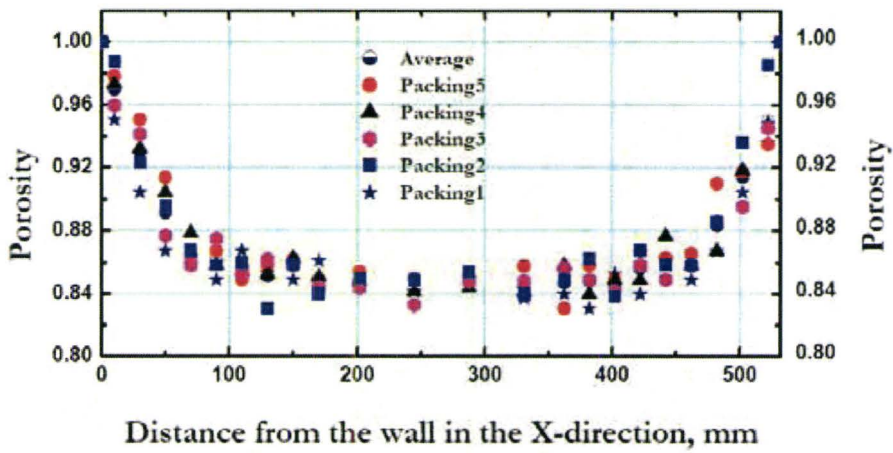


Figure 2.13 Porosity variations from the wall to the center for small shredded scrap (average scrap length 80 mm) in X-direction

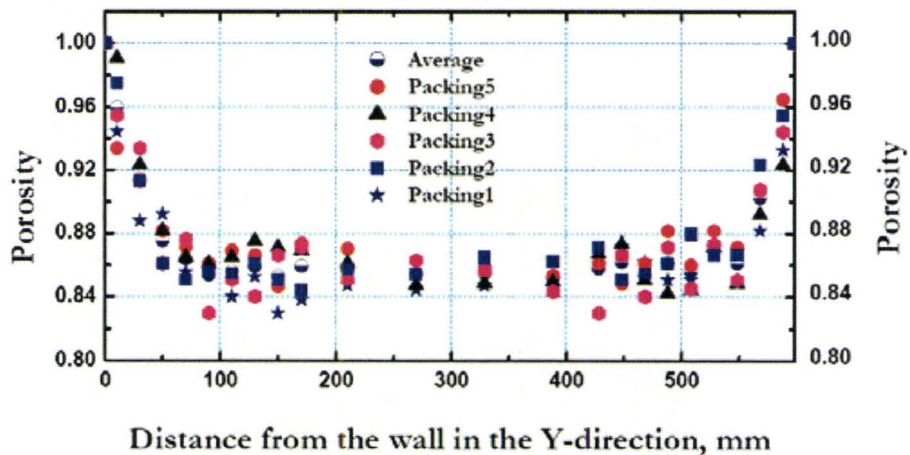


Figure 2.14: Porosity variation from the wall to the center for small shredded scrap (average scrap length 80 mm) in Y-direction

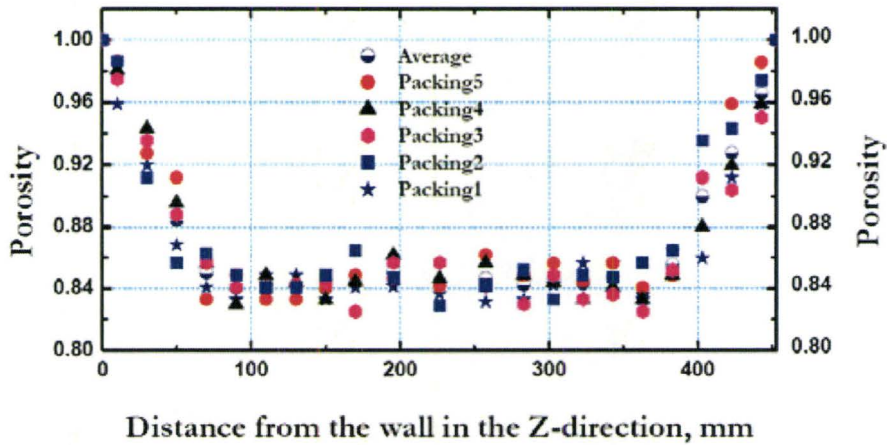


Figure 2.15: Porosity variation from the wall to the center for small shredded scrap (average scrap length 80 mm) in Z-direction

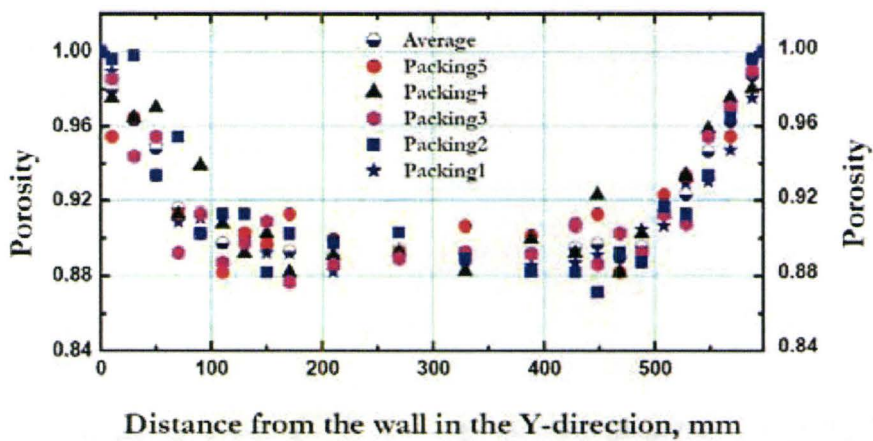


Figure 2.16: Porosity variation from the wall to the center for large shredded scrap (average scrap length 150 mm) in Y-direction

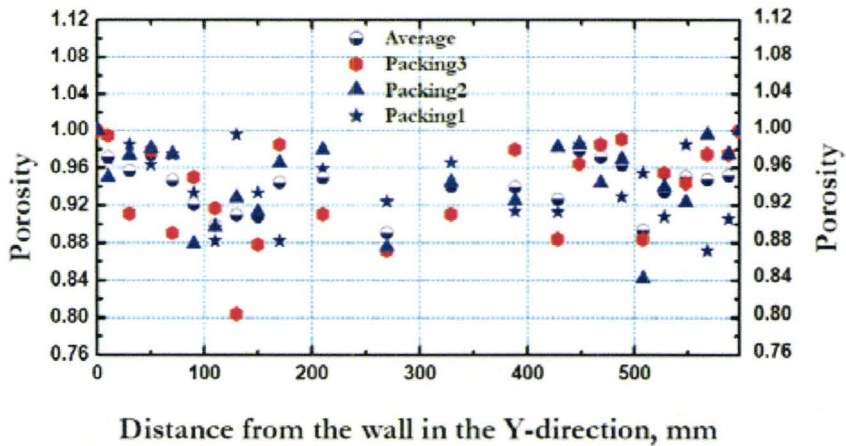


Figure 2.17: Porosity variation from the wall to the center for Busheling in Y-direction

The same experimental procedure was followed to observe the porosity distribution pattern for regular shaped spherical particles. Experiments were performed for both small spherical particles (diameter ~63 mm) and large spherical particles (diameter 195 mm). Figure 2.18 and 2.19 show the porosity distribution for small spherical particles and large spherical particles. It is seen in Figure 2.18, at the wall the porosity approaches 1 and at a distance of the average particle size, the porosity remains uniform. The same porosity distribution observed for shredded scrap. For large spherical particles porosity distribution is more random, which is similar to busheling.

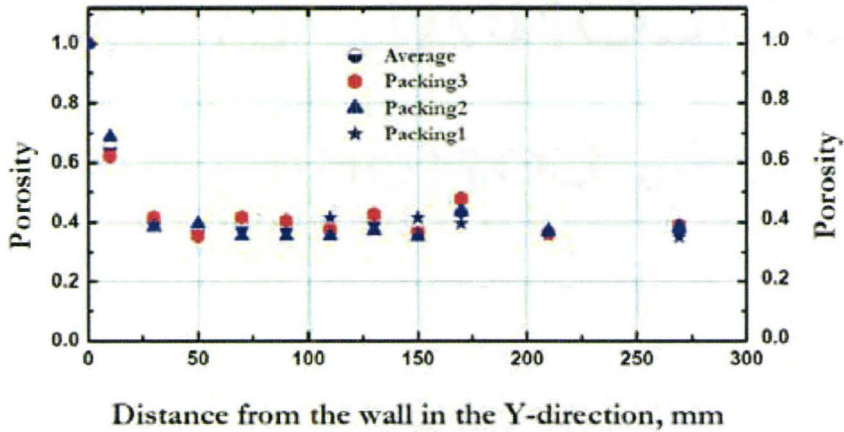


Figure 2.18: Porosity variation from the wall to the center for small spherical particles (diameter~63mm) in Y-direction

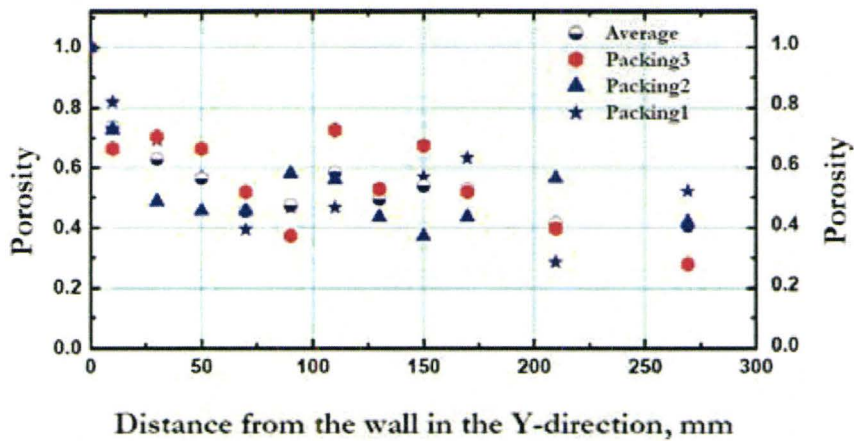


Figure 2.19: Porosity variation from the wall to the center for large spherical particles (diameter~195mm) in Y-direction

It is evident from our porosity measurements that there is anomaly of porosity distribution pattern for both busheling and large spherical shaped particles. This is due to large size of busheling and large spherical particles compared to the plexiglass vessel. During porosity measurement some amount of water can stick with the scarp and it is seen that about 0.13% error of total porosity if the scrap is dry, compared to wet scrap. If the water only stick in the first section i.e., near the wall then the porosity measurement error near the wall is about 3%.

From the present porosity distribution experiments it can be concluded that the porosity approaches 1 near the wall, and decreases towards the center of the bed, and remains constant after a particle length for both small shredded scrap and large shredded scrap.

2.5.3 Experiments to determine the extent of combustion

To predict temperature distribution inside the furnace, it is necessary to know the total amount of heat input to the furnace during scrap heating by the burner. As stated earlier, due to incomplete combustion, some unburned propane and oxygen or some carbon monoxide and oxygen can be present in the combustion products. To determine the burner power or total heat release during combustion, experiments were performed using off gas analysis to determine the extent of combustion.

A schematic of the off gas analysis set up is shown in Figure 2.20, which consists of scrap-heating furnace with scrap, burner, gas sampling pump, water vapor absorption column and a gas analyzer. Gas samples were taken using hollow a steel tube. Gas sampling positions are shown in Figure 2.21.

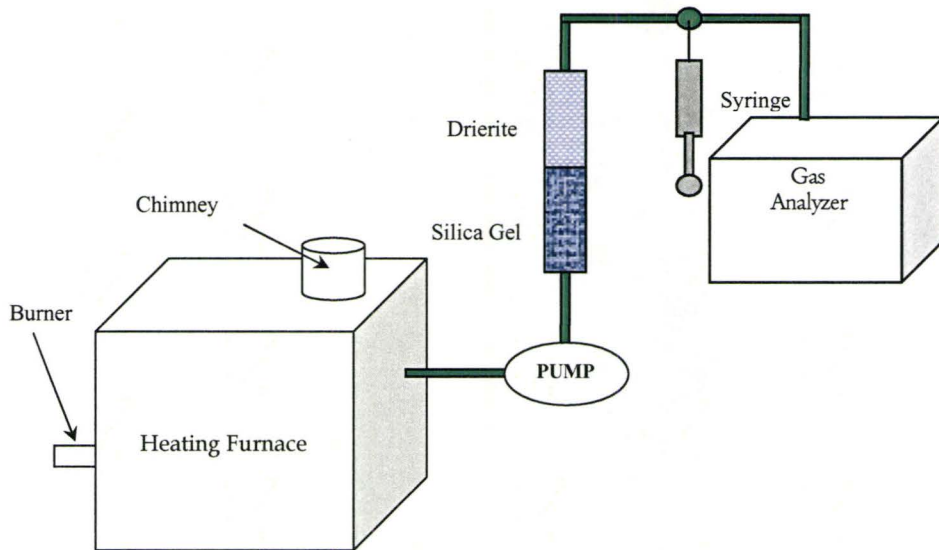


Figure 2.20: A schematic of the off gas analysis Experimental Set-up

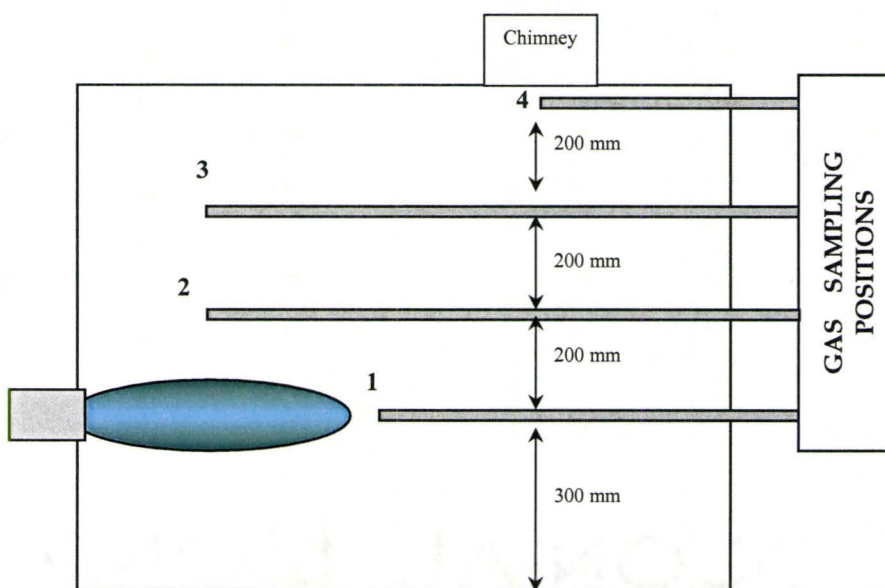


Figure 2.21: Gas sampling positions in the cross section of the center of the furnace.

At the beginning of the experiment, the furnace was purged by argon. During argon purging gas samples were taken from different positions shown in Figure 2.21 by a pump. It was observed that after 20 minutes of argon purging the furnace was almost free of oxygen in all the sampling positions (<1% oxygen), which is shown in Figure 2.22. After removing air from the furnace, the burner was started outside the furnace with oxygen and propane. To ensure complete combustion, an extra 10% oxygen over the required stoichiometry oxygen was supplied. Helium was used as a tracer gas in the burner. After a steady flame was achieved the burner was introduced to the furnace, and continuous gas samples were taken using a pump. Before gas sampling the gas mixture was passed through a column of silica gel and drierite to make sure that there is no water vapor in the gas mixture. A study of CO₂ adsorption/elution phenomena by different drying agents, which is presented in Appendix A., shows that precautions should be taken to ensure that samples of gas contain the true CO₂ content for chemical analysis. Gas samples were taken after passing the gas through the column of silica gel and drierite for 1.5 minutes, which ensure the true gas compositions of the samples. The only place from where the combustion products can go out from the furnace is chimney. Gas compositions at the chimney were monitored continuously.

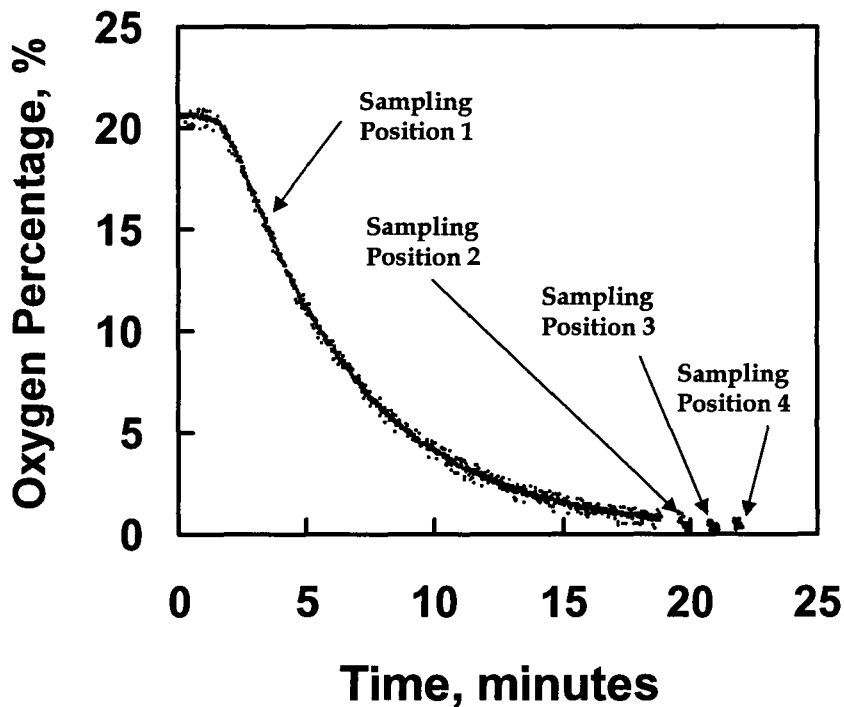


Figure 2.22: Oxygen percentage inside the furnace in different positions.

The carbon balance is related to the percent of combustion. The total carbon input is only from the propane and the carbon out is by CO_2 , CO or some un-burn propane. Exhaust gas compositions were checked through the experiment. It was found from that there is no CO present in the exhaust gas through chimney. Percent of combustion was calculated by the following equation;

$$\% \text{ Combustion} = 100(\text{Carbon Out in } \text{CO}_2) / (\text{Carbon in as } \text{C}_3\text{H}_8)$$

The experiment was repeated for different propane and oxygen flow rates. Figure 2.23 shows the calculated percent of combustion for different propane and oxygen flow rates, at different times. Virtually complete combustion is seen in Figure 2.23 for all the cases. Using a thermodynamic software FactSage5.5., 2007 and known propane and oxygen flow rates, thermodynamic calculations were performed to predict burner powers, which are summarized in Table 2.4. The burner powers for three different flow rates of propane and oxygen are 8.3 kW, 12.8kW and 17.3 kW, respectively.

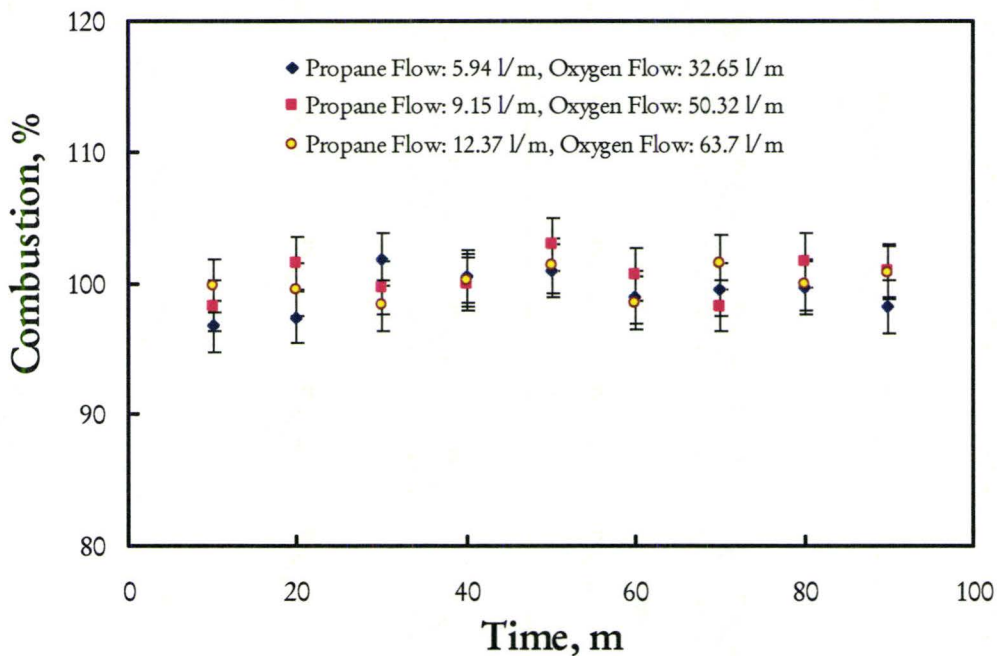


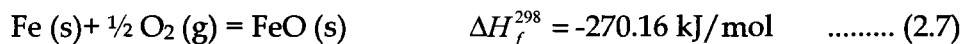
Figure 2.23: Percent of combustion for different propane and oxygen flow rate at 298.1 K and 1 atmospheric pressure.

Table 2.4: Propane and oxygen flow rates at 298.1K and 1 atmospheric pressure, with corresponding burner power (FactSage5.5., 2007)

C₃H₈ Flow Rate (l/min)	O₂ Flow Rate (l/m)	Excess O₂ (l/m)	Power (kW)
5.94	32.65	10%	8.3
9.15	50.32	10%	12.8
12.37	63.17*	2.1%	17.3

** Due to flame stability less than 10% of stoichiometry oxygen was used*

Steel scrap oxidizes during heating by burners. To estimate the extent of scrap oxidation iron oxides were collected after the heating experiment (small shredded scrap) with burner power of 12.8 kW. Equation 2.7 and 2.8 show the energy evolved during formation of FeO and Fe₂O₃, respectively (Janaf Thermochemical Tables, Third Edition, 1985). With the amount of iron oxide and equation 2.7 the energy evolved due to scrap oxidation was calculated, which is approximately 5% of total energy input during the experiment. Similarly, if the oxide is only Fe₂O₃ then the energy evolved due to oxidation is approximately 7% of total energy input during the experiment. The energy evolved due to scrap oxidation was small compared to the total energy input during the heating experiment and therefore scrap oxidation was neglected in this research.



2.5.4 Scrap Heating Experiments

At the beginning of the scrap heating experiment, steel scrap was carefully loaded into the furnace (Figure 2.2) and thermocouples were positioned at the pre-determined locations (Figure 2.6). Before starting the experiment, the furnace was purged with argon gas to make sure that there is no oxygen left inside the furnace. Then both the propane and oxygen supply lines were opened. The burner was then started. An excess oxygen was used, and accounted for in the reported burner power (Table 2.4). After a steady flame was obtained outside the furnace, the burner was inserted into the furnace. At the same time recording of the temperatures started. Precautions were taken to stop air entrainment into the furnace from the room environment by properly sealing the furnace.

Temperature measurements were repeated for different configurations of the furnace and with different scrap. Temperature distributions over the time of the experiments were monitored with furnace roof on and furnace roof off. Also, separate heating experiments were carried out with small shredded scrap, large shredded scrap, Busheling and Heavy Melt.

2.6 Experimental Results and Discussion

There were only 13 temperature measurements in the vertical central plane of the furnace, so the temperature distribution in the furnace was obtained by interpolating and extrapolating the temperatures with a software package, TECPLOT (Tecplot, 9.0). In front of the burner adiabatic flame temperature of propane and oxygen was used for the extrapolation. Thermocouples receive heat from the gas and radiate heat to the scrap so the measured temperature is between the gas and scrap temperatures. Therefore, the response of the thermocouples needs to be modeled. Modeling of thermocouple temperature, gas temperature and scarp temperature is discussed in Chapter 3, Section 3.9. The measured thermocouple temperature distributions over time for the large shredded scrap at the highest power level, 17.3 kW, are shown in Figures 2.24a to c. As expected the heat penetrates more deeply as time progresses.

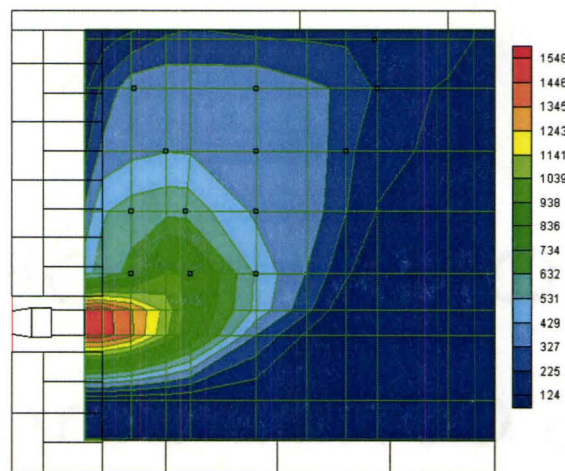


Figure 2.24a: Temperature ($^{\circ}\text{C}$) contour of the furnace after 30 minutes of the experiment with Large Shredded Scrap with top cover on, Burner Power 17.3 kW

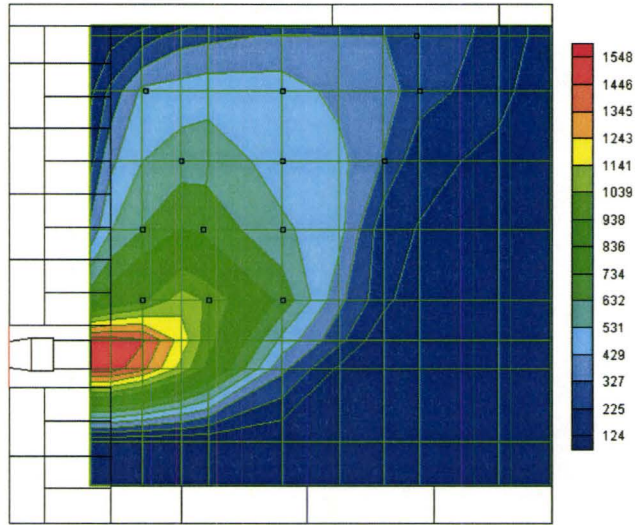


Figure 2.24b: Temperature ($^{\circ}\text{C}$) contour of the furnace after 60 minutes of the experiment with Large Shredded Scrap with top cover on, Burner Power 17.3 kW

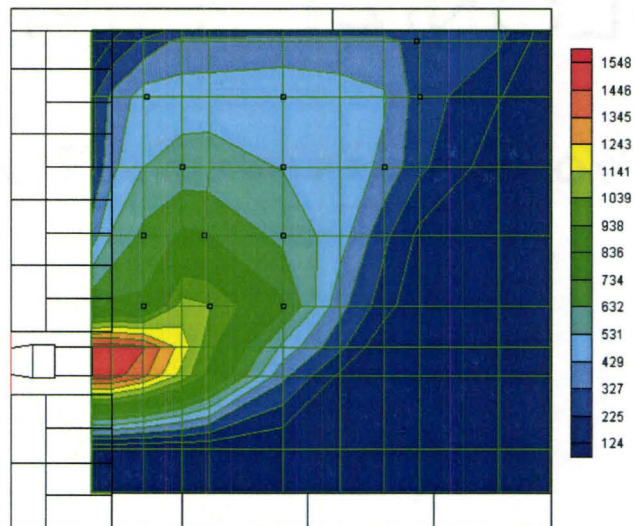


Figure 2.24c: Temperature ($^{\circ}\text{C}$) contour of the furnace after 90 minutes of the experiment with Large Shredded Scrap with top cover on, Burner Power 17.3kW

Figure 2.25 shows the effect of burner power on the gas temperatures 60 minutes after the start of heating; these Figures should be compared with Figure 2.24b at the highest power level, also after 60 minutes. As expected, more burner power produces more heating.

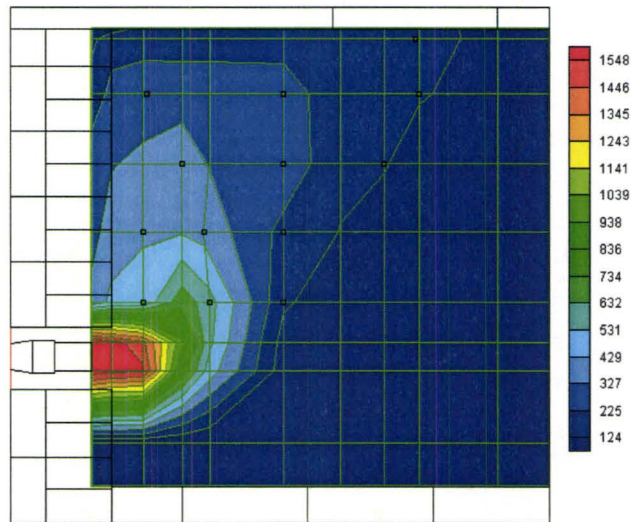


Figure 2.25a: Temperature ($^{\circ}\text{C}$) contour of the furnace after 60 minutes of the experiment with Large Shredded Scrap with top cover on, Burner Power 8.3 kW

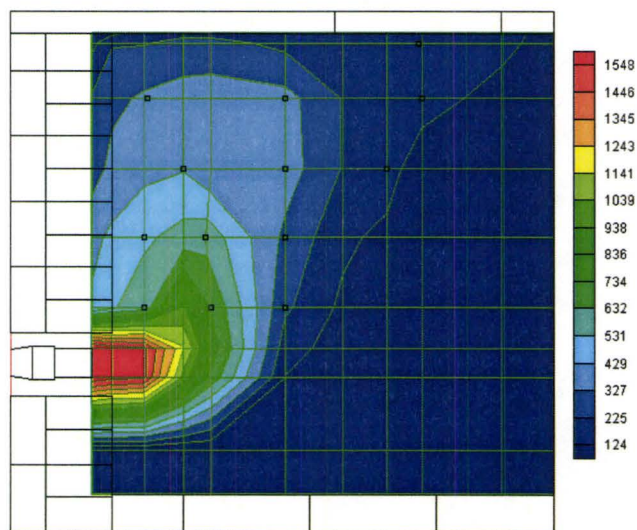


Figure 2.25b: Temperature ($^{\circ}\text{C}$) contour of the furnace after 60 minutes of the experiment with Large Shredded Scrap with top cover on, Burner Power 12.8 kW

The furnace roof causes the combustion gases to flow across the furnace to reach the chimney on the other side, as shown in Figure 2.18a. This changes the flow pattern and consequently the heating pattern, as can be seen by comparing Figure 2.26a (cover on) with 2.26b (cover off). There is better heating with the cover on because the contact length between the scrap and gas is increased.

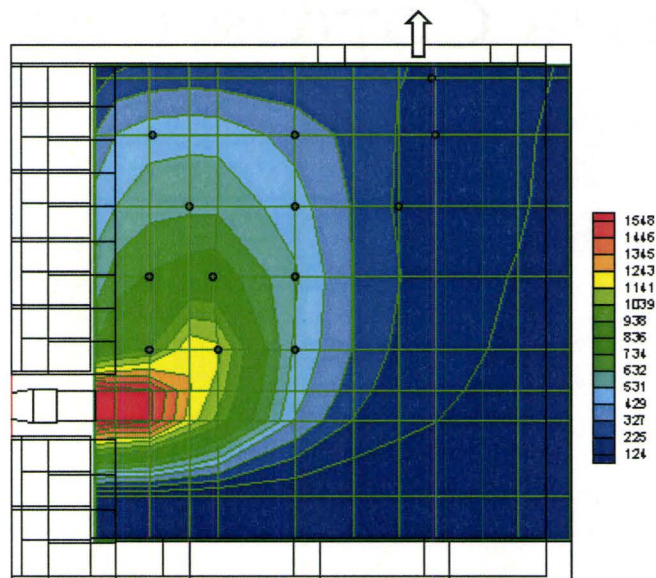


Figure 2.26a: Temperature (°C) contour of the furnace after 90 minutes of the experiment with Small Shredded Scrap with top cover on, Burner Power 12.8 kW

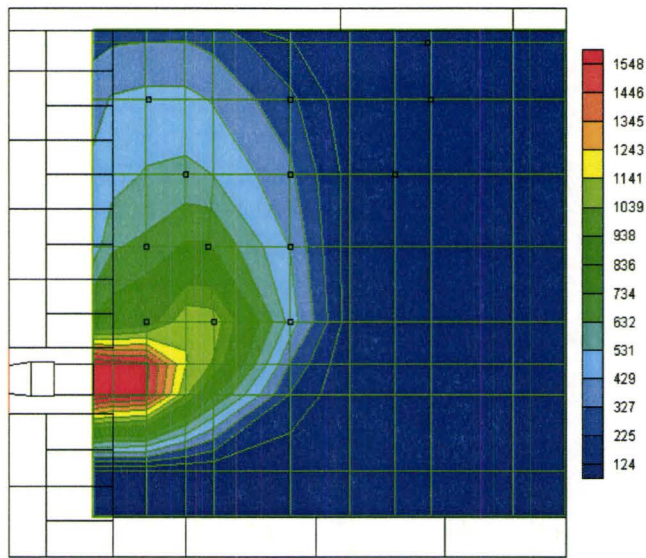


Figure 2.26b: Temperature ($^{\circ}\text{C}$) contour of the furnace after 90 minutes of the experiment with Small Shredded Scrap with top cover off, Burner Power 12.8 kW

Figure 2.27a to c shows the temperature contours for small shredded scrap, large shredded scrap and heavy melt, respectively. It is quite evident that the heating is more effective for smaller scrap. Figure 2.28 shows this more quantitatively. In Figure 2.28 the off gas temperature measured at the chimney is plotted as a function of time. If more heat is transferred to the scrap, the gas temperature will be lower. The apparent efficiency is simply calculated by comparing the off gas temperature to the

adiabatic flame temperature: $\eta_{app} = \frac{T_{flame} - (T_{exhaust} - T_{ambient})}{T_{flame}}$. Figure 2.28

shows that the efficiency decreases with time as the scrap heats up; the

thermal driving force is decreased. These efficiencies are very high because they are in the initial stages of heating.

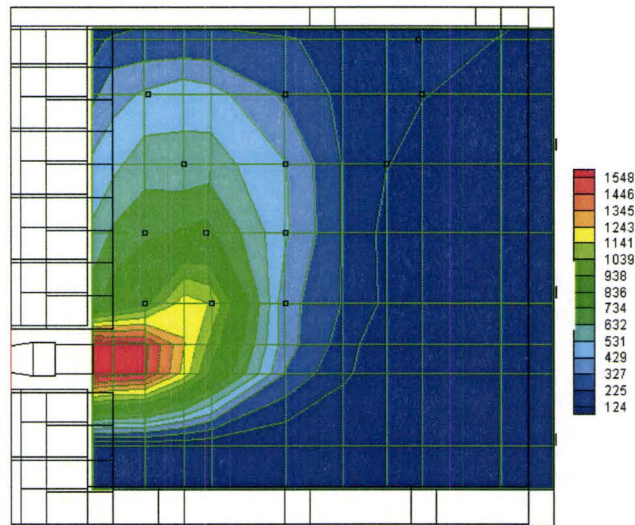


Figure 2.27a: Temperature ($^{\circ}\text{C}$) contour of the furnace after 60 minutes of the experiment with Small Shredded Scrap, top cover on, Burner Power 12.8 kW

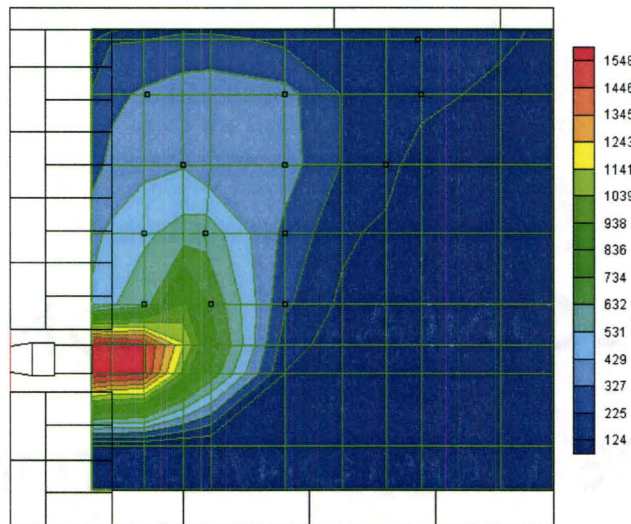


Figure 2.27b: Temperature ($^{\circ}\text{C}$) contour of the furnace after 60 minutes of the experiment with Large Shredded Scrap, top cover on, Burner Power 12.8 kW

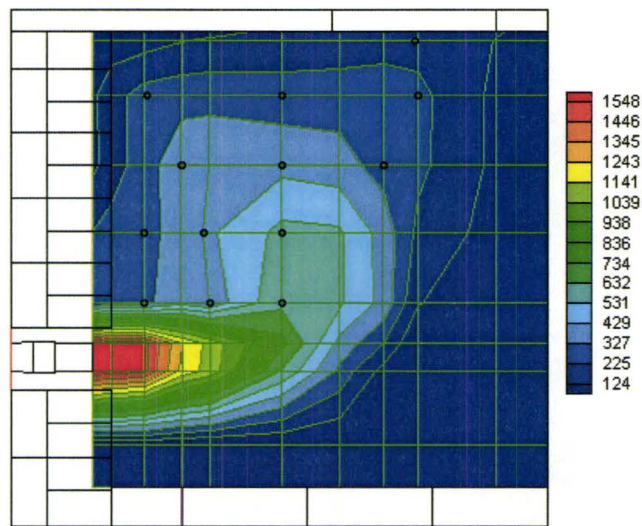


Figure 2.27c: Temperature ($^{\circ}\text{C}$) contour of the furnace after 60 minutes of the experiment with Heavy Melt, top cover on, Burner Power 12.8 kW

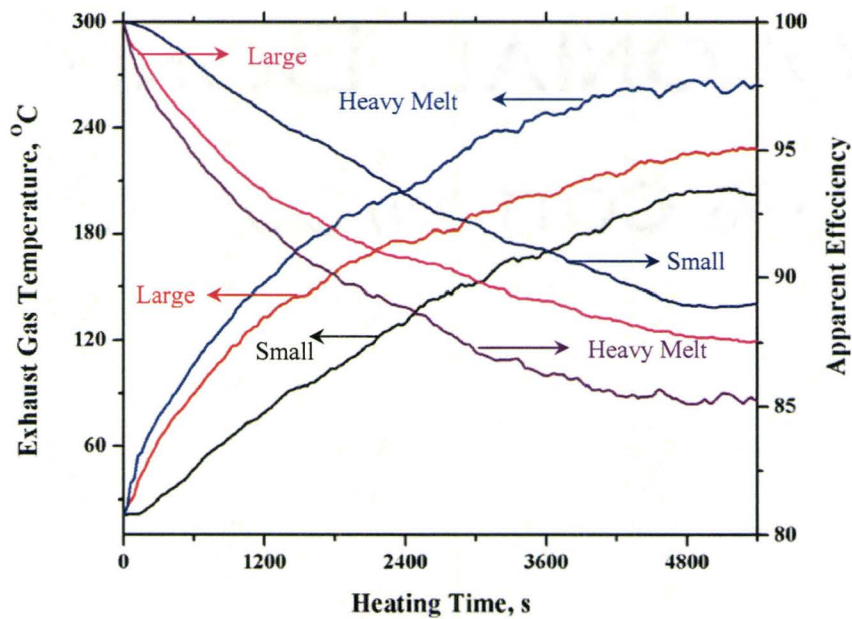


Figure 2.28: Plot of Exhaust Gas Temperature and Apparent Efficiency with Heating Time for Shredded (Small and Large) and Heavy Melt, Burner Power 12.8kW

To illustrate the effect of gas flow on the heating, a piece of steel sheet was placed in the centre of the scrap pile, as shown in Figure 2.29. The sheet had a clearance of 60 mm on each side, and 60 mm at the ends, so the combustion gases were forced to travel further through the scrap. The steel sheet had a dramatic effect on the heating, as seen by comparing Figures 2.30a (no sheet) with Figure 2.30b (with the sheet). Figure 2.31 shows the plot of outlet gas temperature and the apparent efficiency over time. Clearly, the steel sheet has a strong effect on flow modification, and the effectiveness of the heating. While, it is not practical to use this concept for the charging of an electric furnace, it could be useful for the design of separate scrap heating furnaces.

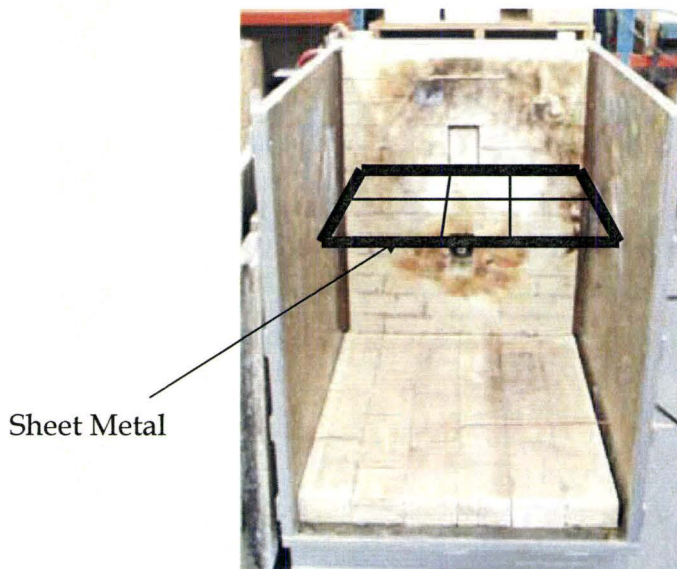


Figure 2.29: Sheet metal layer position during the experiment

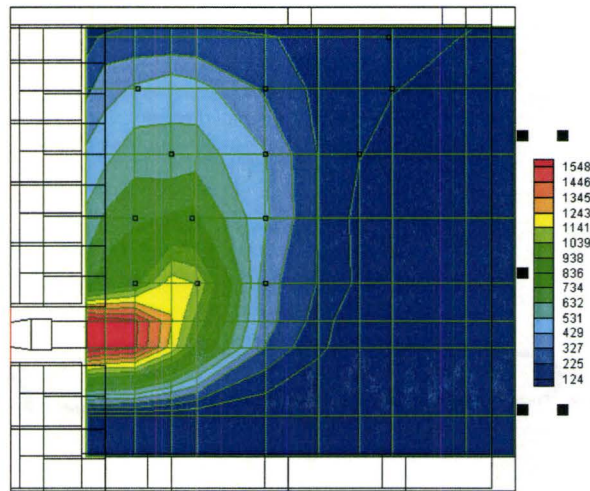


Figure 2.30a: Temperature (°C) contour of the furnace after 60 minutes of the experiment with Small Shredded scrap, top cover on, Burner Power 12.8 kW

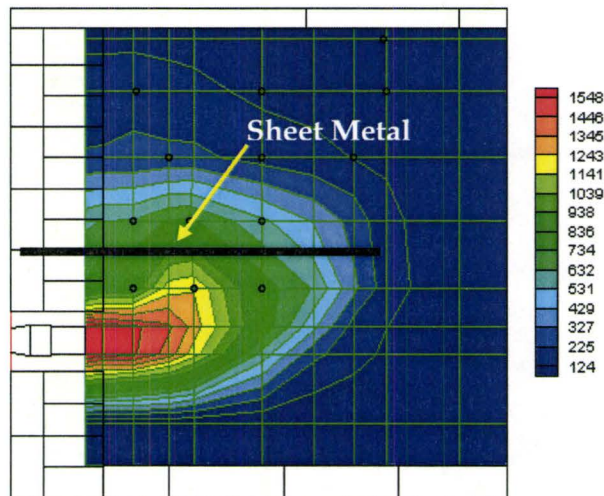


Figure 2.30b: Temperature (°C) contour of the furnace after 60 minutes of the experiment with small Shredded scrap and sheet metal layer, top cover on, Burner Power 12.8 kW

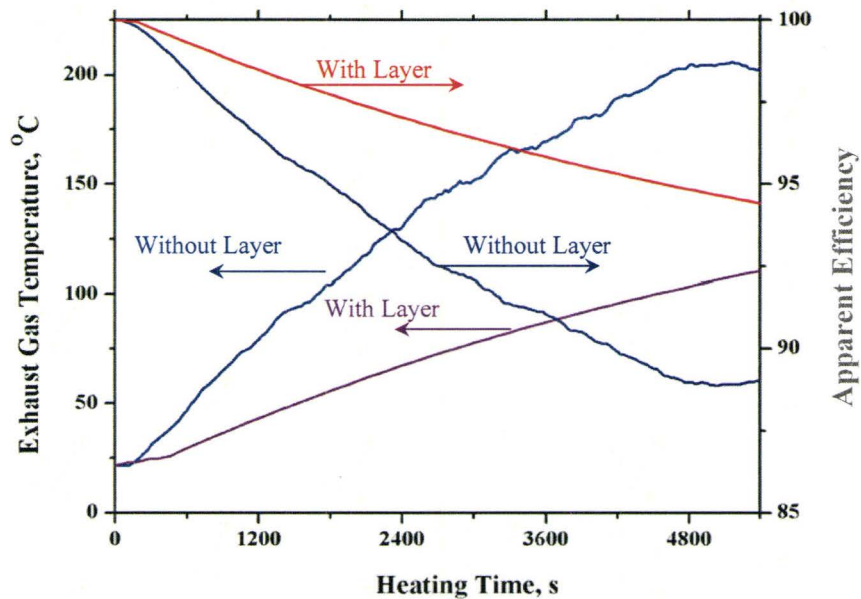


Figure 2.31: Plot of exhaust gas temperature and apparent efficiency with heating time, small shredded scrap, with sheet metal addition and without sheet metal addition, Burner Power 12.8 kW

To illustrate the effect of scrap layering on the heating, small shredded, large shredded, heavy melt and busheling were layered inside the furnace, as shown in Figure 2.32. Figure 2.33a to c shows the temperature contours for the above mentioned configuration. It is quite evident that the heating is more effective in the case of layering. When small shredded scrap is placed above the heavy melt and larger shredded scrap the small pieces go inside the voids and increased scrap density. Also in the top of the small scrap busheling acts as a sheet metal, hence better heating.

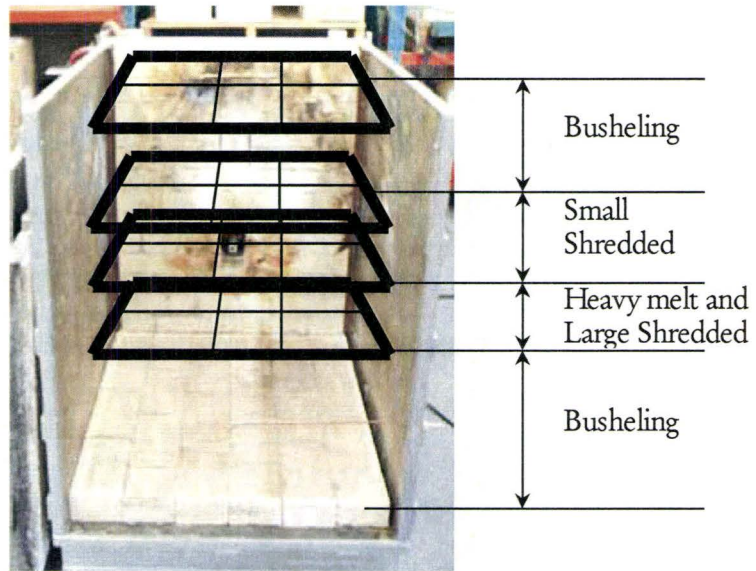


Figure 2.32: Scrap layering during the experiment

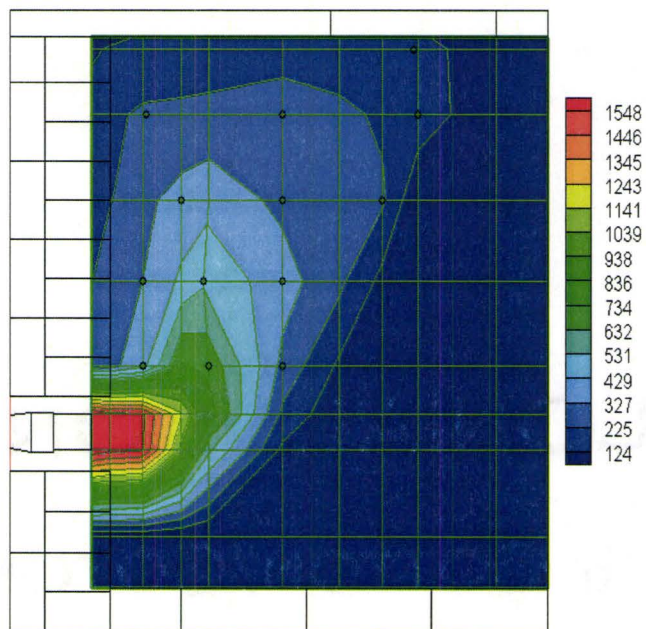


Figure 2.33a: Temperature ($^{\circ}\text{C}$) contour of the furnace after 30 minutes of the experiment with Scrap Layers, top cover on, Burner Power 12.8 kW

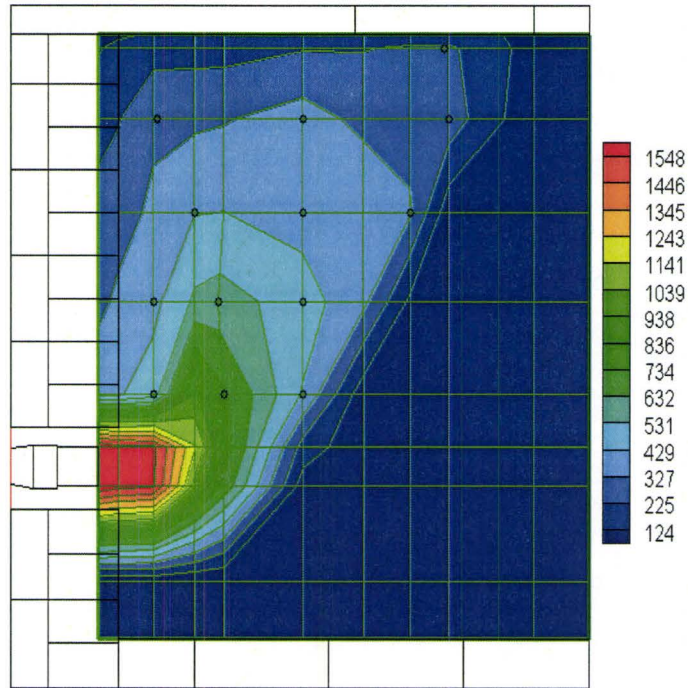


Figure 2.33b: Temperature ($^{\circ}\text{C}$) contour of the furnace after 60 minutes of the experiment with Scrap Layers, top cover on, Burner Power 12.8 kW

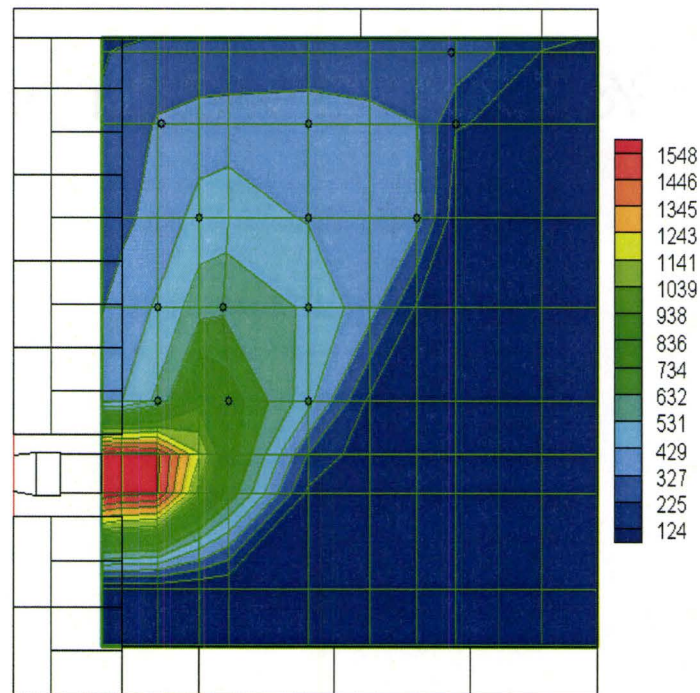


Figure 2.33c: Temperature ($^{\circ}\text{C}$) contour of the furnace after 90 minutes of the experiment with Scrap Layers, top cover on, Burner Power 12.8 kW

To check the reproducibility of present scrap heating experiments, an experiment was repeated for small shredded scrap with low burner power, i.e., 8.3 kW. It was mentioned earlier that temperatures were measured with heating time at 30 seconds interval. The exit gas temperatures i.e., thermocouple number 13 in Figure 2.6 are plotted with the time of heating for two tests, which is shown in Figure 2.34. Figure 2.35 shows the summary of absolute temperature deviation respect to steel melting point, for two tests in all the thermocouples for entire heating time. So, the heating experiments can be reproducible with the deviation of maximum 0-17.5%, which is shown in Figure 2.35.

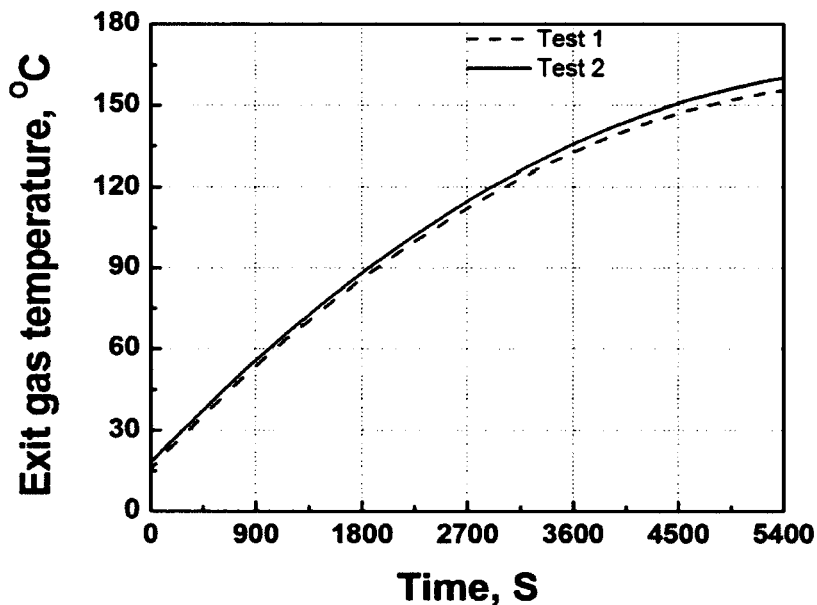


Figure 2.34: Exit gas temperature Vs time for test 1 and test two with small shredded scrap, top cover on, Burner Power 8.3 kW

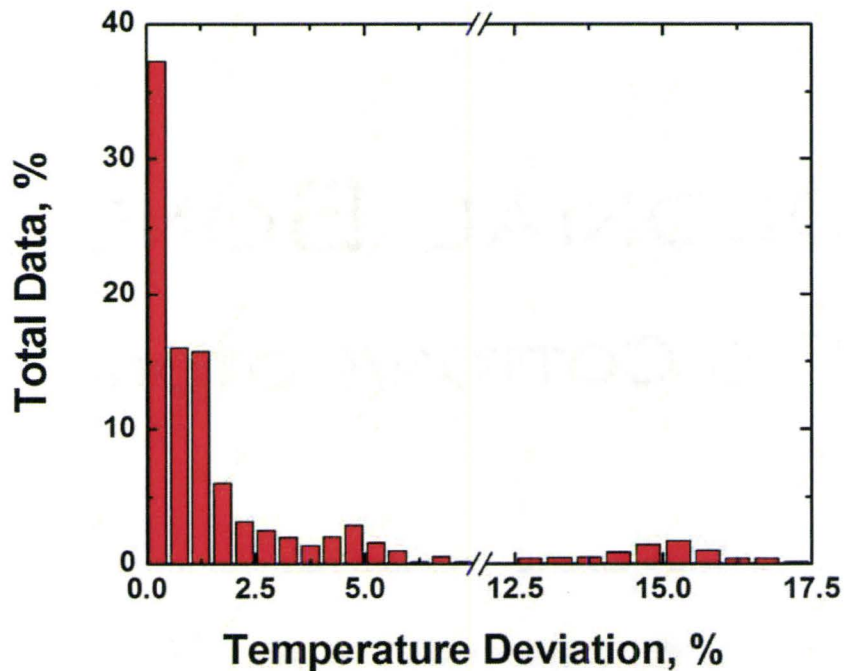


Figure 2.35: Summary of temperature deviation between test 1 and test 2 with small shredded scrap, top cover on, Burner Power 8.3kW

2.7 Summary of Scrap Heating Experiments

Present research was focused in the region of the Electric Arc Furnace around the burners. Hence, heating by electrode was ignored in this study. Also, it is important to mention that the aim of the present study was to measure the efficiency of heat transfer between the flame and scrap in the initial stages, not to melt the scrap. So, melting of scrap was not considered. Typically, there are three burners positioned in the cold spots between electrodes (Jones, 1994). Therefore, burner to burner interactions

were also ignored for the current research. Considering above mentioned phenomena an in-house scrap-heating furnace was designed and built in the lab to perform the scrap heating experiments.

Scrap heating experiments were carried out in the lab with small shredded scrap, large shredded scrap, busheling and heavy melt and different configurations. Temperature distributions were monitored over the time of the experiments using 13 thermocouples in the vertical center plane of the furnace, so the temperature distribution in the furnace was obtained by interpolating and extrapolating the temperatures with a software package, TECPLOT (Tecplot 9.0). The error of temperature measurements were within $\pm 0.5\%$. The main findings from the scrap heating experiments were;

1. Heat penetrated more deeply as time progressed for all kinds of scrap and more burner power produced more heating.
2. The furnace roof caused the combustion gases to flow across the furnace to reach the chimney on the other side, which changed the flow pattern and consequently the heating pattern. There was better heating with the furnace cover on compared to furnace cover off because the contact length between the scrap and gas was increased in case of furnace cover on.

3. Heating was more effective for small scrap compared to large scrap.
4. Apparent heating efficiency decreased with time as the scrap heated up; the thermal driving force was decreased. Measured efficiencies were very high because they were in the initial stage of heating.
5. A steel sheet placed horizontal in the middle of the furnace had a strong effect on flow modification, and the effectiveness of the heating, which could be used for the design of separate scrap heating furnaces.

Chapter 3

Numerical Modeling

3.1 Introduction

A numerical model is a set of equations, algebraic or differential, which may be used to represent and predict certain phenomena. In the last few decades, numerical modeling has played a key role in developing a holistic approach towards the understanding of metals and materials processing (Szekely, 1988). The term model as opposed to law implies that the relationship employed may not be quite exact and that the predictions derived from them may only be approximate. Numerical modeling has been used for a long time, but in recent years major breakthroughs have been possible because of dramatic developments both in computing hardware and software, which allows for more effective solution of the model equations.

Steel production in the Electric Arc Furnace (EAF) is a high temperature process and because of high temperature involved, it is difficult to measure the characteristics of the flow and heat transfer inside EAF. So, numerical modeling may be a viable reasonable alternative for

investigating fluid flow and heat transfer phenomena between a flame and scrap inside an EAF.

For accurate prediction of flow and temperature field for the scrap heating by burners variable porosity, non-Darcian, turbulent flow with separate temperatures for gas and solids need to be considered. FLUENT is not capable of considering the above mentioned conditions. To handle these issues an in-house computer model needs to be developed, which can take account of non-uniform porosity inside the furnace, turbulence, the dynamic behavior of porosity due to localized melting and heat transfer phenomena between the flame and scrap.

In this chapter a numerical model of the fluid flow and heat transfer phenomena between flame and scrap inside the EAF has been developed.

3.2 Porous Media Flow and Heat Transfer - Literature Review

Fluid flow and heat transfer phenomena through a porous medium have been extensively investigated due to its many engineering applications. In the present research an oxy-fuel burner, heats the scrap by transferring heat from the flame to the scrap. This heat transfer takes place via

convection, radiation from the combustion products and conduction within the scrap. Our present research is to understand the fluid flow and heat transfer phenomena in a non homogeneous porous medium with irregular shaped particles. Our aim is to understand the efficiency of the transfer of the combustion heat to the steel scrap in the furnace. So we neglect the detailed modeling of combustion and used hot gas as input to the furnace by the burner. In this Section a comprehensive review of available flow models for porous media is presented.

3.2.1 Porous Media Flow Models

The fluid flow characteristics of a fluid can be described mathematically by a set of equations considering two basic conservation principles, conservation of mass and conservation of momentum. For Newtonian fluid, the momentum equations for a single phase flow can be represented by the Navier-Stokes equations. Navier-Stokes equations in Cartesian coordinates of a fluid in laminar flow, can be expressed as (Versteeg and Malalasekera, 2007);

$$\frac{\partial(\rho V_i)}{\partial t} + \frac{\partial}{\partial x_j}(\rho V_i V_j) = -\frac{\partial P}{\partial x_i} + \frac{\partial}{\partial x_j}(\mu \frac{\partial V_i}{\partial x_j}) + \rho g_i \quad \dots\dots\dots (3.1)$$

The equation of continuity or the conservation of mass takes the following form provided there is no mass generation or loss.

$$\frac{\partial \rho}{\partial t} + \frac{\partial}{\partial x_j} (\rho V_j) = 0 \quad \dots\dots\dots (3.2)$$

In the Navier-Stokes equation 3.1, and continuity equation 3.2, the parameters t , P , ρ , μ , V , and g are time, pressure, fluid density, viscosity, velocity and acceleration due to gravity, respectively. When the system is a porous medium, then due to the great complexity of pores and solid matrix structure it is not possible to apply Navier-Stokes equations for prediction of flow characteristics. This problem led to the idea of the development of a mathematical description in terms of macroscopic features of fluid flow. The macroscopic momentum equations for porous media can be classified into two groups, Darcian and non-Darcian, which are described hereafter.

In the literature, different regimes of flow in porous media are characterized based on pore Reynolds number Re_p ($Re_p = \frac{V_d d_p}{\nu_f}$, where V_d is the Darcy velocity, d_p is the diameter of the pore and ν_f is the kinematic viscosity of the fluid). The Darcy velocity also known as the superficial velocity (flow rate/flow area). For low pore Reynolds number ($Re_p < 1$) incompressible flow through porous media can be described by Darcy's law (Darcy, 1856). In 1856, Darcy experimentally observed the pressure gradient and the speed of fluid through sand filters and he found that the

pressure drop is typically proportional to the velocity of the fluid. From Darcy's law, velocities for multi dimensional flows can be presented as

$$\vec{V}_d = -\frac{K}{\mu} \nabla P \quad \dots\dots\dots (3.3)$$

where K is the permeability of the medium, i.e., ability of a fluid to pass through a medium or material, μ is the viscosity of the fluid and ∇P is the pressure gradient. The mean filter velocity \vec{V}_d , is the Darcy velocity, which is proportional to pore velocity, V_p and described as; $\vec{V}_d = \phi \vec{V}_p$, where ϕ is the porosity of the medium. One of the main advantages of Darcy's law is that it linearizes the momentum equations, thus removing a considerable amount of difficulty in solving the governing equations. Darcy's law is valid for creeping type flows, where the Reynolds number is less than unity and inertia effects can be ignored in comparison to the viscous resistance (Greenkorn, 1981) or when the media is densely packed with low permeability $K \ll 1$, (Rudraiah and Balachandra, 1983) which implies that the pore Reynolds number Re_p , is less than unity. On the other hand, Darcy's law cannot account for the no-slip boundary condition on a rigid boundary (Hamdan, 1994). Darcy's law neglects the boundary and inertia effects (Bever and Sparrow 1969, Chandrasekher and Vortmeyer 1979, Brady 1984, Hassanizadeh and Gray 1987 and Yu. et al. 1991) of the medium. Some porous media, e.g., a scrap pile, has porosity close to unity

and the flow is fast, which makes the pore Reynolds number greater than unity. This type of porous medium needs special treatment where considerations of the inertial effects are important. In addition, Darcy's law does not account for the high velocity gradients, which arise when viscous effects are prominent. So, for proper flow prediction one should employ a non-Darcian equation, which can account both inertial and/ or viscous effects.

A review of single phase flow through porous media, presented by Hamaden, 1994, is summarized here. After Darcy, Lapwood (Lapwood, 1948) modified the Navier Stokes equations by replacing the viscous term $\mu \nabla^2 \vec{V}_d$ using the viscous damping term in Darcy's law, viz., $-\mu \vec{V}_d / K$ and proposed a flow model for porous media as;

$$\rho \frac{D\vec{V}_d}{Dt} = -\nabla P - \mu \frac{\vec{V}_d}{K} \dots\dots\dots (3.4)$$

The above model is known as the Darcy-Lapwood model. This model was appreciated by various researchers (Rudraiah and Srimani 1980, Rudraiah and Balachandra, 1983), who studied the nonlinear convection using this model. In contrast from the convection analysis point of view, some researchers have criticized the Darcy-Lapwood model for the way in which inertial term are included in the Navier Stokes equations.

Brinkman (Brinkman 1947a and Brinkman 1947b) proposed a modified Darcy’s law by investigating the flow around spherical particles. Brinkman accounted for viscous shear stresses that act on the fluid elements, which were neglected in Darcy’s law. The Brinkman model can be regarded as a modified Darcy’s law, which is presented here as the Darcy-Lapwood-Brinkman model,

$$\rho \frac{D\vec{V}_d}{Dt} = -\nabla P - \mu \frac{\vec{V}_d}{K} + \mu_{eff} \nabla^2 \vec{V}_d \quad \dots\dots\dots (3.5)$$

where, \vec{V}_d is the volume averaged Darcy velocity of the fluid within the porous medium, μ_{eff} is the effective viscosity of the fluid, and μ is the viscosity of the fluid. Arguments are available in the literature (Brinkman 1947a, Lundgren 1972, Hsu and Cheng 1985, and Durlafsky and Brady, 1987) supporting these two viscosities. On the other hand some researchers stated that the porous medium should retain its bulk properties and hence two viscosities are same in the Brinkman model. In the Darcy-Brinkman model the inertial term was neglected, but Forchheimer (Forchheimer, 1901) included the inertial loss term in the momentum equation in the form of $F\vec{V}_d |V_d|/\sqrt{K}$, where F is the drag coefficient or geometric factor. The Darcy-Lapwood-Forchheimer-Brinkman model can be presented as;

$$\rho \frac{D\vec{V}_d}{Dt} = -\nabla P - \mu \frac{\vec{V}_d}{K} + \mu_{eff} \nabla^2 \vec{V}_d - \rho \frac{F}{\sqrt{K}} \vec{V}_d |V| \quad \dots\dots\dots (3.6)$$

In the above equation $|V|$ is defined as $\sqrt{U^2 + V^2 + W^2}$, where, U , V and W are the Darcy velocities in x , y and z directions. Values of permeability, K , and drag coefficient, F , can be obtained from appropriate empirical relations, which are discussed later. In an effort to include Brinkman and Forchheimer extensions in the Darcy model, Beckermann et al (Beckermann, Viskanta and Ramadhyani, 1986) studied non-Darcian natural convection in a vertical enclosure filled with spherical shaped particles. They solved the Brinkman-Forchheimer-extended Darcy equation using the SIMPLE algorithm (Patankar, 1980) and their result showed good agreement with the data obtained from Weber's model (Weber, 1975). Similarly, to verify Brinkman-Forchheimer-extended Darcy model, Kladias and Prasad (Kladias and Prasad, 1991) conducted experiments over a wide range of governing parameters such as, Darcy Number ($Da=K/D^2$, where K is the permeability and D is the reference dimension), Forchheimer Number ($F_s = \frac{F}{D}$, where F is the drag coefficient of the Brinkman-Forchheimer-extended Darcy model, and D is the reference dimension), Prandtl Numbers ($P_r = \frac{\nu}{\alpha}$, which is ratio of the kinematic viscosity to thermal diffusivity) and conductivity ratio. Experimental results were reported for natural convection in a horizontal porous medium heated from the bottom. They achieved a good agreement

between the experimental results and the numerical prediction at low Darcy numbers and low Rayleigh numbers with variable porosity in the range 0.375 to 0.468. It is important to mention here that the Darcy-Lapwood-Forchheimer-Brinkman flow model for porous media is the best regarded model, because it takes into account both viscous and inertial terms (Hamdan, 1994).

For some applications, e.g., drying, the constant porosity assumption is valid. It is shown in the literature (Roblee, Baird and Tierney 1958 and Benenati and Brosilow, 1962) and also from our porosity experiments, which are described in Section 2.5.2, that a solid boundary influences the porosity distribution of the porous media. Porosity near the solid wall is high compared to center of the porous bed. In the literature a number of experimental and theoretical studies have shown that there is a significant effect on the velocity field of the high porosity near the solid wall (Roblee, Baird and Tierney 1958 and Benenati and Brosilow, 1962). Due to the variation of porosity near the solid wall, a channeling effect (Vafai , 1984) can be observed. This channeling effect was observed both experimentally and numerically by Vafai (1984) and Vafai et al (1986). So, for accurate flow prediction in porous media, consideration of variable porosity is important. A series of investigations in the literature (Hsu and Cheng 1990, Nithiarasu et al. 1997, Alazmi and Vafai 2000, Postelnicu and Rees

2003, Pakdee and Rattanadecho 2006, Chen et al. 2007) have considered the effect of variable porosity model on fluid flow and heat transfer for porous media to study both forced convection and natural convection. Vafai and Tien (Vafai and Tien, 1981) have established the steady state equations for a porous media using the local volume averaging technique and applied their equations of flow through a porous medium over a flat surface. Hsu and Cheng (1990) obtained the macroscopic momentum equations for forced convection of an incompressible flow in a variable porosity medium based on the volume averaging of the microscopic equations and used their model to analyze thermal dispersion in a porous medium. They compared their predicted heat transfer characteristics with experimental data reported in the literature (Yagi and Kunni, 1960). Considering the macroscopic mass and momentum balance, Nithiarasu et al (1997) derived a general set of governing equations of non-Darcian convective flow for a medium of variable porosity. They studied natural convective flow using their generalized non-Darcian porous media model and validated their model with the help of experimental data cited in the literature. Using a generalized non-Darcian model i.e., variable porosity model, Kladias and Prasad (1991) found good agreement between experimental results and predicted results for higher value of Darcy number as well as higher Rayleigh number. These authors also observed that the nature of the porosity variation of a medium affects heat transfer

and fluid flow results. The generalized non-Darcian flow model, which was used by above-mentioned researchers, can be described as;

$$\rho\phi\frac{\partial\vec{V}_P}{\partial t} + \rho\phi(\vec{V}_P \cdot \nabla)\vec{V}_P = -\nabla P - \frac{\mu\vec{V}_P}{K} + \mu_{eff} \cdot \nabla^2\vec{V}_P + \rho g\beta\Delta T - \frac{\rho F}{\sqrt{K}}|\vec{V}_P| \vec{V}_P \dots(3.7)$$

where, \vec{V} , ϕ , β and ΔT are the Darcy velocity, porosity, thermal expansion coefficient and temperature difference between the local temperature and the reference temperature. Other parameters of the generalized non-Darcian model have already described earlier.

It is important to mention here that the previous studies related to porous media flow and heat transfer were carried out considering regular shaped particles, either spheres or cylinders. Before the present study no one had taken any initiative for comprehensive modeling of the heat transfer and fluid flow phenomena for irregular shaped particles, such as steel scrap. It can be summarized from the literature that the flow through a porous medium can be explained accurately with the use of the generalized non-Darcian model in a variable porosity medium. The generalized non-Darcian model approaches the theory of porous media (Darcy's Law) as the permeability decreases, and it approaches the standard Navier-Stokes equations for a fluid as permeability increases; this is further explained in Section 3.4.2.

Now the question arises whether using fluid viscosity in the momentum equation for the effective viscosity is justified or not. In this regard there are several studies available in the literature for the turbulent flow through porous media for an incompressible fluid, which are presented next.

3.2.2 Turbulence Modeling in Porous Media

At low Reynolds number, flows are laminar and at high Reynolds number flows become turbulent. A typical point velocity measurement might demonstrate the form of, $U + u'(t)$, where U and $u'(t)$ are the mean velocity and fluctuating component of the velocity. In most engineering applications it is unnecessary to resolve the details of the turbulence fluctuations and only mean values of flow properties may characterize the turbulent flow (Versteeg and Malalasekera, 2007). Time averaged momentum equations yield Reynolds stresses of the form $\overline{\rho u'_i u'_j}$, which are not known a priori (Bird, Stewart and Lightfoot, 1994). Hence, there is a need for turbulence modeling. The most common turbulence models are classified into four groups (Versteeg and Malalasekera, 2007) which are summarized in Table 3.1.

Table 3.1: Turbulence Models (Versteeg and Malalasekera, 2007)

Turbulence Model	Name
Zero equation model	Mixing length model
One equation model	Spalart-Allmaras model
Two equations model	<i>k-ε</i> model <i>k-ω</i> model Algebraic stress model
Seven equations model	Reynolds stress model

Among the turbulence models the *k-ε* model is the most widely used and validated turbulence model for single phase flows (Versteeg and Malalasekera, 2007). In *k-ε* model for single phase Reynolds stresses are modeled by the mean velocity gradient, which is shown here;

$$-\rho \overline{u_i' u_j'} = \mu_T \left(\frac{\partial u_i}{\partial x_j} + \frac{\partial u_j}{\partial x_i} \right) - \frac{2}{3} \left(\rho k + \mu_T \frac{\partial u_i}{\partial x_i} \right) \delta_{ij} \quad \dots\dots\dots (3.8)$$

The transport equation of turbulent kinetic energy, *k* is as follows;

$$\frac{\partial(\rho k)}{\partial t} + \frac{\partial}{\partial x_i} (\rho k u_i) = \frac{\partial}{\partial x_j} \left(\frac{\mu_{eff}}{\sigma_k} \frac{\partial k}{\partial x_j} \right) + S_K \quad \dots\dots\dots (3.9)$$

In the above equations, $S_K = G_K - \epsilon\rho$ and σ_K is the *k-ε* model constant, where G_K is the volumetric rate of turbulence generation. The transport

equation of the rate of dissipation of turbulent kinetic energy ϵ is as follows;

$$\frac{\partial(\rho\epsilon)}{\partial t} + \frac{\partial}{\partial x_i}(\rho\epsilon u_i) = \frac{\partial}{\partial x_j} \left(\frac{\mu_{eff}}{\sigma_\epsilon} \frac{\partial \epsilon}{\partial x_j} \right) + S_\epsilon \dots\dots\dots (3.10)$$

where $S_\epsilon = \frac{C_1 \epsilon G_K - C_2 \rho \epsilon^2}{k}$. In which C_1 , C_2 and σ_ϵ are the k - ϵ model constants. The effective viscosity, μ_{eff} , is the sum of turbulent viscosity, μ_T , and laminar viscosity, μ_l , of the fluid. Turbulent viscosity, μ_T , is computed by combining k and ϵ as follows; $\mu_T = \rho C_\mu \frac{k^2}{\epsilon}$; where C_μ is the k - ϵ model constant. The values of k - ϵ model constants are as follows; $C_\mu = 0.09$, $C_1 = 1.44$, $C_2 = 1.92$, $\sigma_K = 1.0$ and $\sigma_\epsilon = 1.3$ (Launder and Spalding, 1974).

Turbulent phenomena in porous media are more complex compared to ordinary fluid flow. In the literature porous media flow regimes are classified as; (a) Darcy flow regime ($Re_p < 1$), (b) Forchheimer flow regime ($1 \sim 10 < Re_p < 150$), (c) transition flow regime ($150 < Re_p < 300$) and (d) fully turbulent flow regime ($Re_p > 300$) (Vafai et al, 2006). Different methodologies are described in the literature to develop turbulence models for flow in the porous media. Generally, governing equations for the mean velocity and turbulent properties are obtained by time averaging followed by volume averaging (Nakayama and Kuwahara 1999). Recently,

Francisco Jr. and Marcelo (2000), Pedras and Lemos (2001a) and Pedras and Lemos (2001b) developed double decomposition concept to obtain turbulent properties. Pedras and Lemos (Pedras and Lemos, 2001a), developed a two-equation turbulent model flow in porous media by space integration of the equations for turbulent flow for a single phase fluid, i.e., in the absence of porous media. They accounted for the porous media effect by considering additional terms in the turbulent kinetic energy and the dissipation rate equations. The turbulent kinetic energy, k , equation and dissipation rate of turbulent kinetic energy, ε , equation for porous media developed by Pedras and Lemos (Pedras and Lemos, 2001a), are presented.

$$\frac{\partial(\rho k)}{\partial t} + \frac{\partial}{\partial x_i}(\rho k u_i) = \frac{\partial}{\partial x_j} \left(\frac{\mu_{eff}}{\sigma_k} \frac{\partial k}{\partial x_j} \right) + S_K \quad \dots\dots\dots (3.11)$$

$$\frac{\partial(\rho \varepsilon)}{\partial t} + \frac{\partial}{\partial x_i}(\rho \varepsilon u_i) = \frac{\partial}{\partial x_j} \left(\frac{\mu_{eff}}{\sigma_\varepsilon} \frac{\partial \varepsilon}{\partial x_j} \right) + S_\varepsilon \quad \dots\dots\dots (3.12)$$

where, $S_K = G_K - \varepsilon \rho + C_K \rho \phi \frac{k |V_j|}{\sqrt{K}}$ and $S_\varepsilon = \frac{C_1 \varepsilon G_K - C_2 \rho \varepsilon^2}{k} + C_2 C_K \rho \phi \frac{\varepsilon |V_j|}{\sqrt{K}}$.

To obtain the value of C_K the same authors (Pedras and Lemos, 2001b) numerically solved the microscopic flow inside a special periodic array of elliptical rods, considering low and high Reynolds numbers and varying porosity from 0.4 to 0.8. Nield (Nield, 2001), presented a summary and discussion on the alternative turbulence models for flow through a porous

medium and he concluded that Pedras and Lemos (Pedras and Lemos 2001a, Pedras and Lemos 2001b) analysis can be considered as more complete.

3.2.3 Porous Media Thermal Models

A review of literature in the area of fluid flow and heat transfer for porous media indicates that it is a common practice to adopt the concept of local thermal equilibrium (LTE) between fluid and solid in the porous media. This local thermal equilibrium assumption implies that the local temperature difference between fluid and solid in the porous media is negligible. The local thermal equilibrium model can be presented as;

$$(\rho C)_m \frac{\partial T}{\partial t} + \phi(\rho C)_f \vec{V}_p \cdot \nabla T = K_{eff} \nabla^2 T + S_E \dots\dots\dots(3.13)$$

Where, $(\rho C)_m = \phi(\rho C)_f + (1-\phi)(\rho C)_s$ and $K_{eff} = \phi K_f + (1-\phi)K_s$ f and s imply for fluid and solid. C , T , and S_E are the specific heat, temperature, and heat source term, respectively. The velocity in equation 3.13 was considered as Darcy's velocity.

The assumption of LTE is widely used in the literature to analyze thermal transport in a porous medium. However, this assumption is not valid for applications where a significant temperature difference exists between the solid and the fluid phases. Hence, the need for local thermal non equilibrium (LTNE) models. In recent years the LTNE model has received

considerable attention due to its application in a wide variety of engineering fields. The LTNE model in porous media has been investigated by a number of investigators such as Sozen and Vafai (1990), Amiri and Vafai (1994), Quintard, Kaviany and Whitaker (1997). They showed that consideration of the LTNE model is necessary for accurate temperature prediction. This type of model requires an additional term in each equation to account the energy exchange between solid and fluid, the heat transfer coefficient, h_{fs} . The heat transfer coefficient between fluid to solid, h_{fs} , and the specific surface area, A_s are the main resistance of heat transfer in the interface between fluid and solid. Considering LTNE the energy equations for fluid and solid phases can be represented as;

$$\phi(\rho C)_f \frac{\partial T_f}{\partial t} + \phi(\rho C)_f \vec{V}_p \cdot \nabla T_f = K_{seff} \nabla^2 T_f + h_{fs} A_s (T_s - T_f) + S_E \dots\dots\dots(3.14)$$

$$(1 - \phi)(\rho C)_s \frac{\partial T_s}{\partial t} = K_{seff} \nabla^2 T_s + h_{fs} A_s (T_f - T_s) - \nabla q^r \dots\dots\dots(3.15)$$

In the LTNE energy equations, ϕ , ρ , C , T , K_{seff} , h_{fs} , A_s , K_{seff} and q^r are the porosity, density, specific heat, temperature, effective thermal conductivity of the fluid, interface heat transfer coefficient between fluid and solid, specific surface area, effective thermal coefficient of the solid and radiation term, respectively. Subscript f is for the fluid and s is for the solid phase. Thermo physical properties in the energy equations can be determined by either experimental work reported in the literature or using models, which are discussed in detail in Section 3.4.

3.3 Model Equations

Nithiarasu et al. (1997) derived a general set of 2-dimensional, governing equations of non-Darcian natural convective flow in a medium of variable porosity. Based on their concept, a 3-dimensional general set of governing equations are derived here. Mass and momentum balances for 3-dimensional flow in a fluid saturated medium of variable porosity were performed. The medium was assumed isotropic with constant physical properties.

A control volume of lengths Δx , Δy and Δz was considered for the mass and momentum balance. Let, a_f be the fraction of area available for flow per unit cross sectional area. For isotropic porous media, a_f is same in all the directions, which is equal to the local bed porosity, ϕ , but a_f varies from location to location. The flow area available in the x , y and z -directions for the control volume are $a_f \Delta y \Delta z$, $a_f \Delta x \Delta z$ and $a_f \Delta x \Delta y$, respectively. The average fluid velocities over the control volume faces in x , y and z directions were considered as u_f , v_f and w_f . u_f , v_f and w_f are the pore velocities.

The mass balance over the control volume ($\Delta x \Delta y \Delta z$) can be written as;

$$\begin{aligned} \frac{\partial}{\partial t} (\rho a_f \Delta x \Delta y \Delta z) = & \rho u_f a_f \Delta y \Delta z |_x - \rho u_f a_f \Delta y \Delta z |_{x+\Delta x} + \rho v_f a_f \Delta x \Delta z |_y - \\ & \rho v_f a_f \Delta x \Delta z |_{y+\Delta y} + \rho w_f a_f \Delta x \Delta y |_z - \rho w_f a_f \Delta x \Delta y |_{z+\Delta z} \end{aligned}$$

..... (3.16)

Equation 3.16 can be re-written as;

$$\frac{\partial}{\partial t}(\rho a_f \Delta x \Delta y \Delta z) = -\frac{\partial}{\partial x}(\rho u_f a_f \Delta x \Delta y \Delta z) - \frac{\partial}{\partial y}(\rho v_f a_f \Delta x \Delta y \Delta z) - \frac{\partial}{\partial z}(\rho w_f a_f \Delta x \Delta y \Delta z) \dots\dots\dots 3.17)$$

Or $\frac{\partial}{\partial t}(\rho \phi) + \frac{\partial}{\partial x}(\rho \phi u_f) + \frac{\partial}{\partial y}(\rho \phi v_f) + \frac{\partial}{\partial z}(\rho \phi w_f) = 0 \dots\dots\dots(3.18)$

The superficial volume averaged fluid velocity (Nield and Bejan, 1992) can be defined as $u = \phi u_f$, $v = \phi v_f$, and $w = \phi w_f$.

Ignoring non-Darcian effects and the gravitational force, an x-momentum balance was performed. The rate of momentum in at the face of control volume ($\Delta x \Delta y \Delta z$), at x is $\rho u_f u_f a_f \Delta y \Delta z |_x$ and the rate of momentum out at $x + \Delta x$ is $\rho u_f u_f a_f \Delta y \Delta z |_{x + \Delta x}$. Similarly, the rate of momentum in at the face of control volume, at y, $y + \Delta y$, z and $z + \Delta z$ can be written as $\rho u_f v_f a_f \Delta x \Delta z |_y$, $\rho u_f v_f a_f \Delta x \Delta z |_{y + \Delta y}$, $\rho u_f w_f a_f \Delta x \Delta y |_z$ and $\rho u_f w_f a_f \Delta x \Delta y |_{z + \Delta z}$, respectively. Using molecular transport x component of momentum accumulation (in-out) in the control volume can be written as;

$$(\rho a_f \Delta y \Delta z) [\tau_{xx|x} - \tau_{xx|x + \Delta x}] + (\rho a_f \Delta x \Delta z) [\tau_{yy|y} - \tau_{yy|y + \Delta y}] + (\rho a_f \Delta x \Delta y) [\tau_{zz|z} - \tau_{zz|z + \Delta z}] \dots\dots\dots(3.19)$$

The resultant force of fluid pressure in the x-direction is $(\rho a_f \Delta y \Delta z) [P_{|x} - P_{|x + \Delta x}]$. Now, rate of accumulation of x momentum is;

$a_f \Delta x \Delta y \Delta z \frac{\partial(u_f \rho)}{\partial t}$. Using equation 3.19, resultant force and rate of accumulation of x momentum equations were derived.

Considering Newtonian and incompressible fluid in the Cartesian coordinate system, the governing equations of flow, turbulence (k - ϵ) and energy conservation for porous medium at under unsteady state are presented here.

In generalized non-Darcian porous media momentum equations, the source term is composed with two terms, a viscous loss term and an inertial loss term. The momentum equations, which are considered for the present research, are described here.

Conservation equation of momentum in the x-direction, can be represented as;

$$\begin{aligned} \frac{\partial(\phi \rho u_f)}{\partial t} + \frac{\partial(\phi \rho u_f u_f)}{\partial x} + \frac{\partial(\phi \rho u_f v_f)}{\partial y} + \frac{\partial(\phi \rho u_f w_f)}{\partial z} = -\frac{\partial P}{\partial x} + \frac{\partial}{\partial x} \left(\mu_{eff} \frac{\partial u_f}{\partial x} \right) + \\ \frac{\partial}{\partial y} \left(\mu_{eff} \frac{\partial u_f}{\partial y} \right) + \frac{\partial}{\partial z} \left(\mu_{eff} \frac{\partial u_f}{\partial z} \right) - \frac{\mu}{K} u_f - \frac{\rho F}{\sqrt{K}} |u| u_f \end{aligned} \tag{3.20}$$

The model parameters ϕ , μ_{eff} , F and K are the porosity, effective viscosity of the fluid ($= \mu_l + \mu_T$), which is the sum of laminar viscosity of the fluid

(μ) and the turbulent viscosity of the fluid (μ_T), drag coefficient and permeability, respectively. In equation 3.20, $|u|$ is can be defined as $\sqrt{u_f^2 + v_f^2 + w_f^2}$. Considerations of model parameters are discussed in Section 3.4.

The conservation equation of momentum in the y-direction, can be represented as;

$$\begin{aligned} \frac{\partial(\phi\rho v_f)}{\partial t} + \frac{\partial(\phi\rho v_f u_f)}{\partial x} + \frac{\partial(\phi\rho v_f v_f)}{\partial y} + \frac{\partial(\phi\rho v_f w_f)}{\partial z} = & -\frac{\partial P}{\partial x} + \frac{\partial}{\partial x}\left(\mu_{eff} \frac{\partial v_f}{\partial x}\right) + \frac{\partial}{\partial y}\left(\mu_{eff} \frac{\partial v_f}{\partial y}\right) \\ & + \frac{\partial}{\partial z}\left(\mu_{eff} \frac{\partial v_f}{\partial z}\right) - \frac{\mu}{K} v_f - \frac{\rho F}{\sqrt{K}} |v| v_f + \rho g \beta \Delta T \end{aligned} \dots\dots\dots (3.21)$$

Standard model parameters are similar to the x-momentum equation. The last term on the right hand side of y-momentum equation is the extra source term due to buoyancy, where, g , β and ΔT are the acceleration due to gravity, thermal expansion coefficient and temperature difference between local temperature and reference temperature. The importance of buoyancy forces in a mixed convection flow can be determined by the ratio of Grashof and the square of Reynolds numbers as;

$$\frac{Gr}{Re^2} = \frac{g\beta\Delta TL}{u^2} \dots\dots\dots (3.22)$$

where L is the characteristic length. When the ratio approaches or exceeds unity, then there is a strong buoyancy contribution to the flow. In this

situation the ratio is well above unity, so buoyancy dominates. The buoyancy term is obtained using the Boussinesq approximation. This approximation treats density as a constant value everywhere, except for the buoyancy term in the momentum equation;

$$(\rho_i - \rho)g \approx -\rho g\beta(T - T_o) \dots\dots\dots (3.23)$$

In the above equation ρ is the constant density of the fluid, T_o is the operating or reference temperature, and β is the thermal expansion coefficients. Equation 3.23 can be obtained using Boussinesq approximation of $\rho_i = \rho(1 - \beta\Delta T)$.

The conservation equation of momentum in the z-direction, can be represented as;

$$\begin{aligned} \frac{\partial(\phi\rho w_f)}{\partial t} + \frac{\partial(\phi\rho w_f u_f)}{\partial x} + \frac{\partial(\phi\rho w_f v_f)}{\partial y} + \frac{\partial(\phi\rho w_f w_f)}{\partial z} = & -\frac{\partial P}{\partial x} + \frac{\partial}{\partial x}\left(\mu_{eff} \frac{\partial w_f}{\partial x}\right) + \frac{\partial}{\partial y}\left(\mu_{eff} \frac{\partial w_f}{\partial y}\right) \\ & + \frac{\partial}{\partial z}\left(\mu_{eff} \frac{\partial w_f}{\partial z}\right) - \frac{\mu}{K}w_f - \frac{\rho F}{\sqrt{K}}|w|w_f \end{aligned} \dots\dots\dots (3.24)$$

In this work the modified two equations $k-\varepsilon$ model of Pedras and Lemos (Pedras and Lemos 2001a, Pedras and Lemos 2001b) are used to estimate the turbulence parameters. The model incorporates an equation for the conservation of turbulence kinetic energy, k and its dissipation rate, ε . The $k-\varepsilon$ transport equations in terms of Cartesian co-ordinate system are expressed as;

Conservation equation of turbulent kinetic energy, can be represented as;

$$\frac{\partial(\rho k)}{\partial t} + \frac{\partial}{\partial x}(\rho k u_f) + \frac{\partial}{\partial y}(\rho k v_f) + \frac{\partial}{\partial z}(\rho k w_f) = \frac{\partial}{\partial x}\left(\frac{\mu_{eff}}{\sigma_k} \frac{\partial k}{\partial x}\right) + \frac{\partial}{\partial y}\left(\frac{\mu_{eff}}{\sigma_k} \frac{\partial k}{\partial y}\right) + \frac{\partial}{\partial z}\left(\frac{\mu_{eff}}{\sigma_k} \frac{\partial k}{\partial z}\right) + S_K + S_{Pk}$$

..... (3.25)

Where $S_K = G_K - \varepsilon\rho$ and $S_{Pk} = C_K\rho\phi\frac{k|u|}{\sqrt{K}}$. The σ_K is the $k-\varepsilon$ model constant.

The model parameter C_K is obtained from Pedras and Lemos (Pedras and Lemos 2001b) work. Again, $|u|$ is $\sqrt{u_f^2 + v_f^2 + w_f^2}$ and K is the permeability of the medium. ε and G_K are the dissipation rate of turbulent kinetic energy and volumetric rate of turbulence generation. For three dimensional Cartesian co-ordinates system, G_K is;

$$G_K = 2\mu_T\left[\left(\frac{\partial u_f}{\partial x}\right)^2 + \left(\frac{\partial v_f}{\partial y}\right)^2 + \left(\frac{\partial w_f}{\partial z}\right)^2\right] + \mu_T\left[\left(\frac{\partial u_f}{\partial y} + \frac{\partial v_f}{\partial x}\right)^2 + \left(\frac{\partial v_f}{\partial z} + \frac{\partial w_f}{\partial y}\right)^2 + \left(\frac{\partial u_f}{\partial z} + \frac{\partial w_f}{\partial x}\right)^2\right]$$

..... (3.26)

The conservation equation for the dissipation rate of turbulent kinetic energy, can be represented as;

$$\frac{\partial(\rho\varepsilon)}{\partial t} + \frac{\partial}{\partial x}(\rho\varepsilon u_f) + \frac{\partial}{\partial y}(\rho\varepsilon v_f) + \frac{\partial}{\partial z}(\rho\varepsilon w_f) = \frac{\partial}{\partial x}\left(\frac{\mu_{eff}}{\sigma_\varepsilon} \frac{\partial \varepsilon}{\partial x}\right) + \frac{\partial}{\partial y}\left(\frac{\mu_{eff}}{\sigma_\varepsilon} \frac{\partial \varepsilon}{\partial y}\right) + \frac{\partial}{\partial z}\left(\frac{\mu_{eff}}{\sigma_\varepsilon} \frac{\partial \varepsilon}{\partial z}\right) + S_\varepsilon + S_{P\varepsilon}$$

..... (3.27)

where, $S_\epsilon = \frac{C_1 \epsilon G_K - C_2 \rho \epsilon^2}{k}$ and $S_{p\epsilon} = C_2 C_K \rho \phi \frac{\epsilon |u|}{\sqrt{K}}$. In which C_1 , C_2 and σ_ϵ

are the k - ϵ model constant. The turbulent viscosity, μ_T is computed by the

combining k and ϵ as follows. $\mu_T = \rho C_\mu \frac{k^2}{\epsilon}$; (Launder and Spalding, 1974)

where C_μ is the k - ϵ model constant. The values of model constants are;

$C_1=1.44$, $C_2 =1.92$, $C_K=0.28$, $\sigma_K =1.0$ and $\sigma_\epsilon =1.3$ (Launder and Spalding,

1974).

Considering local thermal non equilibrium (LTNE) between fluid and solid in the porous media the energy equations can be written as;

Fluid Energy Equation can be written as:

$$\phi(\rho C)_f \frac{\partial T_f}{\partial t} + \frac{\partial}{\partial x}(\phi u_f C \rho T)_f + \frac{\partial}{\partial y}(\phi v_f C \rho T)_f + \frac{\partial}{\partial z}(\phi w_f C \rho T)_f = \dots \dots \dots (3.28)$$

$$K_{eff} \left(\frac{\partial^2 T_f}{\partial x^2} + \frac{\partial^2 T_f}{\partial y^2} + \frac{\partial^2 T_f}{\partial z^2} \right) + h_{fs} A_s (T_s - T_f) + S_E$$

Solid Energy Equation can be written as:

$$(1 - \phi)(\rho C)_s \frac{\partial T_s}{\partial t} = K_{eff} \left(\frac{\partial^2 T_s}{\partial x^2} + \frac{\partial^2 T_s}{\partial y^2} + \frac{\partial^2 T_s}{\partial z^2} \right) - \left(\frac{\partial q_r}{\partial x} + \frac{\partial q_r}{\partial x} + \frac{\partial q_r}{\partial x} \right) + h_{fs} A_s (T_f - T_s) \dots \dots \dots (3.29)$$

In the fluid and solid energy equations ϕ , ρ , C , K_{eff} , h_{fs} , A_s , K_{eff} and q_r are the porosity, density, specific heat, effective thermal conductivity of the

fluid, heat transfer coefficient between fluid and solid, specific surface area, effective thermal conductivity of solid and radiation terms, respectively.

In the model equations model parameters i.e., porosity (ϕ), permeability (K), drag coefficient (F), effective thermal conductivities for fluid (K_{eff}) and solid (K_{seff}), heat transfer coefficient between fluid and solid (h_{fs}), and radiation terms need to be specified. These considerations are discussed in Section 3.4.

3.4 Model Parameters

3.4.1 Porosity

From the porosity distribution experiments in Section 2.5.2, it can be concluded that the porosity approaches 1 at the wall, decreases for both small shredded and large shredded scrap towards the center. It is explained in Section 2.5.2 that there is a general trend among researchers to use an exponential decay function for porosity variation from wall to the center of the bed, based on the experimental porosity variation observation of Roblee, 1958 and Benenati and Brosilow, 1962. The typical exponential function can be represented as; $\phi = \phi_{\infty} (1 + ae^{-bx/L_c})$, which is also explained in Section 2.5.2. Our experimental porosity distribution

data are plotted with distance from the wall for both small shredded scrap and large shredded scrap, which are shown in Figures 3.1 and 3.2. It is seen from Figure 3.1 and 3.2 that our experimental porosity distribution data could be fit in the exponential decay function by appropriate values of a , b and L_c . Table 3.2 shows the values of a , b and L_c for regular shaped particles, small shredded and large shredded scrap, respectively.

Our experimental data of porosity variation and modeled exponential decay function of porosity for small shredded scrap and large shredded scrap are shown in Figure 3.3 and 3.4, respectively.

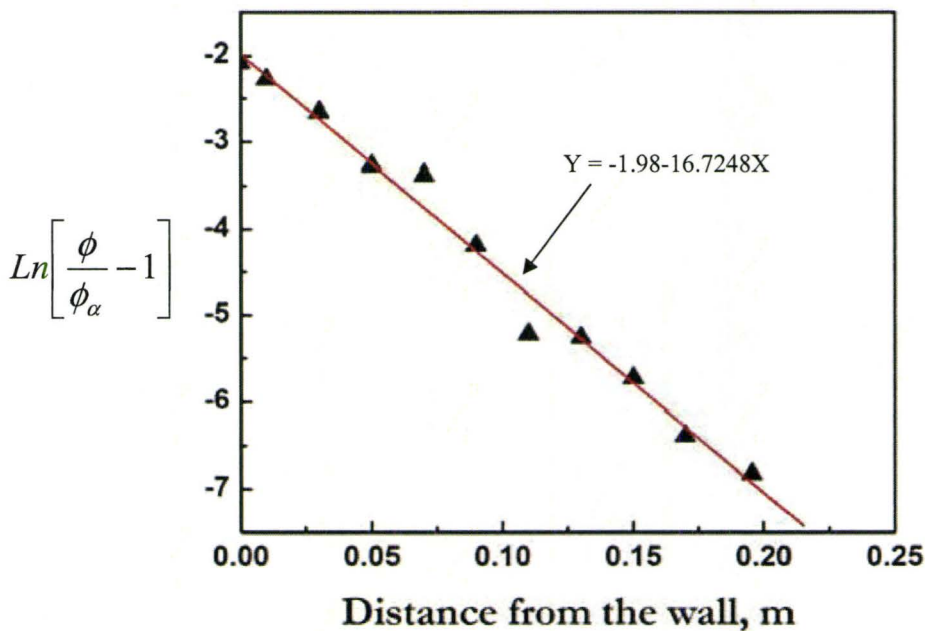


Figure 3.1: Experimental porosity variation from the wall to the center of the furnace for small shredded scrap

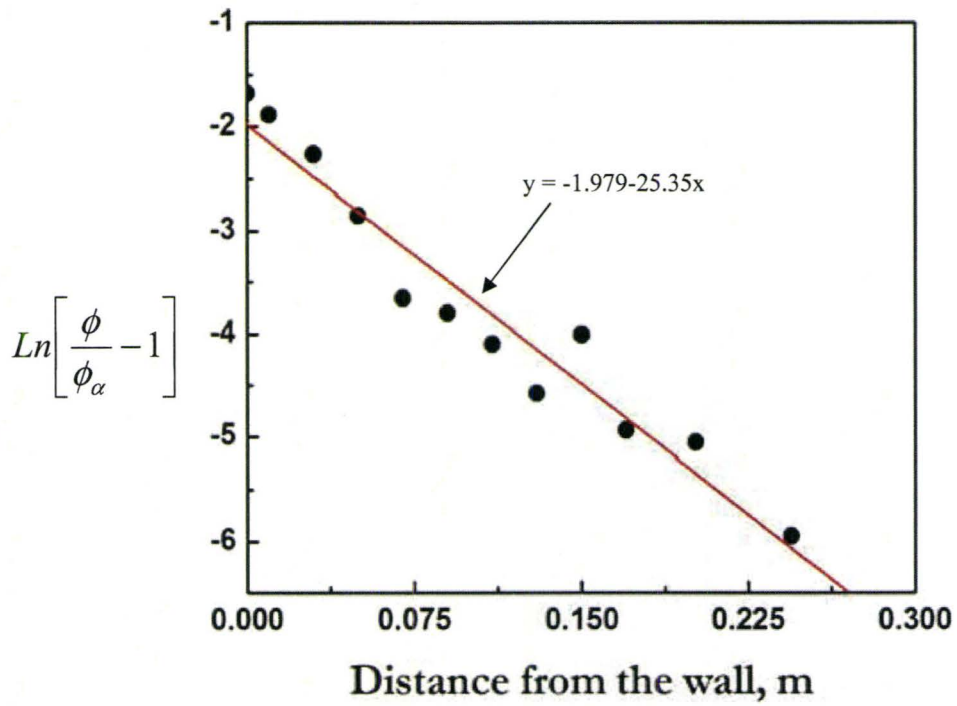


Figure 3.2: Experimental porosity variation from the wall to the center of the furnace for large shredded scrap

Table 3.2: Comparison of a , b and L_c for spherical shaped particles, large shredded scrap and small shredded scrap.

Particles	a	b	$L_c(mm)$	ϕ_α
Spherical (Benenati and Brosilow, 1962)	1.7	6	2-4	0.38
Small shredded scrap	0.1379 ± 0.025	0.4515 ± 0.036	27	0.85
Large shredded scrap	0.1382 ± 0.030	0.7098 ± 0.028	28	0.90

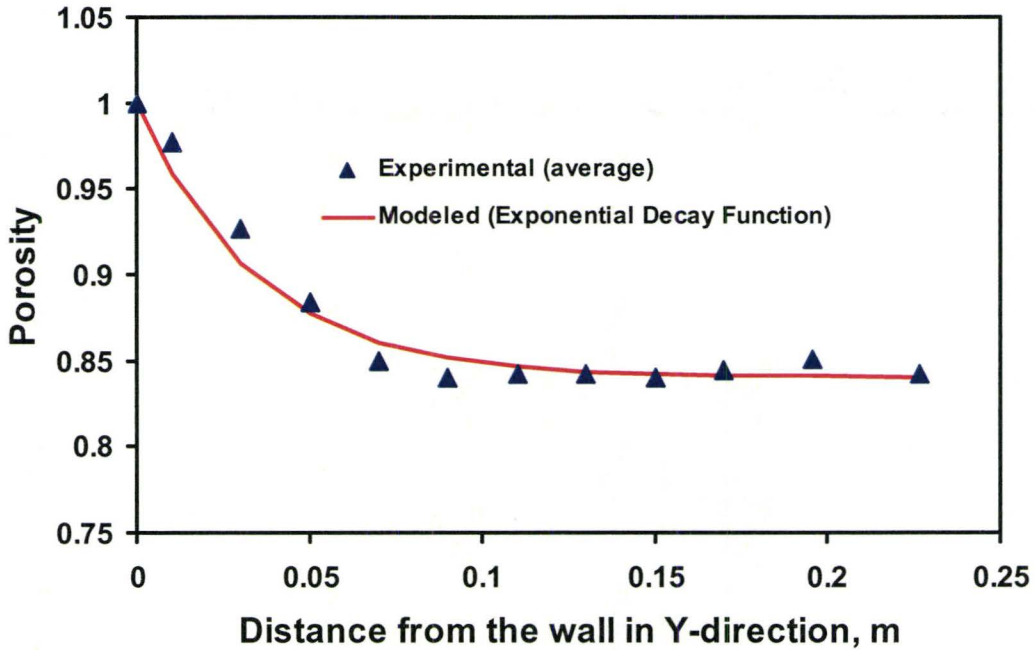


Figure 3.3: Experimental porosity variation from the wall to the center of the furnace for small shredded scrap and exponential decay function of porosity variation from the wall to the center of the furnace

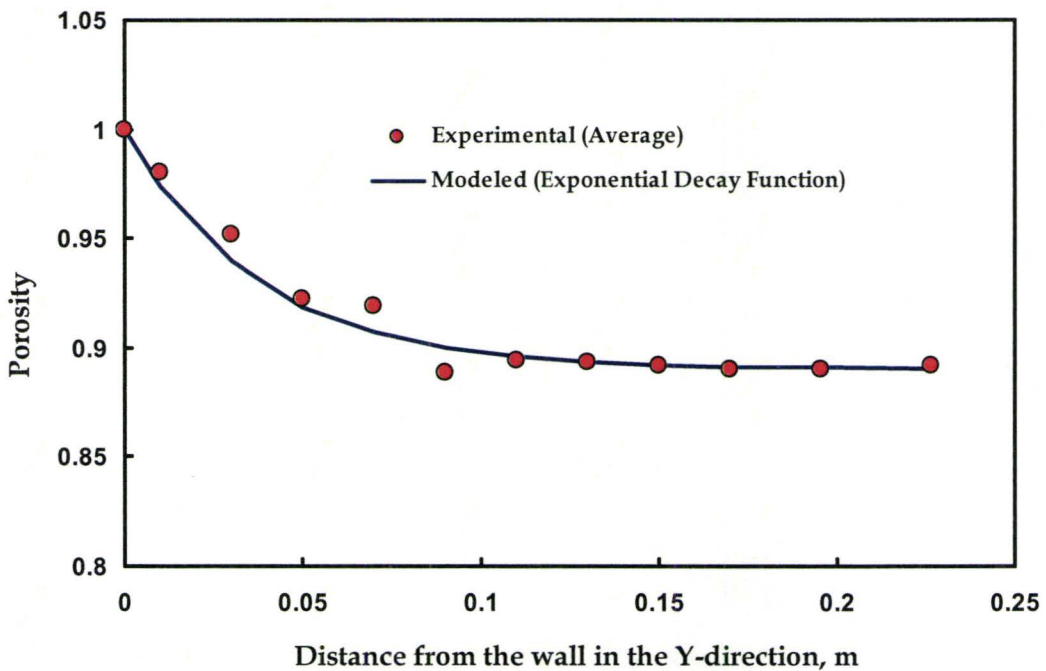


Figure 3.4: Experimental porosity variation from the wall to the center of the furnace for large shredded scrap and exponential decay function of porosity variation from the wall to the center of the furnace

3.4.2 Permeability, K and Drag Coefficient, F

The pressure drop across a porous bed is a function of system geometry, bed porosity, bed permeability, and the physical properties of the fluid phase. Significant progress has been made to establish the correlation between velocity and pressure drop across the porous bed, as recently summarized by Jamialahmadi et al (Jamialahmadi, Muller-Steinhagen and Izadpanah, 2005). Ergun (Ergun, 1952) critically reviewed the fluid flow through porous bed of granular solids. He showed that the pressure drop is caused by simultaneous kinetic and viscous energy losses and the following equation is applicable.

$$\frac{\Delta P}{L} = 150 \frac{(1-\phi)^2}{\phi^3} \frac{\mu U}{d_p^2} + 1.75 \frac{(1-\phi)}{\phi^3} \frac{\mu G U}{d_p} \quad \dots\dots\dots (3.30)$$

The above equation is known as the Ergun equation, where, ΔP , L , ϕ , μ , d_p , U and G are pressure loss, height of porous bed, porosity, viscosity of the fluid, effective diameter of the particles, superficial fluid velocity and mass flux of the fluid i.e., ρU . The Ergun equation can be rewritten as;

$$\frac{\Delta P}{L} = \frac{\mu U}{K} + \frac{F}{\sqrt{K}} \frac{\mu G U}{d_p} \quad \dots\dots\dots (3.31)$$

where, K and F are the permeability of a porous medium and the drag coefficient or geometric factor, which can be written as, $K = \frac{\phi^3 d_p^2}{150(1-\phi)^2}$ and

$F = \frac{1.75}{\sqrt{150}\phi^{3/2}}$. The permeability and drag coefficient depend upon the size

and shape of the solid phase. According to the Ergun equation the permeability, K , was plotted with both porosity and particle diameter using constant particle diameter of 0.05 m and constant porosity of 0.5. Figure 3.5 shows that permeability increases with both porosity and particle diameter. Similarly, the geometric factor, F was plotted with porosity in Figure 3.6. Both the viscous loss term and the inertial loss terms in the momentum equation, vanish when the porosity is one, i.e., single phase flow.

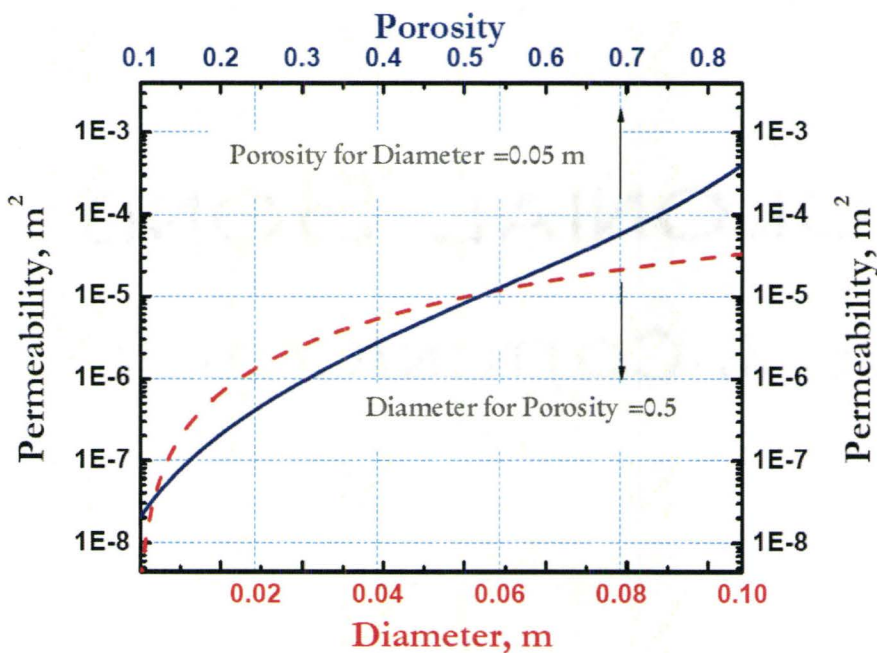


Figure 3.5: Variation of Permeability with Porosity ($d_p=0.05m$) and Particle Characteristic Diameter (Porosity = 0.5) of the particle

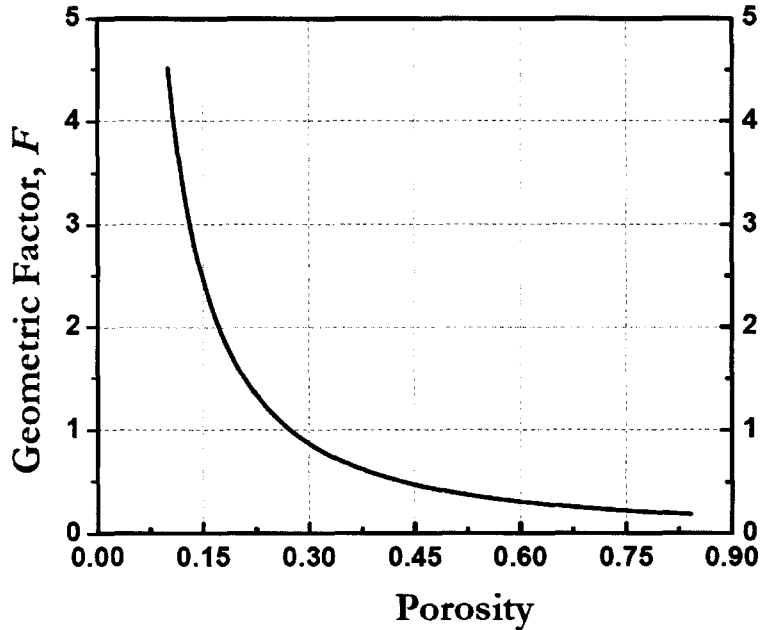


Figure 3.6: Variation of Geometric Factor, F with Porosity

In the present research the scrap particles are irregular shaped and our porous bed is complex compared to packed bed. There have been no studies about the permeability and geometric factor for irregular shaped particles. In the present research permeability equation and geometric factor was taken according to Ergun equation. The permeability equation

then can be presented as; $K = \frac{\phi^3 d_p^2}{150(1-\phi)^2}$. Similarly, the geometric factor

can be presented as; $F = \frac{1.75}{\sqrt{150}\phi^{3/2}}$. In this study effective particle diameter

i.e., d_p , was tuned to fit the experimental temperature distribution and numerical calculation, which is explained in Section 3.9.

3.4.3 Effective Thermal Conductivity

The simplest model for the effective thermal conductivity of porous media is the rule of mixtures, which can be described as, $K_{eff} = \phi K_f + (1-\phi)K_s$, where, ϕ is the porosity of the medium and K_f and K_s are the conductivities of fluid and solid phases, respectively. Many commercial software and LTE models, which are discussed in Section 3.2.3, use this (FLUENT 6.0, Lauriat and Prasad 1987).

Thermal dispersion in porous medium is a complex phenomenon resulting from diffusion in the solid phase and convection and diffusion in the moving fluid. Thermal dispersion is modeled as a small correction to the effective fluid conductivity in the porous medium. On the other hand effective thermal conductivity of the solid is simply modeled as; $K_{seff} = (1-\phi)K_s$, where K_s is the solid conductivity. Different models are presented in Table 3.3 for effective thermal conductivity of the fluid in porous media. Figures 3.7 - 3.9 show the variation of fluid effective thermal conductivity with particle Reynolds number, particle diameter and porosity for the models in Table 3.3. It can be concluded that K_{feff} increases as the particle Reynolds number increases. In the literature K_{feff} data are available in the range of $10 < Re_p < 2500$. In the present scrap-heating situation the Reynolds number ranges from $10 - 10^5$. K_{feff} is sensitive to porosity variation, but it is more sensitive to particle diameter in most models. Similarly, the Peclet

number, which is the product of Reynolds number and Prandtl number, ranges from 1 - 10⁴. Due to high value of the Peclet number thermal dispersion was ignored in this study so the rule of mixture is used. Convection is explicitly handled in the momentum equations, since it is so large it can not be assumed as simple dispersion process.

Table 3.3: Summary of different models for K_{eff}

Authors	K_{eff}	Comments
Demirel et al., 2000	$K_f (2.894 + 0.068 Re_p)$	<u>Model 1</u> Rasching Ring 5.6 < Column Dia / d_p < 6.6
Hunt and Tien, 1988a, 1988b	$\phi K_f + 0.025 \rho C_p U \sqrt{K}$	<u>Model 2</u> High porosity metal foam, Porosity=0.94-0.97 Length=15.24 cm Width=5.08 cm Thickness=1.27 cm
Chen et al., 1996	$\phi K_f + 0.01 \frac{1-\phi}{\phi^2} \rho C_p U d_p$	<u>Model 3</u> Glass Sphere d_p =3mm Gas velocity =0.01 m/s
Hsu and Cheng 1990, David et al. 1991, and Jang and Chen 1992	$\phi K_f + 0.04 \frac{1-\phi}{\phi} \rho C_p U d_p$	<u>Model 4</u> Porosity =0.4 Forced convection of air through annular and cylindrical packed column
Hong and Tien 1987, Amiri et al 1995, and Amiri and Vafai 1998	$\phi K_f + 0.1 \rho C_p U d_p$	<u>Model 5</u> Spherical Particle d_p =2 -8.5 mm Porosity =0.9 Re_p =100

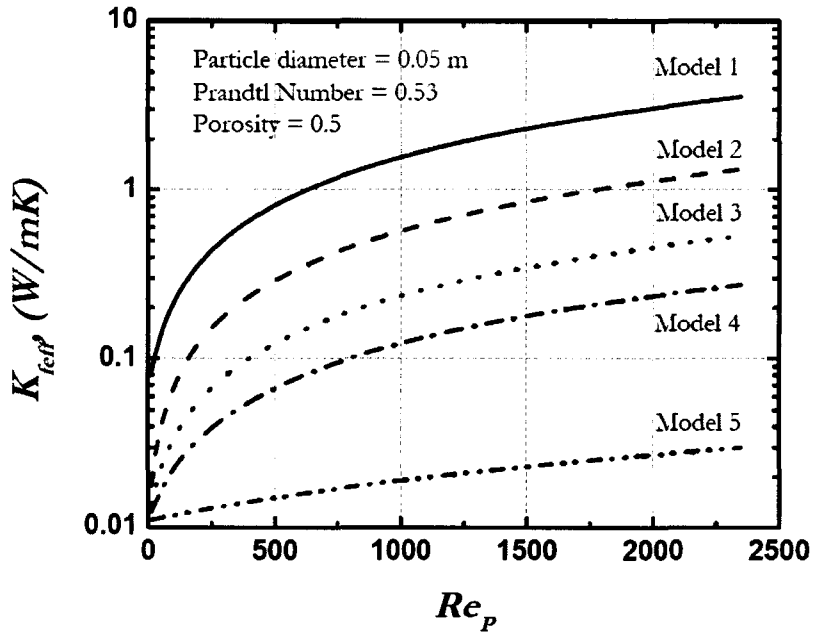


Figure 3.7: Plot of fluid effective thermal conductivity with particle Reynolds number ($K_f=0.022$). The models are shown in Table 3.3

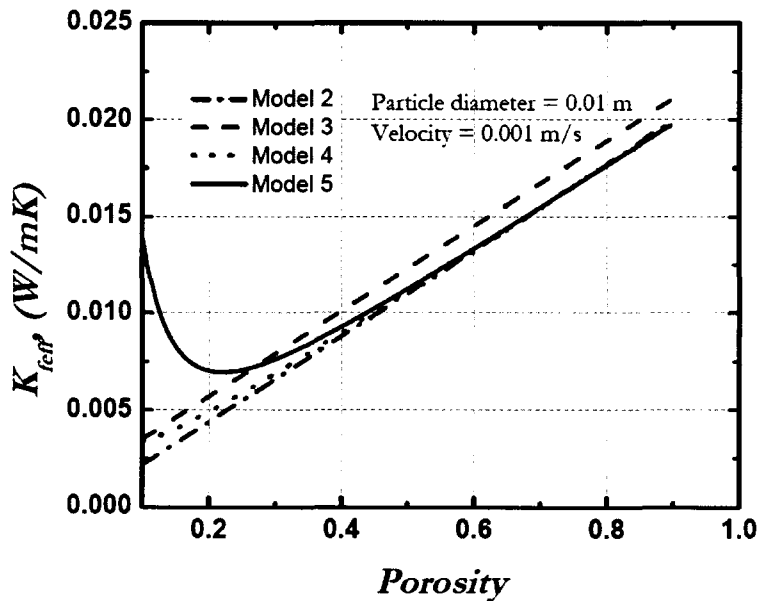


Figure 3.8: Fluid effective thermal conductivity with porosity ($K_f=0.022$). The Models are shown in Table 3.3.

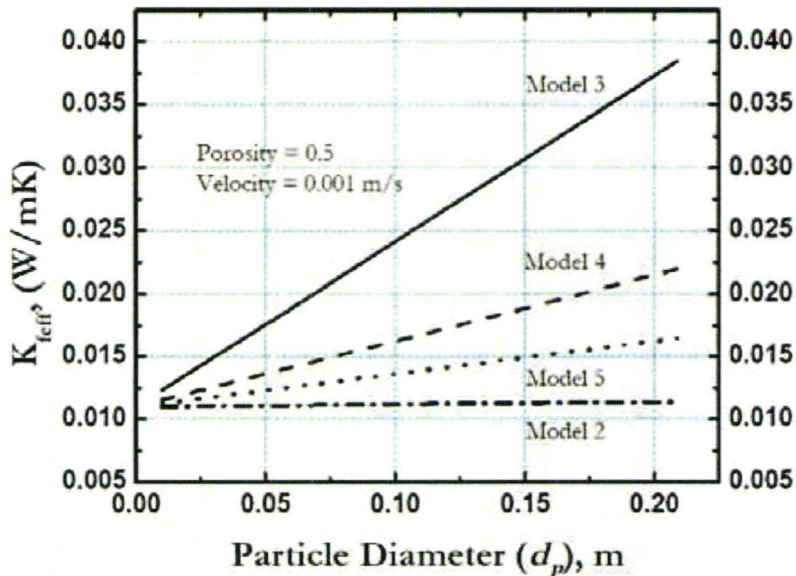


Figure 3.9: Fluid effective thermal conductivity with particle diameter ($K_f=0.022$). The models are shown in Table 3.3.

3.4.4 Fluid to Solid Heat Transfer Coefficient, h_{fs} , and Specific Surface area, A_s

The heat transfer coefficient between the fluid and the solid, h_{fs} , determines the rate of heat transfer from fluid to solid in porous media. For a sufficiently high heat transfer coefficient, h_{fs} , one can assume local thermal equilibrium between fluid and solid, but at low levels a temperature difference between fluid and solid or local thermal non-equilibrium arises. Over the years many researchers determined h_{fs} , either experimentally or using semi empirical correlations. Wakao et al. 1979, performed a comparative study on fluid to particle heat transfer

coefficient, h_{fs} , in packed beds. He summarized the h_{fs} data, which was reported in the literature for both steady and unsteady situations and found the analogy of mass correlation with heat transfer coefficient, which is presented here in Figure 3.10. Wakao considered Nusselt number as the ratio of convective heat transfer to conductive heat transfer ($N_u = \frac{hL}{k_f}$; h , L and k_f are heat transfer coefficient, characteristic length and thermal conductivity of the fluid). He defined the Reynolds number as $\frac{\rho u L}{\mu_f}$.

Where ρ , u and μ_f are density of the fluid, velocity of the fluid and viscosity of the fluid, respectively. A summary of available models for determining fluid to solid heat transfer coefficient, h_{fs} , is presented in Table 3.4.

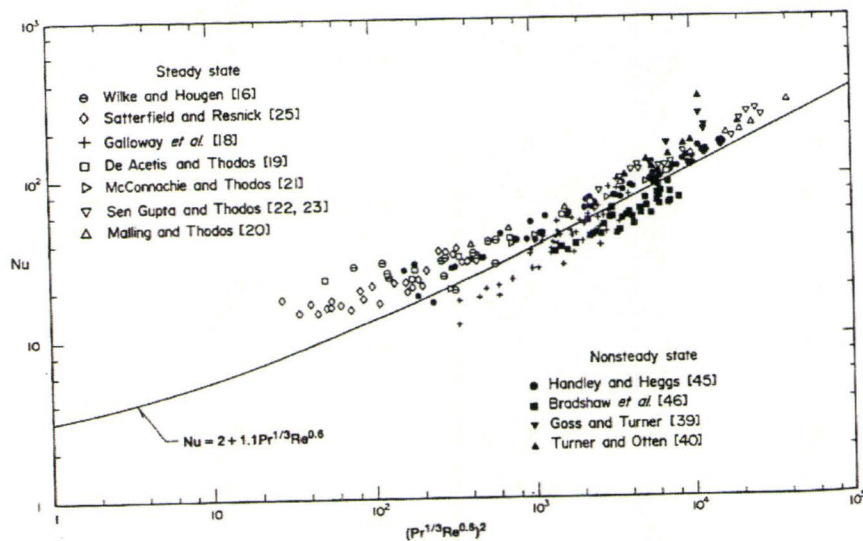


Figure 3.10: Correlation of Nusselt numbers with Re and Pr (Wakao et al. 1979)

Table 3.4: Summary of different models for h_{fs}

Authors	h_{fs}	Comments
Wakao et al, 1979 Amiri and Vafai 1994, Amiri and Vafai 1998, Vafai and Amiri 1998, and Amiri et al 1995.	$K_f \frac{(2+1.1Pr^{1/3} Re^{0.6})}{d_p}$	Model 1 $A_s = \frac{6(1-\phi)}{d_p}$
Hwang et al. 1995.	$0.004 \left(\frac{d_v}{d_p} \right) \left(\frac{K_f}{d_p} \right) Pr^{0.33} Re^{1.35}$ $1.064 \left(\frac{K_f}{d_p} \right) Pr^{0.33} Re^{0.59}$	Model 2 $A_s = \frac{20.346(1-\phi)\phi^2}{d_p},$ $d_v = 4\phi / A_s, Re < 75$ Re > 350
Dixon and Cresswell 1979.	$\left[\frac{d_p \phi}{0.2555 Pr^{1/3} Re^{2/3} K_f} + \frac{d_p}{10K_s} \right]^{-1}$	Model 3 $A_s = \frac{6(1-\phi)}{d_p}$
Furnas 1932	$h_v = h_{fs} A_s = \frac{A^* f(\omega)^{**} V_g^{0.9} T^{0.3}}{d_p^{0.75}}$	Model 4 $T > 1100^\circ C$

*A: Constant depends on bed properties

**f(w): Function of void fraction

For scrap heating using burners the burner temperature is high compared to other areas of the furnace. Most of the experimental data in Figure 3.10 was much lower temperature. The highest temperature (1100° C) was used by Furnas (1932) in his experiments. Kitaev and coworkers, (1968) summarized the results of Furnas study at elevated temperatures. The effects of void volume and temperature are difficult to obtain, so have not yet been firmly established. The volumetric heat transfer coefficient, $h_{fs} A_s$

is presented by them in the form of $h_v = h_{fs} A_S = \frac{Af(\omega)V_g^{0.9}T^{0.3}}{d_p^{0.75}}$, where A , $f(\omega)$, V_g , T and d_p are respectively a coefficient depending on bed properties (~ 80 for lump material), a function of void fraction (~ 0.5), superficial gas velocity (m/s), temperature ($^{\circ}$ C) and particle diameter (mm). Recently, Guo and Irons (2005) used this correlation to model EAF scrap melting phenomena. In the present work when the temperature was higher than 1100°C , then the concept of Kitaev and coworkers was adopted. At low temperature the work of Wakao et al. 1979, was adopted to predict the fluid to solid heat transfer coefficient, h_{fs} . In this research effective particle diameter was tuned to fit the experimental results and numerical results, which is presented in Section 3.9.

3.4.5 Radiation

Radiation is an important mechanism of heat transfer in porous media at high temperature. In most previous studies on heat transfer through porous media convection and conduction were the only modes of heat transfer considered. Recently, a series of studies (Yoshida et al. 1990, Lu et al. 1994, Argento and Bouvard 1996, Talukdar et al. 2004, Yee and Kamiuto 2005 and Seddeek et al. 2007) considered combined convective, conductive and radiative heat transfer mechanisms. Considering local

thermal non-equilibrium (LTNE) models for porous media, the energy equation of the solid phase is (Mohamed and Amiri, 2002);

$$(1 - \phi)(\rho C)_s \frac{\partial T_s}{\partial t} = K_{seff} \nabla^2 T_s - \nabla \cdot q' + h_{fs} A_s (T_f - T_s) \quad \dots\dots\dots (3.32)$$

In the above equation ϵ , T , ρ , C , K_{seff} , q' , h_{fs} , A_s are porosity of the medium, temperature, density, specific heat, effective thermal conductivity, radiation flux, heat transfer coefficient and specific surface area respectively. Chen and Churchill 1963, and in recent years Raptis 1998 and Seddeek et al. 2007, have shown that for an optically thick medium i.e., all incident radiation travels only short distance before interacting with the medium, the radiative heat transfer can be treated as a diffusive process, so the energy equation of the solid phase in the porous medium can be rewritten as;

$$(1 - \phi)(\rho C)_s \frac{\partial T_s}{\partial t} = (K_{seff} + K_r) \nabla^2 T_s + h_{fs} A_s (T_f - T_s) \quad \dots\dots\dots (3.33)$$

Where, K_r presents the radiative conductivity of the medium. Determining the radiative conductivity has been the subject of several studies. The models, may be classified into four groups. The first type is based on idealized geometrical arrangements of the phases, which allows direct algebraic formulation of the heat transfer process. Argo and Smith 1953, considered a regular array of spheres, which was separated by the particle diameter, d_p . Assuming one particle diameter, which is the distance between two layers of solid particles, they suggested the following

expression for the radiative conductivity; $K_r = \frac{4\sigma d_p E T_m^3}{(2-E)}$. Where σ , d_p , E

and T_m are Stefan Boltzmann constant, particle diameter, emissivity, and mean temperature of the medium, respectively. Here temperature differences within the medium were sufficiently small. The second type model is the Rosseland model (Rosseland 1936) where radiant transfer was considered as diffusion of photons and radiative conductivity has the

following expression; $K_r = \frac{4\sigma l T_m^3}{3}$, where l is the mean free path for

radiation and other symbols are already explained in the first type of model. For a packed bed the mean free path for radiation can be taken as a particle diameter. The third type of model is based on a pseudohomogeneous material. The following expression of radiative

conductivity can be written as; $K_r = \frac{16\sigma n^2 T_m^3}{3(x_a + x_b)}$. Where n , x_a and x_b are

index of refraction of solid relative to fluid, absorption cross section per unit volume of packing and scattering cross section per unit volume of packing, respectively. The fourth type of model was proposed by Argento and Bouvard 1996. They proposed a ray tracing method to evaluate the radiative properties of porous media, which is in good agreement with reported data elsewhere (Yong et al. 1983, Vortmeyer 1978). They adopted Chen and Churchill's 1963, radiative conductivity model, where radiative

conductivity, $K_r = \frac{8\sigma T_m^3}{(a + 2s)}$. a and s are absorption coefficient and scattering coefficient, respectively. So the radiative thermal conductivity of the medium can be calculated using absorption and scattering coefficients. To this end Argento and Bouvard introduced a dimensionless radiative exchange factor by $E_r = 1/R(a+2s)$, where R is the radius of the particle. Finally, the radiative conductivity can be written as; $K_r = 8E_r R \sigma T_m^3$. They determined radiative exchange factor over the range of 0.20-0.85 of void fraction. Also they determined both absorption and scattering coefficient over the range of 0.56-0.80 of void fraction. The Argento and Bouvard study was based on equal sized sphere but their method was used for analysis of radiative conductivity for cylindrical rods by Vafai and Etefagh (1988).

In the present research a simple radiative net heat flux model was considered, which can be written as; $q^r = AF_{12}\epsilon\sigma(T_1^4 - T_2^4)$, where A , F_{12} , ϵ , σ , T_1 and T_2 are area, view factor, emissivity, Stefan Boltzman constant, temperature at point 1 and temperature at point 2. In this research view factor was taken as 1. Emissivity was taken as 0.56, which is the emissivity of iron oxide. A sensitivity analysis is shown in Section 3.11 with respect to burner efficiency and radiation.

3.5 Numerical Solution Procedure

A control volume based finite difference procedure (Patankar, 1980) has been adopted in the present study to solve the governing equations numerically. The solution is initiated by discretizing the domain in a large number of non-overlapping control volumes. The governing equations are integrated over all such control volumes to yield a system of algebraic equations, called the discretization equation. The governing equations of flow, turbulence and energy have both first and second order derivatives. These terms are numerically integrated using the concept as applied to a combined convection diffusion problem incorporating the hybrid differencing scheme proposed by Patankar (1980). The pressure velocity inter-linkage in flow equation is solved by an implicit difference procedure referred to as SIMPLE, Semi-Implicit Method for Pressure Linked Equations, (Patankar, 1980). A typical discretization equation for a quantity ϕ is as follows;

$$A_P \phi_P = A_E \phi_E + A_W \phi_W + A_N \phi_N + A_S \phi_S + A_T \phi_T + A_B \phi_B + A_p^0 \phi_p^0 - S_C \cdot Vol$$

.....(3.34)

in which, A_P , is the center point coefficient while, A_E , A_W , A_N , A_S , A_T and A_B , are the neighbor point (three dimensional) coefficients, representing the combined effect of convection and diffusion. $A_p^0 \phi_p^0$ arises due to unsteady consideration and it is zero for steady state problem. Further, S_C ,

represents the constant component of the linearized source term (viz., $S=S_C + S_P\phi_P$) while the slope will be absorbed in the expression of center point coefficient. The center point coefficient A_P is represented as;

$$A_P = A_E + A_W + A_N + A_S + A_T + A_B + A_p^0 - S_P.Vol \dots\dots\dots(3.35)$$

Thus, in a system of n internal control volumes, n number of similar algebraic equations (viz. eq. $A_p T_p$) can be obtained.

The resultant set of discretization equations for both boundary and internal nodes were solved using the Tri-Diagonal Matrix Algorithm (TDMA) adopting a line-by-line solution procedure, which is presented in Appendix B. In this research 99900 (50X54X37) numbers of control volumes and 2 seconds time step were chosen. Grid independency test was also performed and further increase in control volume or decrease in time steps did not change the numerical results.

The local thermal non equilibrium model for porous media require solution of separate energy equations for both fluid and solid phases. These two equations are coupled with the interface heat transfer coefficient, h_{fs} (Al-Amiri A. M., 2002, 2002). Various studies (Amiri and Vafai, 1994, Alazmi and Vafai 2004) solve the energy equations in a

decoupled manner, handling one temperature at a time. The convergence behavior of the decoupled procedure deteriorates as value of interfacial heat transfer coefficient increases. A robust technique for solving the equations that are coupled with the exchange coefficient is the partial elimination algorithm (PEA), which was proposed by Spalding (1980). In the present research PEA was used to solve the energy equations, which is described in Appendix C.

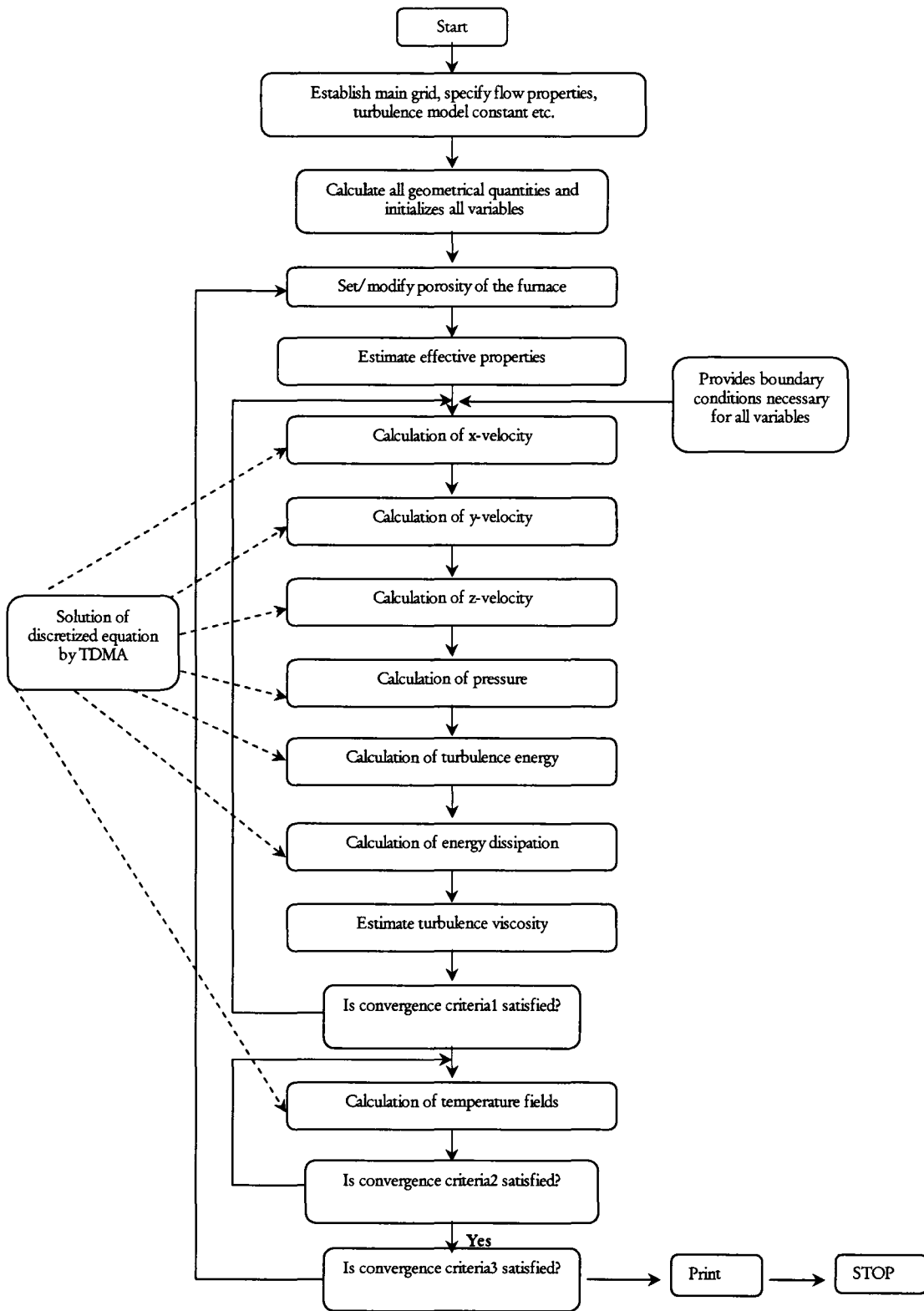
3.6 The Computer Program

The sequential steps of the computer program are discussed below along with the flow diagram shown as Figure 3.11.

1. The information of the grid, dimensions of the furnace, the fluid properties, turbulence model constant, the control parameters such as convergence criteria and the maximum number of iterations are set.
2. Calculation of all geometrical quantities ($A_P, A_E, \dots \phi_P, \phi_E \dots etc.$) and initialization of all variables.
3. Estimation of effective properties.
4. The x-momentum, y-momentum and z-momentum equations are solved sequentially by solving the discretized equation for each of

the control volume. This is followed by solving the turbulence model equation and the values of turbulence kinetic energy and energy dissipation updated in the domain.

5. The fluid and solid properties calculated and updated for the calculation domain.
6. Step 4 and 5 are repeated until convergence criteria for flow, turbulence and the continuity equations are achieved.
7. After the velocity field converged the temperature distribution calculated and updated the porosity. Porosity was updated to 1 for a point if the temperature at that point is more than the steel melting temperature i.e., melting was consider using porosity modification. Step 3 to 7 repeated until the program termination criterion.



3.11: The sequential steps of the computer program

3.7 Evaluation of Computational Procedure

The adequacy and appropriateness of the model were first assessed by carrying out some benchmark simulations. This evaluation procedure of the present computer code was done using the following steps;

- Computations of laminar, steady flow in a cubic cavity with one face moving. This evaluation procedure was adopted from the work of Robert and Mazumdar (2001).
- Computation of laminar, unsteady flow in a cubic cavity with one face moving. It is similar to the work of Robert and Mazumdar, (2001).
- Computation of turbulent, steady flow in a cubic cavity with one face moving.
- Computation of laminar, steady, porous media flow in a cubic cavity with one face moving.
- Computation of laminar, steady natural convection.

Detail assessments are presented in Appendix D. Results of benchmark problems essentially indicated that the unsteady state, three-dimensional, turbulent flow and temperature calculation procedure developed in the present study is initially consistent and sufficiently robust.

3.8 Boundary Conditions

The boundary conditions applied to the numerical solution of the set of governing equations for fluid flow, turbulence and heat transfer in the heating furnace are represented below.

3.8.1 Fluid Flow and Turbulence

Values of all the velocity components and turbulent kinetic energy were taken as zero at the walls, which are represented mathematically as:

$$(0 \leq X \leq L_x, Y=0, 0 \leq Z \leq L_z), (0 \leq X \leq L_x, Y=L_y, 0 \leq Z \leq L_z), (0 \leq Y \leq L_y, X=0, 0 \leq Z \leq L_z), (0 \leq Y \leq L_y, X=L_x, 0 \leq Z \leq L_z), (0 \leq X \leq L_x, Z=0, 0 \leq Y \leq L_y) \text{ and } (0 \leq X \leq L_x, Z=L_z, 0 \leq Y \leq L_y), u = v = w = k = 0;$$

L_x , L_y and L_z are the dimensions of the heating furnace, i.e., computational domain, in X, Y and Z directions. At the outlet gradients of X velocity component, Y velocity component, Z velocity component, turbulent kinetic energy and dissipation rate of turbulent kinetic energy were taken

zero, which are represented as; $\frac{\partial u}{\partial y} = \frac{\partial v}{\partial y} = \frac{\partial w}{\partial y} = \frac{\partial k}{\partial y} = \frac{\partial \epsilon}{\partial y} = 0$. At the inlet X

component velocities were taken as 0.96 m/s, 1.47 m/s and 1.89 m/s for the power of 8.3 kW, 12.8 kW and 17.3 kW, respectively. If burner inlet diameter is considered then the gas velocity is in the order of 60 -116 m/s.

But, at the inlet gas is coming in through a larger cross sectional area than the 4 mm burner inlet. Therefore, these velocities are of the order of 1 m/s.

3.8.2 Temperatures

Temperature gradients in the bottom wall were taken as zero because it was well insulated. All other walls were treated according to convective source terms, which are presented mathematically as:

$$\text{When, } (0 \leq X \leq L_x, Y=0, 0 \leq Z \leq L_z), \frac{\partial T_f}{\partial y} = \frac{\partial T_s}{\partial y} = 0 \text{ and}$$

$$(0 \leq X \leq L_x, Y=L_y, 0 \leq Z \leq L_z), (0 \leq Y \leq L_y, X=0, 0 \leq Z \leq L_z), (0 \leq Y \leq L_y, X=L_x, 0 \leq Z \leq L_z), (0 \leq X \leq L_x, Z=0, 0 \leq Y \leq L_y) \text{ and } (0 \leq X \leq L_x, Z=L_z, 0 \leq Y \leq L_y),$$

$$S_f = h_{fs} A_s (T_s - T_f) + h A_{in} (T_s - T_f) \text{ and } S_s = h_{fs} A_s (T_f - T_s) + h_{out} A_{out} (T_w - T_\alpha)$$

$$\text{At the outlet temperature gradients were taken zero i.e., } \frac{\partial T_f}{\partial y} = \frac{\partial T_s}{\partial y} = 0$$

At the inlet, S_f = Calculated source term from combustion experiments. In front of the burner the source term was distributed in 18 cells to match the thermocouple temperature at position 2, shown in Figure 3.12. In the above, S_f , S_s , h , A_{in} , h_{out} , A_{out} and T_α are source term for fluid phase, source term for solid phase, heat transfer coefficient between fluid and solid of the heating furnace, area of control volume face, heat transfer coefficient between solid wall and environment, which is 1.0 W/m²K (Hassan and Mohamed, 1970), area of control volume face and room temperature. All other symbols are defined earlier. Furnace walls were made of steel and no resistance of the walls were assumed.

Close to the rigid boundaries i.e., the walls, where the variations of the flow properties are steep, the velocities have been consequently modeled using the usual wall function procedure (Launder and Spalding 1974 and Rodi 1980).

3.9 Tuning and Validation of Numerical Model

The key parameters in the present numerical model are permeability, geometric factor, effective thermal conductivity of fluid, effective thermal conductivity of solid and heat transfer coefficient between fluid and solid. The permeability and geometric factor mainly controls fluid flow and effective thermal conductivity of fluid and solid and the heat transfer coefficient mainly responsible for efficiency of the burner. It is important to mention here that the correlations selected for key parameters are dependent on a characteristic particle diameter and porosity, which is shown in Table 3.5. In this research, measured porosity variation inside the furnace was used and the characteristic particle diameter was tuned to obtain good agreement between experimentally measured temperatures and computed temperatures. The simulation condition and considered parameters are summarized in Table 3.5. A sensitivity analysis of burner efficiency on porosity and characteristic particle diameter is also presented in Section 3.11.

It was mentioned earlier in Section 2.4, that there were only 13 temperature measurements in the vertical center plane of the furnace, so the temperature distribution in the furnace was obtained by interpolating and extrapolating the temperatures with a software package, TECPLOT (Tecplot 9.0).

Table 3.5: Experimental Conditions and Tuned Parameters

Parameters	Values/Comments
Scrap	Small Shredded Scrap, Large Shredded Scrap and Busheling
Burner Power	8.3 kW
Furnace Lid Condition	Lid On
Porosity, $\phi = \phi_{\infty} (1 + ae^{-bx/L_c})$	Small Shredded: $a=0.137$ $b=0.45$, $\phi_{\infty}=0.85$ Large Shredded: $a=0.138$ $b=0.71$, $\phi_{\infty}=0.90$ Busheling: Average porosity
Permeability, K	$K = \frac{\phi^3 d_p^2}{150(1-\phi)^2}$
Geometric Factor, F	$F = \frac{1.75}{\sqrt{150}\phi^{3/2}}$
Effective thermal conductivity of solid, K_{seff} and fluid, K_{feff}	$K_{seff} = (1-\phi)K_s + K_r$ $K_{feff} = \phi K_f$
Fluid to solid heat transfer coefficient, h_{fs} and volumetric heat transfer coefficient, h_v	$h_{fs} = K_f \frac{(2 + 1.1Pr^{1/3} Re^{0.6})}{d_p} \text{ at } T < 1100^{\circ}C$ $h_v = h_{fs} A_s = \frac{Af(\omega)V_g^{0.9}T^{0.3}}{d_p^{0.75}}$ $A=160.0, f(\omega) = 0.5 \text{ at } T > 1100^{\circ}C$
Fitted Characteristic Diameter of the Particle, d_p	$d_p=0.027$ m (Small Shredded Scrap) $d_p=0.0285$ m (Large Shredded Scrap) $d_p=0.026$ m (Busheling)

Numerically simulated gas temperatures and experimentally measured thermocouple temperatures, in the vertical center plane, shown in Figure 3.12, are shown in Figure 3.13 and Figure 3.14, for after 30 minutes, and 60 minutes of the heating experiment of small shredded scrap with 8.3 kW burner power. It is clear from Figure 3.13 and Figure 3.14, that there is a good agreement between the numerically predicted temperatures and experimentally measured thermocouple temperatures. Although, temperature patterns are similar, numerically predicted gas temperatures are always higher than those of measured thermocouple temperatures.

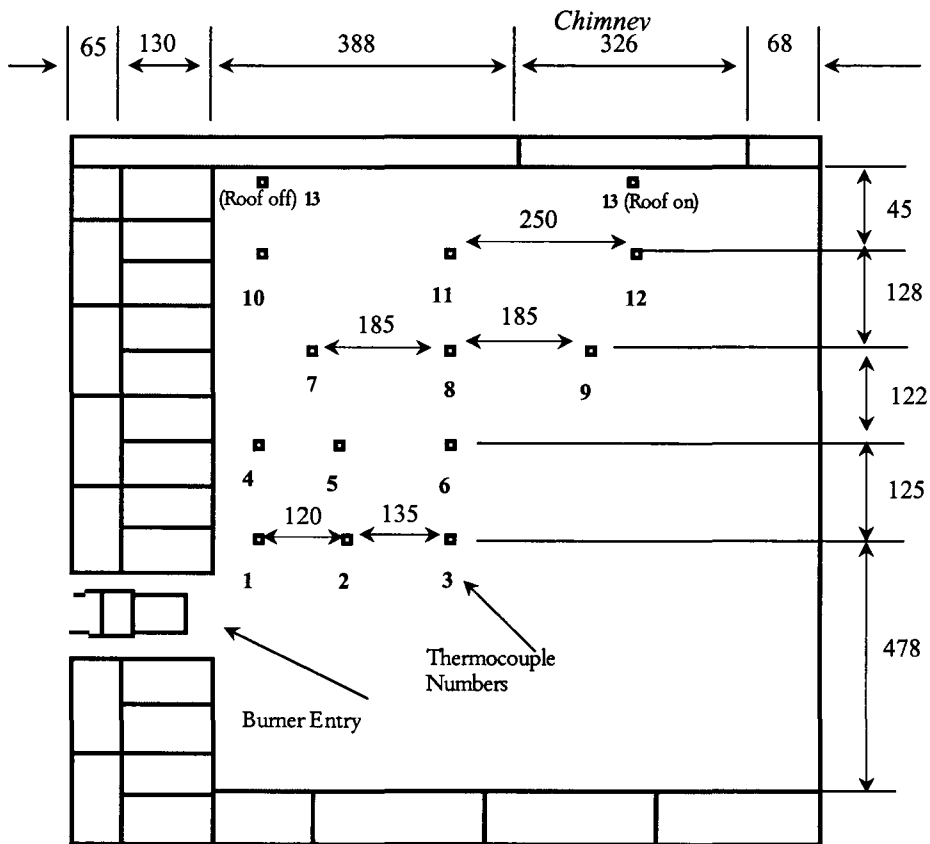


Figure 3.12: Cross section in X-X direction (mm)

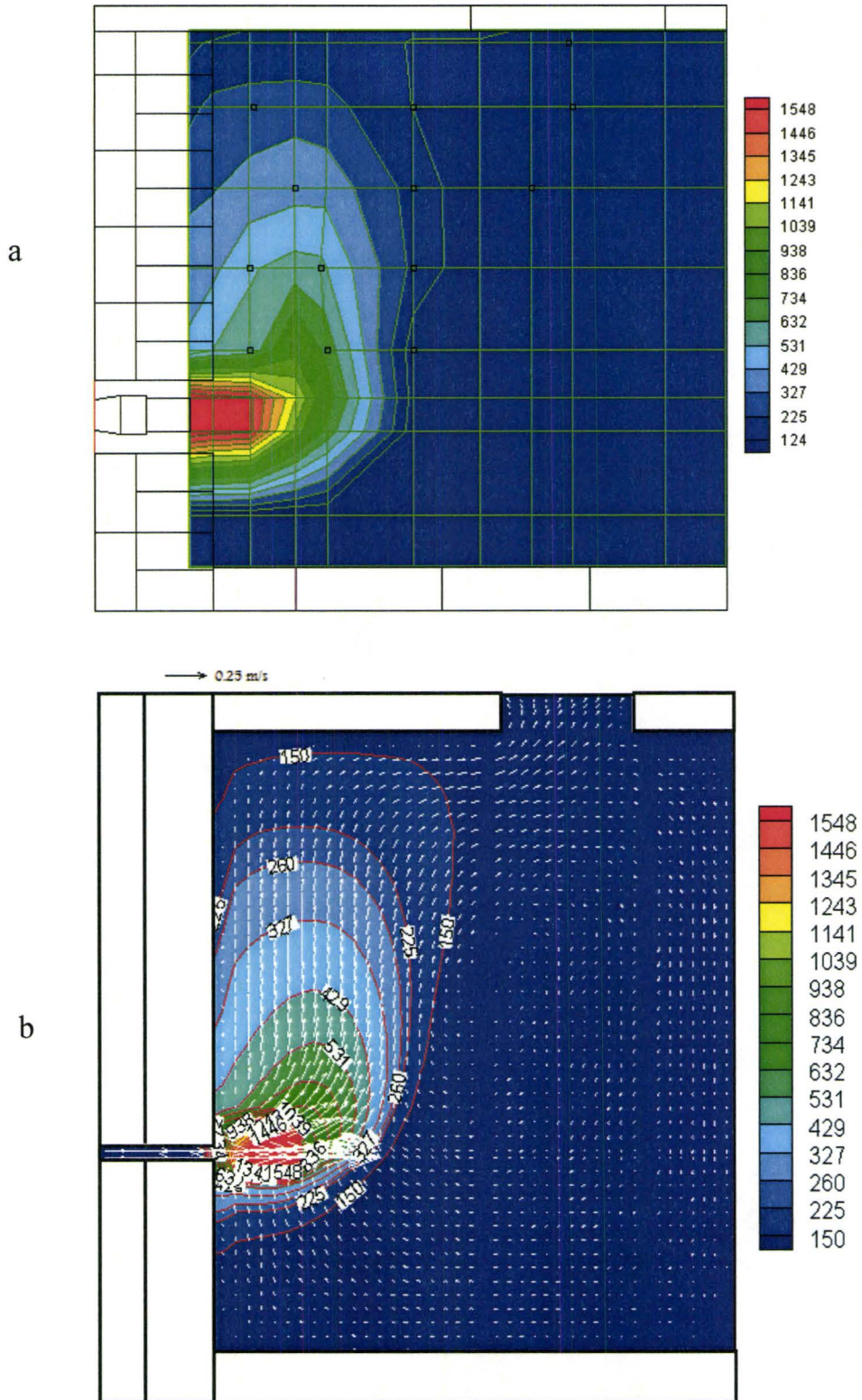


Figure 3.13: Temperature ($^{\circ}\text{C}$) contour of the furnace after 30 minutes of the experiment with Shredded Small Scrap, Power=8.3 kW, Furnace lid on, a=Measured thermocouple temperatures, b=Modeled thermocouple temperatures

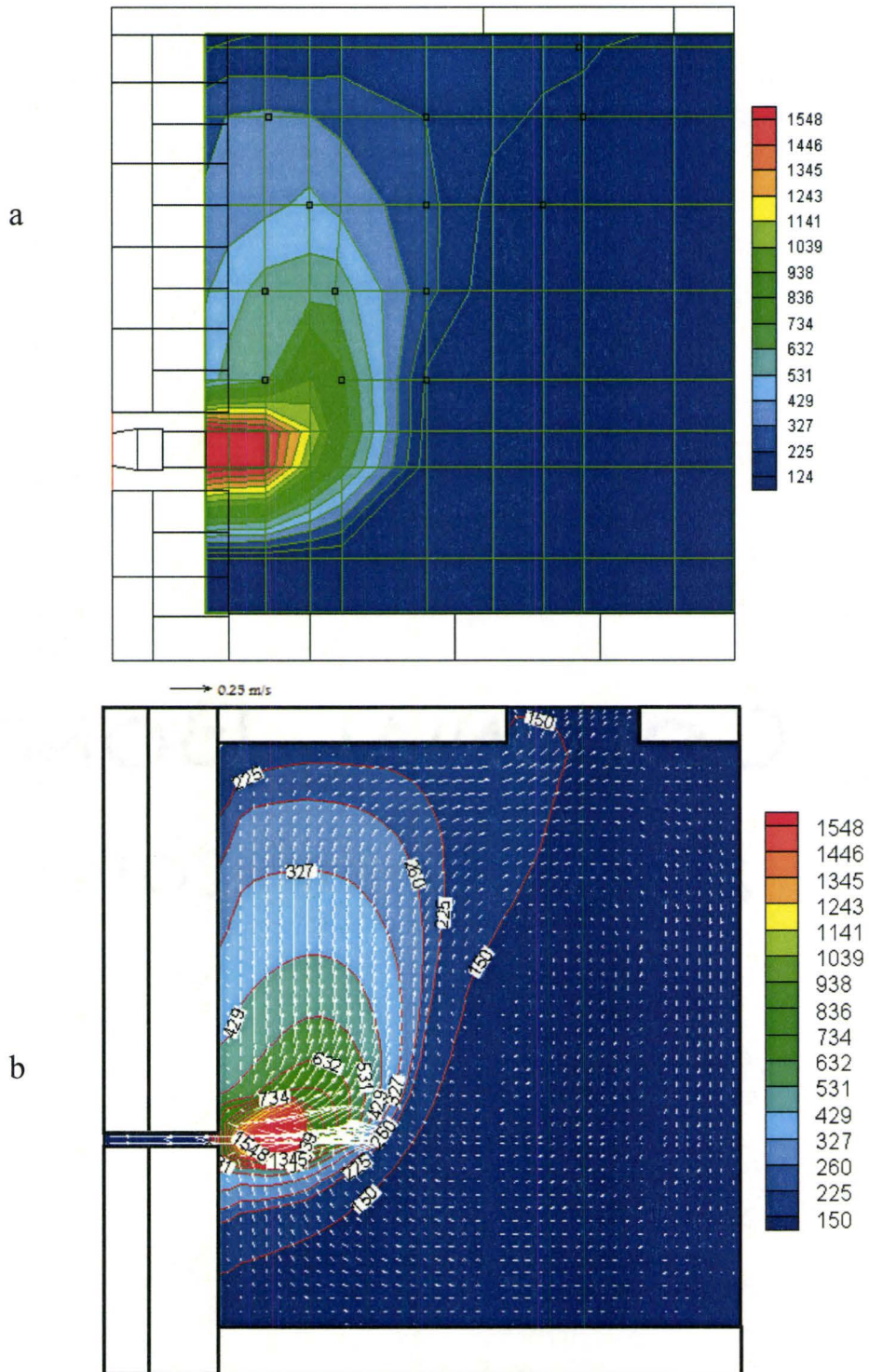


Figure 3.14: Temperature ($^{\circ}\text{C}$) contour of the furnace after 60 minutes of the experiment with Shredded Small Scrap, Power=8.3 kW, Furnace lid on, a=Measured thermocouple temperatures, b=Modeled thermocouple temperatures

The measured temperatures of the thermocouples were lower than that of the predicted gas because the thermocouples receive heat from the gas and radiate heat to the scrap. Therefore, the response of the thermocouples needs to be modeled. During heating thermocouple temperature is changing slowly hence steady state thermocouple temperature can be assumed. For steady state condition an energy balance can be written where the radiant heat flow from the thermocouple to the scrap equals the convective heat flow from the gas to the thermocouple. Assuming the thermocouple as a gray surface it can be written that; $hA(T_f - T_{th}) = AF_{12}\epsilon\sigma(T_{th}^4 - T_{sc}^4)$, where, h , A , T_f , T_{th} , T_{sc} , F_{12} , ϵ and σ are the heat transfer coefficient from gas to scrap, area of the thermocouple, fluid temperature, thermocouple temperature, scrap temperature, shape factor, emissivity and Stefan-Boltzman constant. Value of emissivity was considered as the value of iron oxide i.e., 0.56 (<http://snap.fnal.gov/>) and the value of F_{12} was considered as 1. A plot of predicted gas temperatures, predicted scrap temperatures, measured thermocouple temperatures and predicted thermocouple temperatures are shown in Figure 3.15 to Figure 3.18, for points 1, 2, 12 and 14 (Outlet), from Figure 3.12. It can be seen from Figure 3.15 to Figure 3.18 that there is good agreement between predicted and measured thermocouple temperatures. The dimensionless

temperature difference ($\theta = \frac{T_{th-measured} - T_{th-predicted}}{T_{max-measured} - T_{room}}$) is plotted against total

number of data points, over the heating of 3600 s, in Figure 3.19, which shows the summary of deviation between predicted thermocouple temperatures and measured thermocouple temperatures of small shredded scrap with 8.3 kW burner power. Standard deviation of the absolute dimensionless temperature difference is 0.0266. Similarly, the dimensionless temperature difference is plotted against total number of data points in Figure 3.20 and Figure 3.21 for large shredded scrap and busheling with burner power 8.3 kW. The standard deviation of the absolute dimensionless temperature difference for large shredded scrap and busheling are 0.0336 and 0.0443, respectively. The overall dimensionless temperature difference for small shredded scrap, large shredded scrap and busheling is shown in Figure 3.22.

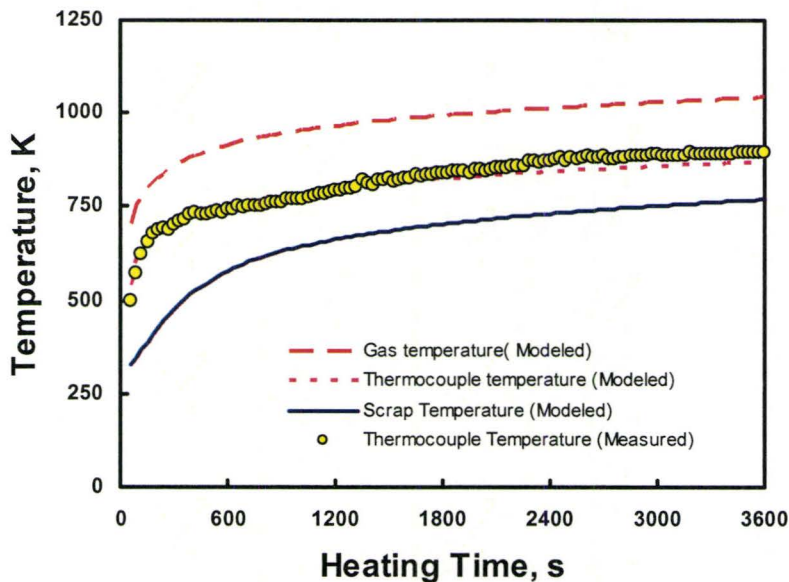


Figure 3.15: Numerically predicted gas and scrap temperatures, predicted thermocouple temperatures and measured thermocouple temperatures with time of heating for point 1 (Shown in Figure 3.12, Small shredded scrap, Burner power=8.3kW).

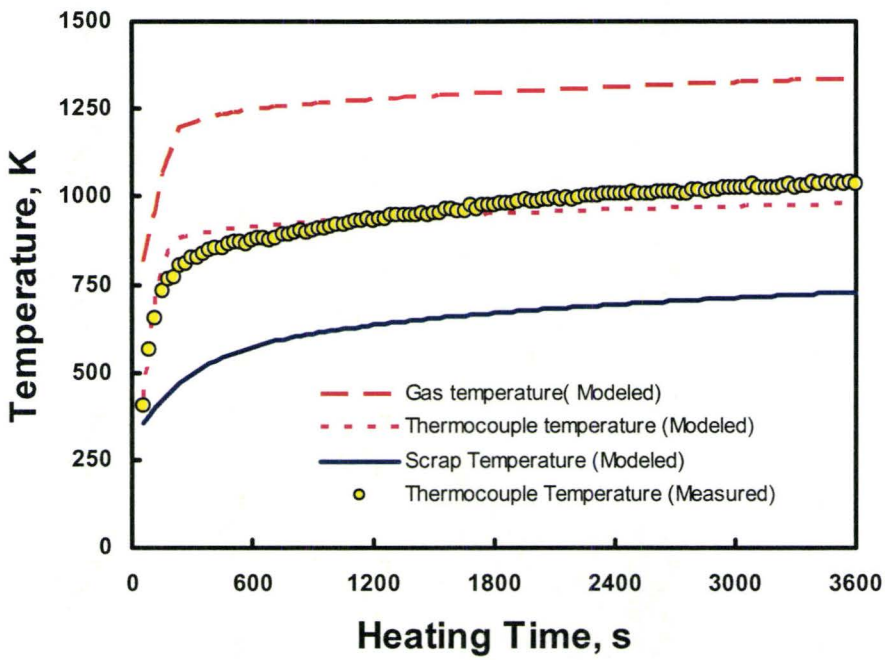


Figure 3.16: Numerically predicted gas and scrap temperatures, predicted thermocouple temperatures and measured thermocouple temperatures with time of heating for point 2 (Shown in Figure 3.12, Small shredded scrap, Burner Power=8.3 kW).

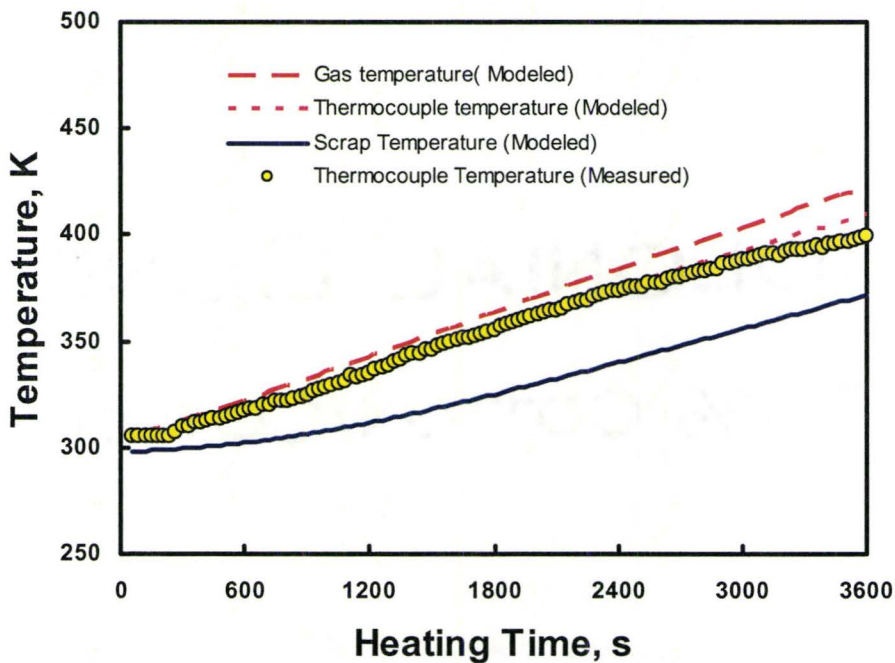


Figure 3.17: Numerically predicted gas and scrap temperatures, predicted thermocouple temperatures and measured thermocouple temperatures with time of heating for point 12 (Shown in Figure 3.12, Small shredded scrap, Burner power = 8.3 kW).

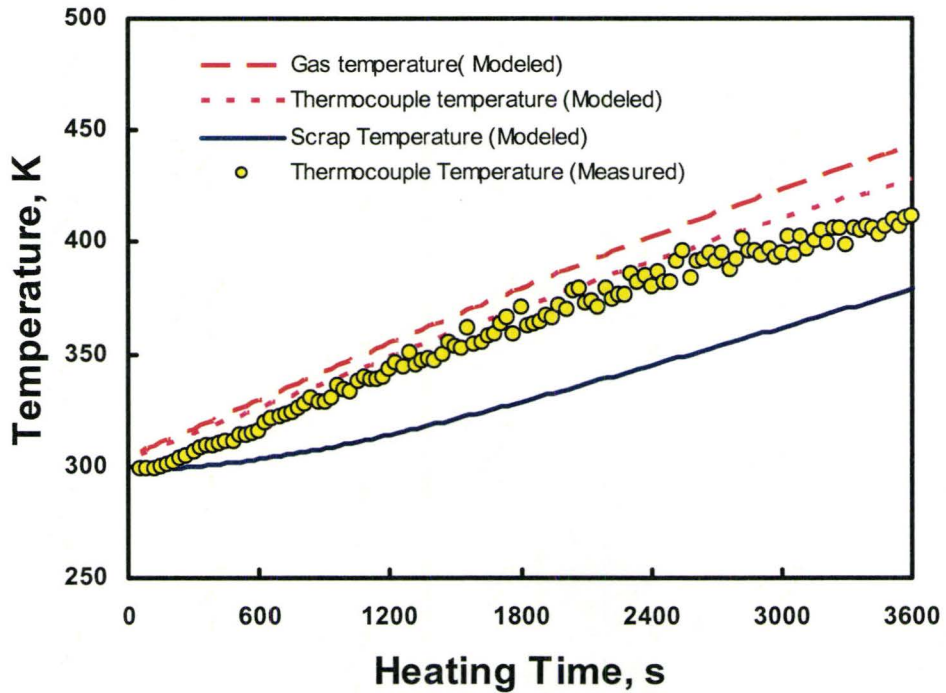


Figure 3.18: Numerically predicted gas and scrap temperatures, predicted thermocouple temperatures and measured thermocouple temperatures with time of heating for point 14 (Shown in Figure 3.12, Small shredded scrap, Burner power = 8.3 kW).

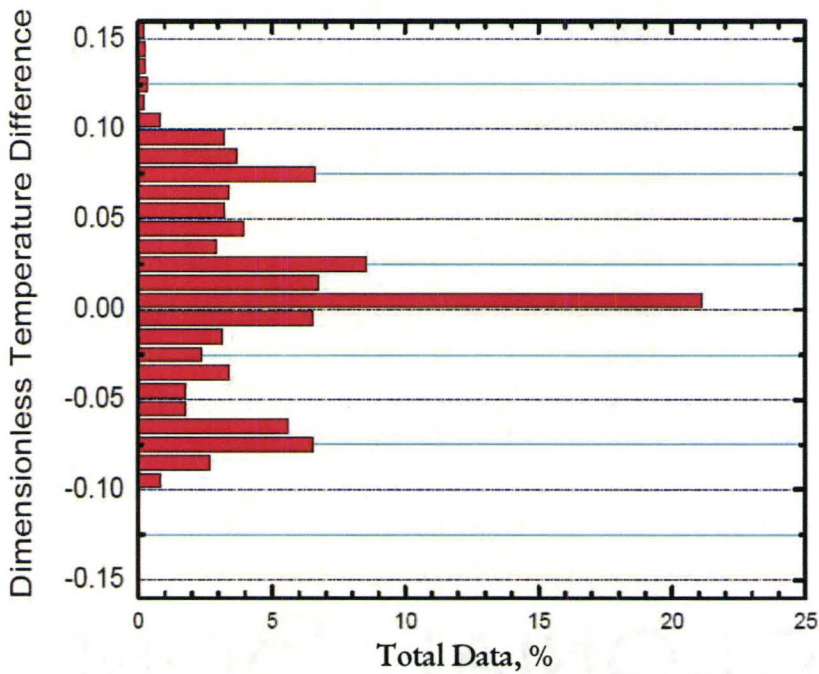


Figure 3.19: Summary of deviation between predicted thermocouple temperatures and measured thermocouple temperatures for all points, shown in Figure 3.12 (Small shredded scrap, Burner power=8.3kW).

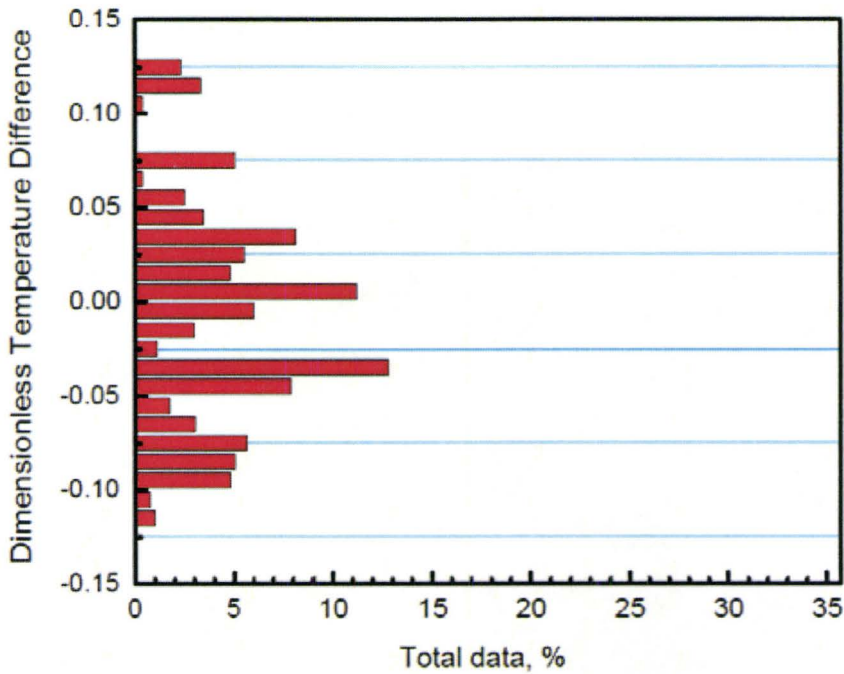


Figure 3.20: Summary of deviation between predicted thermocouple temperatures and measured thermocouple temperatures for all points, shown in Figure 3.12 (Large shredded scrap, Burner power=8.3kW).

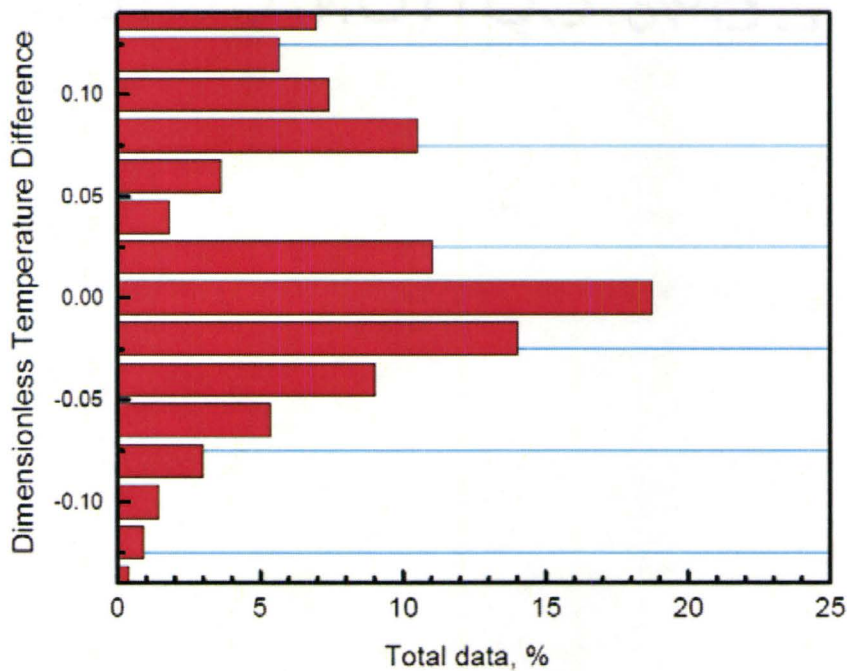


Figure 3.21: Summary of deviation between predicted thermocouple temperatures and measured thermocouple temperatures for all points, shown in Figure 3.12 (Busheling, Burner power=8.3kW).

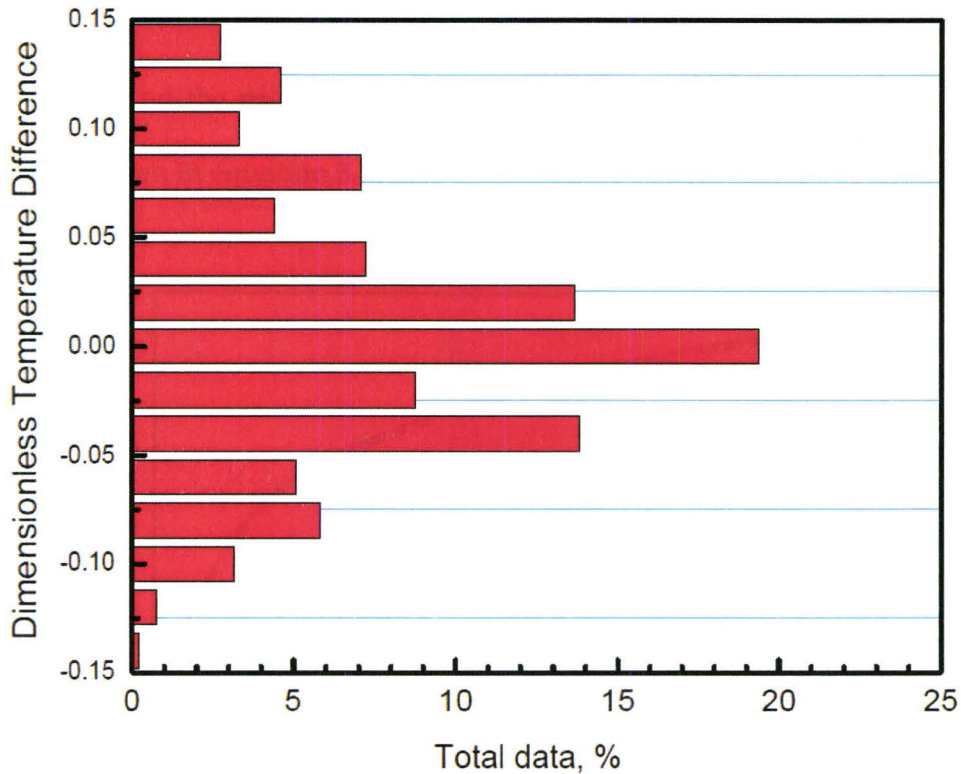


Figure 3.22: Summary of deviation between predicted thermocouple temperatures and measured thermocouple temperatures for all points, shown in Figure 3.12 (Small Shredded scrap, Large shredded scrap and Busheling, Burner power=8.3kW).

The modeled thermocouple temperature is dependent on emissivity of the thermocouple tip and heat transfer coefficient, h_{fs} . Figure 3.23 and Figure 3.24 show the sensitivity of the emissivity and the heat transfer coefficient on predicted thermocouple temperature. It is seen from Figure 3.23 and Figure 3.24 that with 10% variation of both emissivity and heat transfer coefficient the predicted thermocouple temperature varies about 1%. Figures 3.23 and 3.24, show that the effect of emissivity and heat transfer

coefficient on the prediction of thermocouple temperatures are opposite, which is seen in equation 3.39.

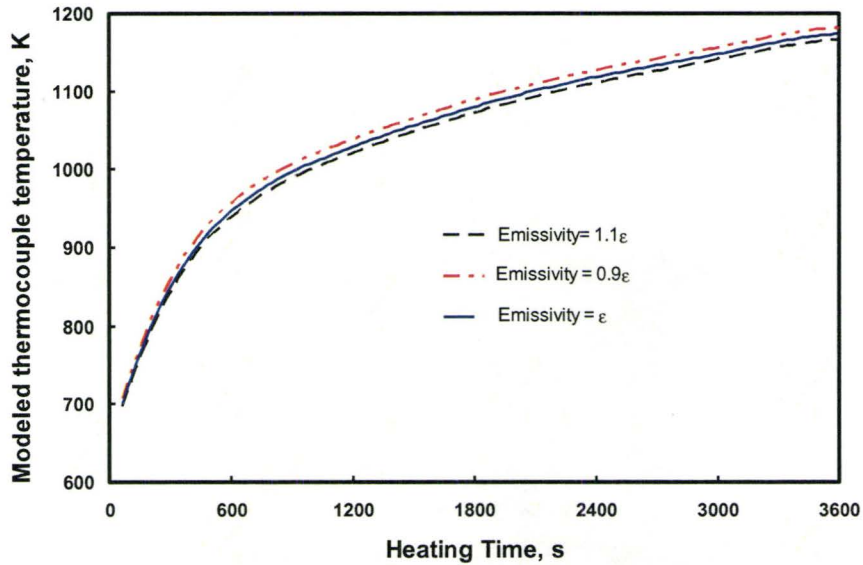


Figure 3.23: Effect of emissivity on modeled thermocouple temperature.

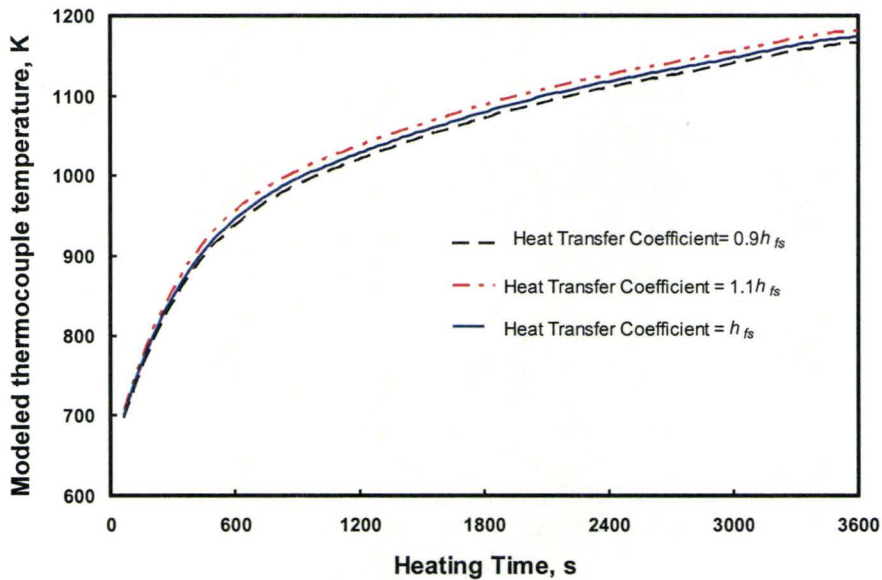


Figure 3.24: Effect of heat transfer coefficient on modeled thermocouple temperature.

3.10 Simulation Results and Discussions

Using tuned parameters heating efficiency of burner i.e., the ratio between the total energy transfer to the scrap and the total energy input by the burner, was evaluated for small shredded scrap. Figure 3.25 shows the heating efficiency of the burner with burner power of 8.3 kW and small shredded scrap. It is seen from Figure 3.25 that heating efficiency of burner decreases with time. This is due to increases of scrap temperature by heating.

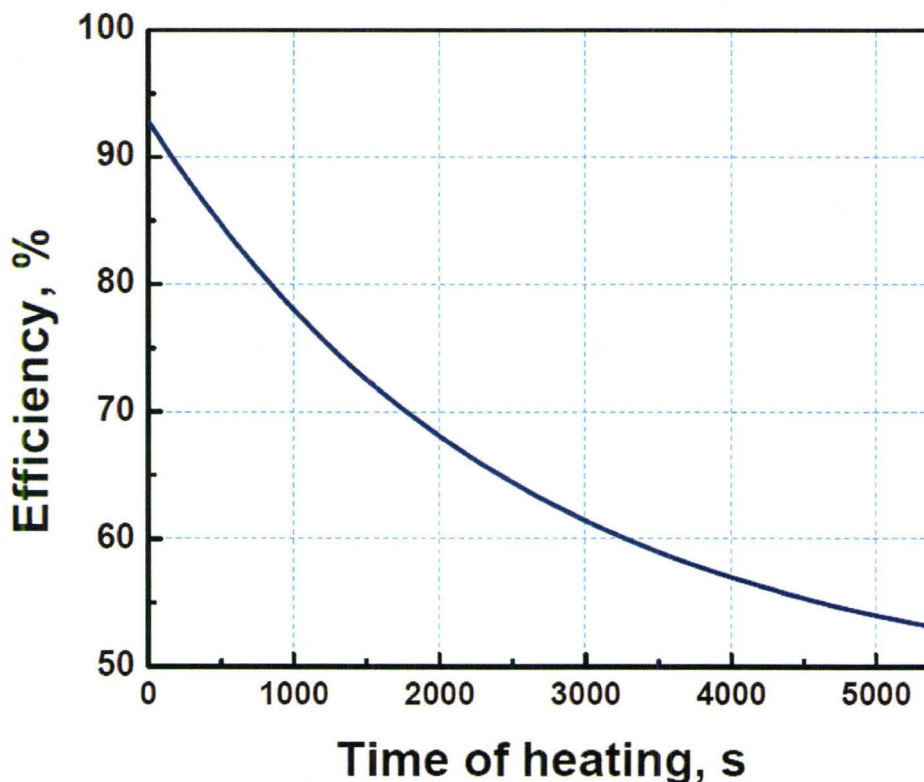


Figure 3.25: Heating efficiency of the burner, Power=8.3kW, Small Shredded Scrap.

Numerically simulated thermocouple temperatures and measured thermocouple temperatures (modeled), in the vertical center plane, shown in Figure 3.12, are shown in Figure 3.26 and Figure 3.27, for after 30 minutes, and 60 minutes of the heating experiment, with burner power 12.8kW for small shredded scrap. It is clear from Figure 3.26 and Figure 3.27, that there is a good agreement between the numerically predicted thermocouple temperatures and measured thermocouple temperatures (modeled), with burner power 12.8 kW for small shredded scrap. Similarly, numerically predicted thermocouple temperatures and measured thermocouple temperatures (modeled), in the vertical center plane are shown in Figure 3.28 for after 30 minutes of the heating experiment, with burner power 17.3kW and small shredded scrap. It is also clear from Figure 3.28 that there is a good agreement between the numerically predicted temperatures and experimentally measured thermocouple temperatures, with burner power 17.3 kW and small shredded scrap. So the fitted characteristic diameter of the particle, d_p , is applicable for small shredded scrap with burner power 12.8 kW and 17.3 kW. Figure 3.29 shows the heating efficiency of small shredded scrap with burner power 8.3 kW, 12.8kW and 17.3 kW. It is seen in Figure 3.29 as burner power increases efficiency decreases over the time.

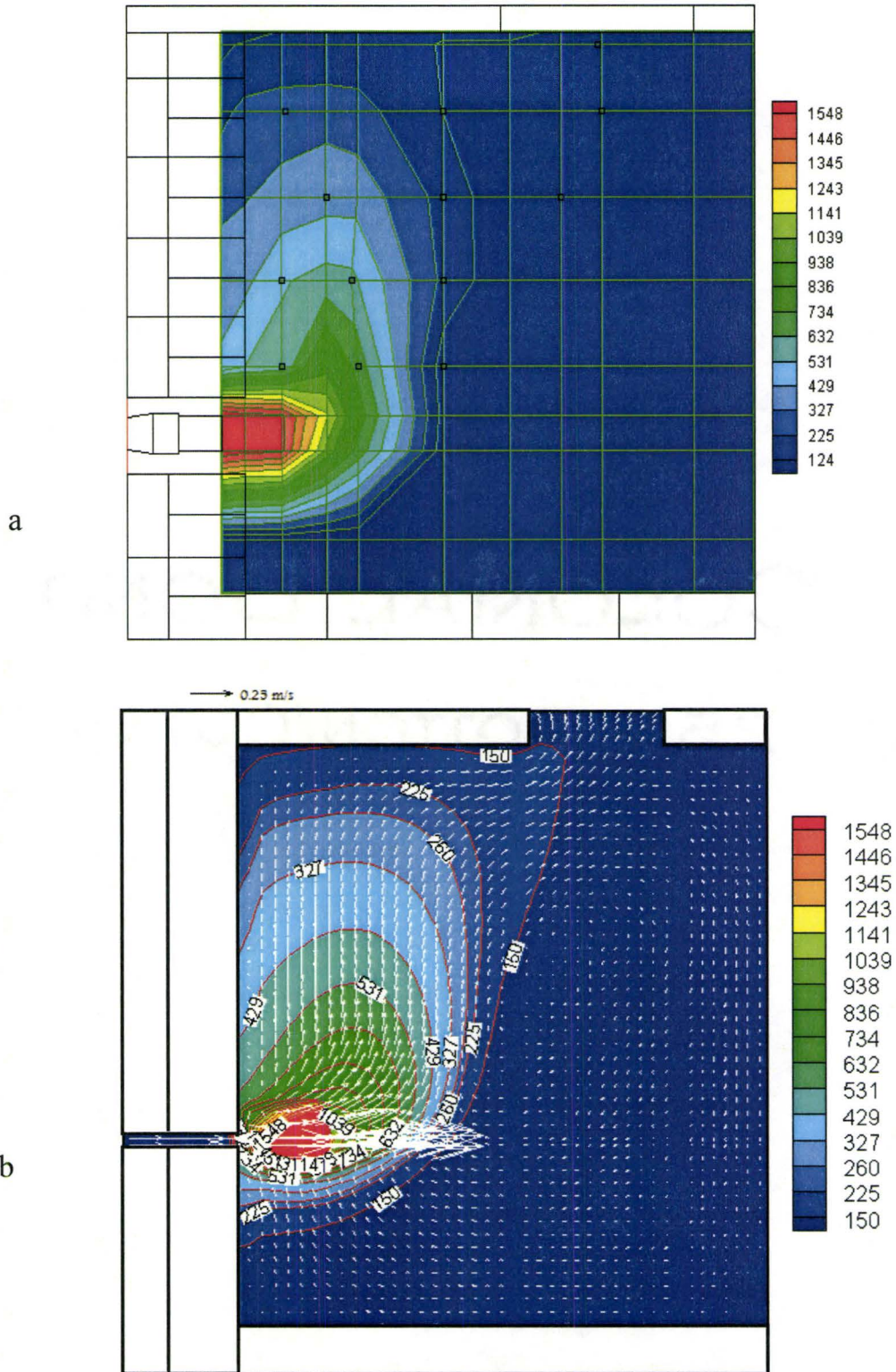


Figure 3.26: Temperature (°C) contour of the furnace after 30 minutes of the experiment with Small Shredded Scrap, Power=12.8 kW, Furnace lid on, a=Measured thermocouple temperatures, b=Predicted thermocouple temperatures

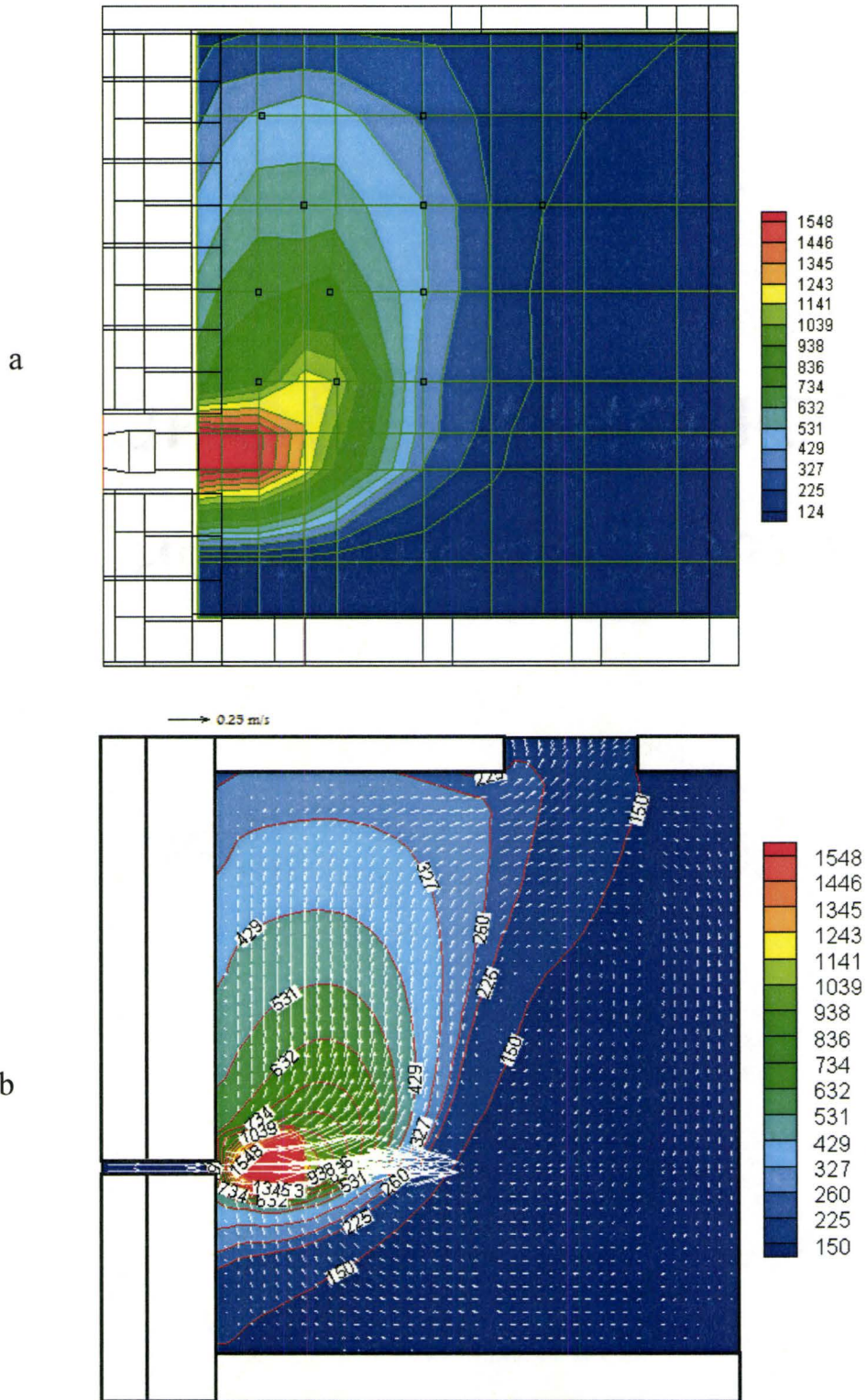


Figure 3.27: Temperature ($^{\circ}\text{C}$) contour of the furnace after 60 minutes of the experiment with Small Shredded Scrap, Power=12.8 kW, Furnace lid on, a=Measured thermocouple temperatures, b=Predicted thermocouple temperatures

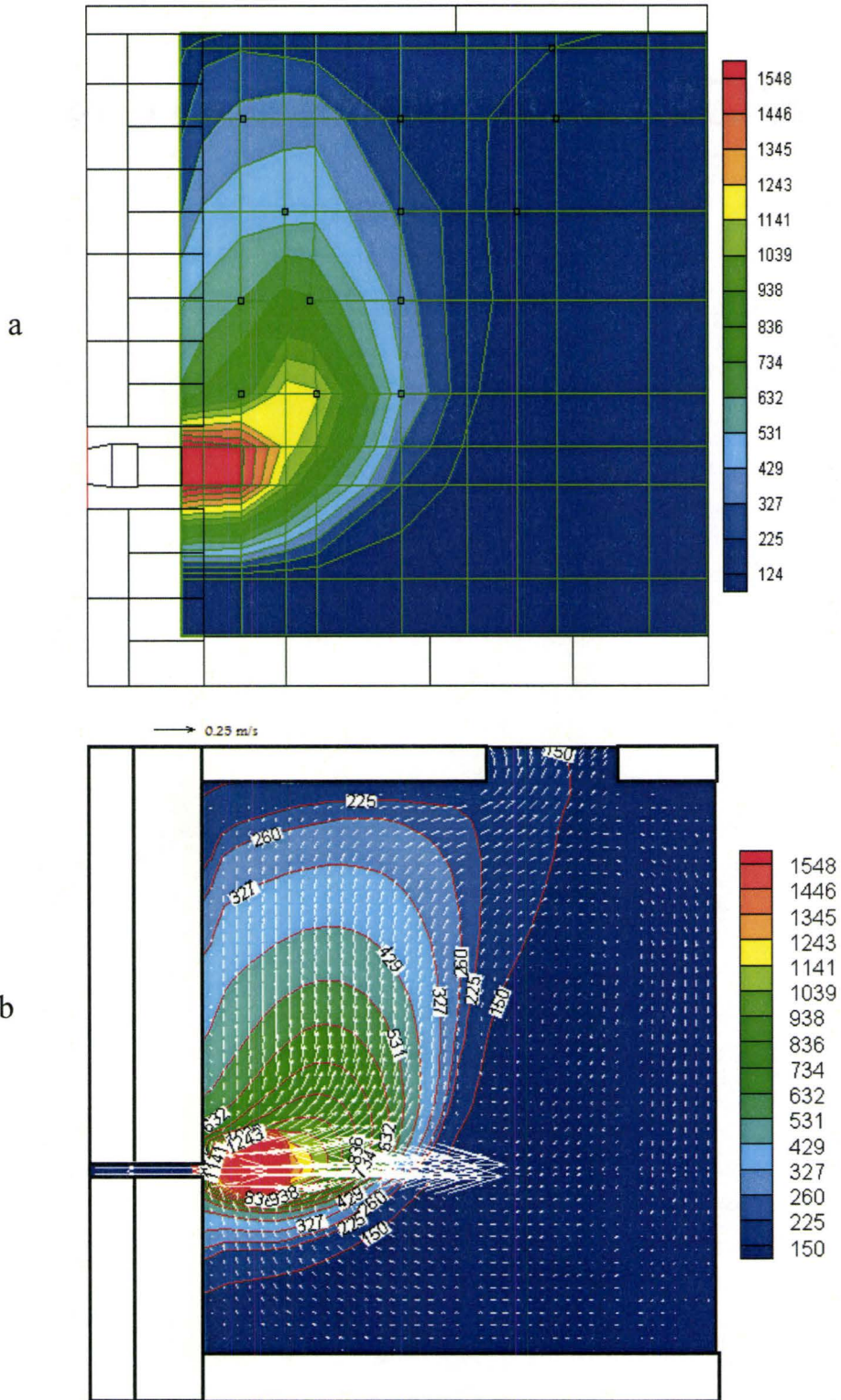


Figure 3.28: Temperature (°C) contour of the furnace after 30 minutes of the experiment with Small Shredded Scrap, Power=17.3 kW, Furnace lid on, a=Measured thermocouple temperatures, b=Predicted thermocouple temperatures

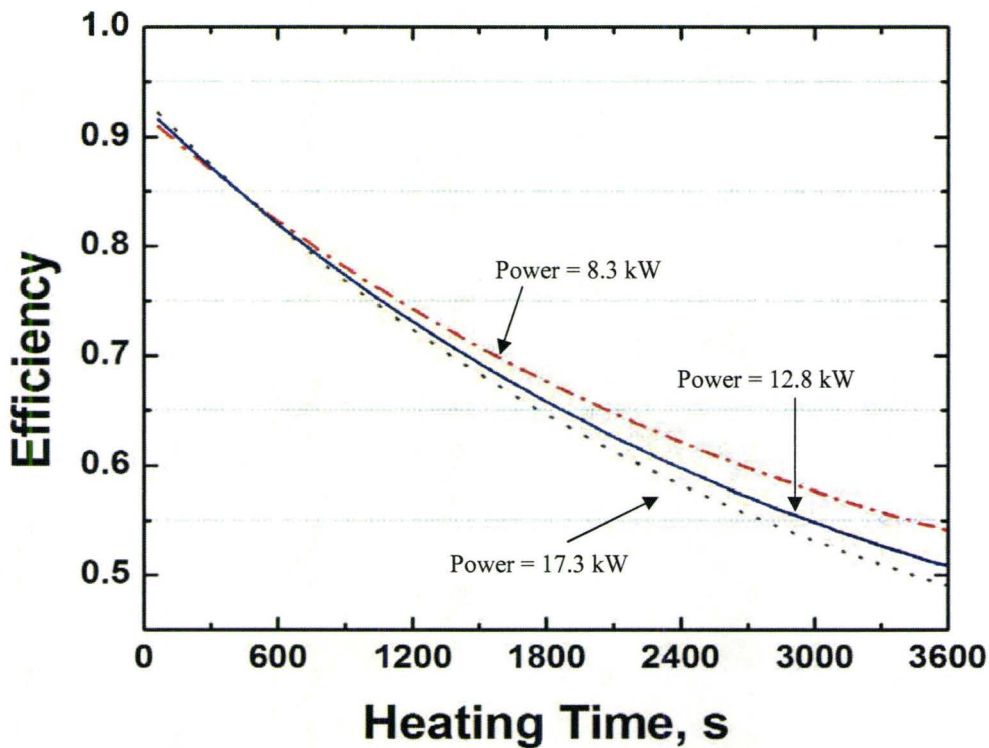


Figure 3.29: Heating efficiency of small shredded scrap using burner power 8.3kW, 12.8kW and 17.3 kW

Numerical simulation was carried out for large shredded scrap. Figure 3.30 shows simulated gas temperatures, in the vertical center plane, shown in Figure 3.12, for after 60 minutes of the heating experiment, with burner power 8.3kW for large shredded scrap. Figure 3.30 should be compared to Figure 2.25a and it is seen there is a good agreement between the numerically predicted temperatures and experimentally measured thermocouple temperatures for large shredded scrap.

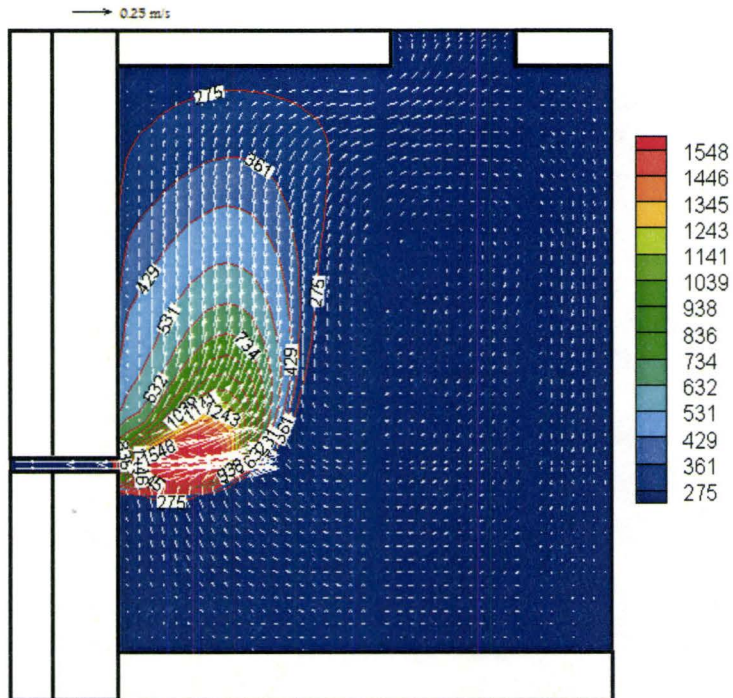


Figure 3.30: Temperature ($^{\circ}\text{C}$) contour of the furnace after 60 minutes of the experiment with Large Shredded Scrap, Power=8.3 kW, Furnace lid on

Simulations were carried out for busheling, sheet metal addition (Figure 2.29) and layers of different scrap (Figure 2.32). Figure 3.31 summarizes the burner heating efficiency for different scrap. It is seen from Figure 3.31 that there is a dramatic effect on heating if a piece of steel sheet is placed in the centre of the scrap pile, which is also seen in Figure 2.31. Also it is clear from Figure 3.31 that burner efficiency is low for busheling compared to small shredded and large shredded scrap. This is due to low scrap density in case of busheling compared to small shredded scrap and large shredded scrap. It is also seen from Figure 3.31 that during initial stage of heating small shredded scrap has higher heating efficiency than

that of large shredded scrap. If scrap is placed in different layers, shown in Figure 2.32, then heating efficiency is similar of small shredded scrap.

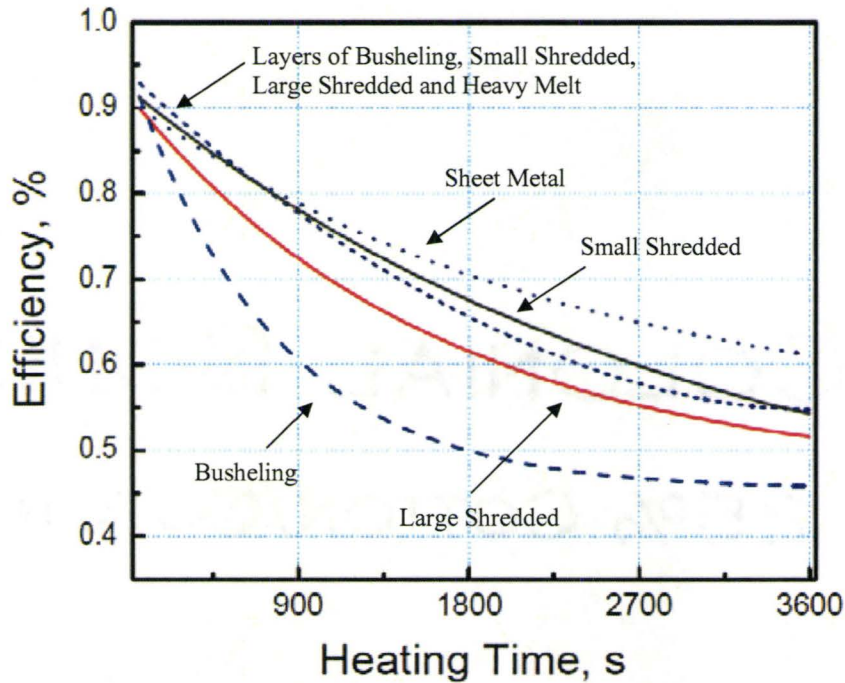


Figure 3.31: Heating efficiency of small shredded scrap, larger shredded scrap, busheling, sheet metal additions and layers of busheling, small shredded, large shredded and heavy melt. Burner Power: 8.3 kW

Directly in front of the burner the scrap was melted by the burner gas which was 1527°C . A cavity was created in a matter of minutes, and then grew no larger. Figure 3.32 shows photographs taken after briefly removing the burner from the furnace. In this case, the melting was complete in about 90 seconds. To handle this phenomenon, the porosity was set to unity, once temperature reached the melting point of the steel.

Figure 3.33 shows the modeled scrap temperature for thermocouples 1 and 2; see Figure 3.12 for the locations. Initially the scrap temperature at thermocouple number one was higher than thermocouple number two and after about 120 seconds of heating, scrap temperature at thermocouple number 2 is higher than thermocouple number 1. As heating progresses scrap in front of the burner melts and the flame penetrates into the furnace. This phenomenon reduces the contact locally, but allows the gases to penetrate further into the scrap which increases the heating efficiency. Figure 3.34 shows the heating efficiency of burner with scrap melting and without scrap melting, which shows that heating efficiency is more if scrap melts in front of the burner.

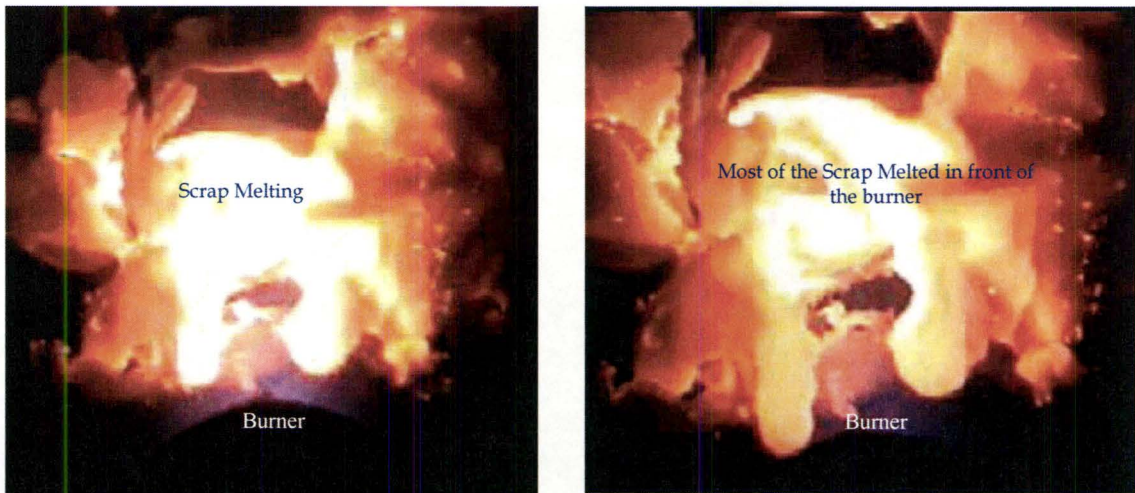


Figure 3.32: Picture in front of the burner after a) 35 seconds of heating and b) 90 seconds of heating.

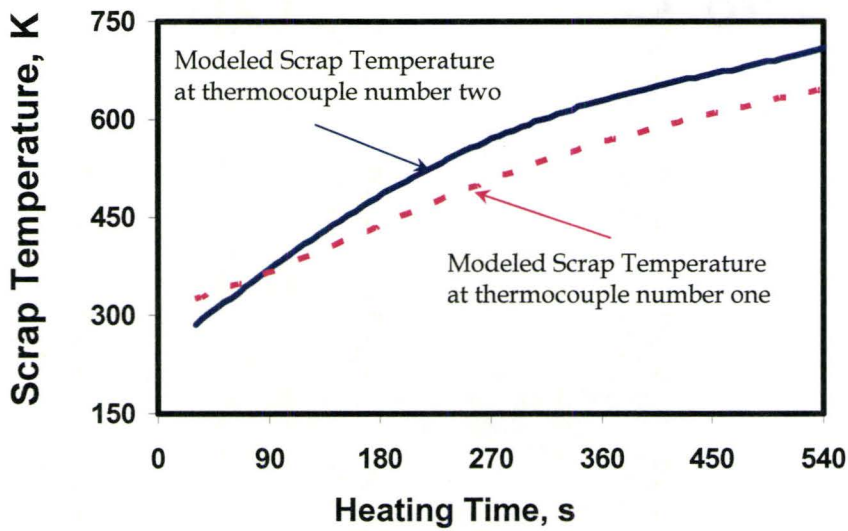


Figure 3.33: Modeled scrap temperature with heating time at thermocouple number one and thermocouple number two. Small Shredded Scrap and Burner Power: 12.8 kW

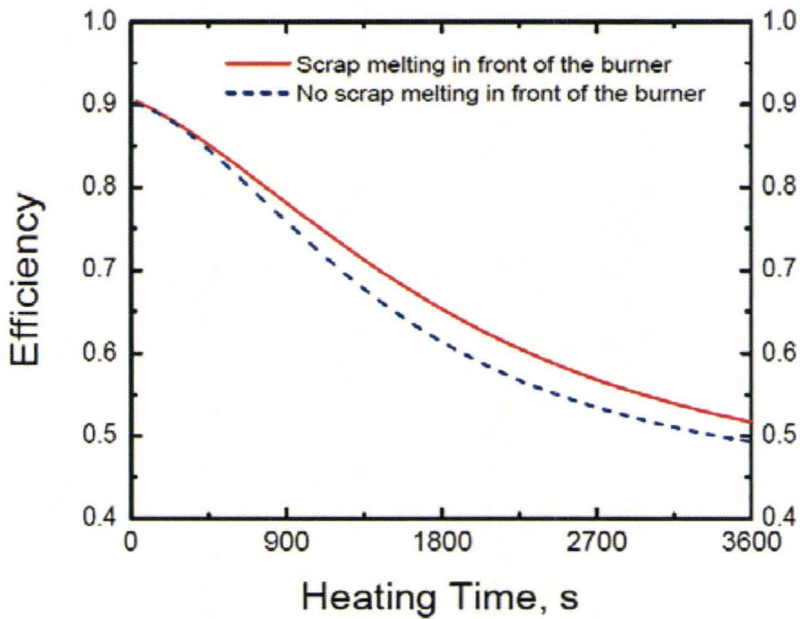


Figure 3.34: Heating efficiency of burner for Small Shredded Scrap, With Scrap melting and without scrap melting Power = 12.8kW, Porosity = Measured Value

3.11 Sensitivity Analysis of Burner Efficiency

3.11.1 Sensitivity of Burner Efficiency on Porosity and Characteristic Particle Diameter

The effect of the tuning parameters on the heating efficiency of burner i.e., the ratio between the total energy transfer to the scrap and the total energy input by the burner, was evaluated for small shredded scrap. The base case is 12.8 kW for small shredded scrap. It was shown in Section 3.9 that in the present numerical model overall heat transfer from burner to scrap depends upon permeability, geometric factor, effective thermal conductivity of fluid, effective thermal conductivity of solid and heat transfer coefficient between fluid and solid. All the above mentioned parameters are dependent on the characteristic particle diameter and porosity. A sensitivity analysis was performed to study the dependency of characteristic particle diameter and porosity on heating efficiency of burner. Figure 3.35 shows that there is a small dependency of characteristic particle diameter on heating efficiency of burner. Figure 3.36 shows strong dependency of porosity variation on heating efficiency of burner. The heating efficiency of the burner increases as porosity decreases.

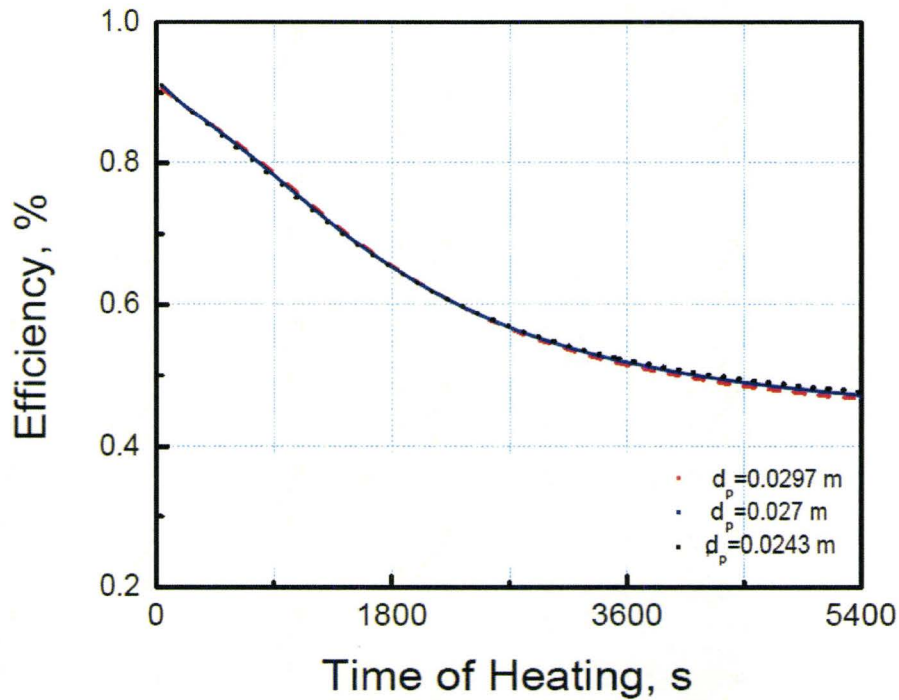


Figure 3.35: Heating efficiency of the burner for different characteristic particle diameter, Power = 12.8kW, Porosity = Measured Value, Small Shredded Scrap.

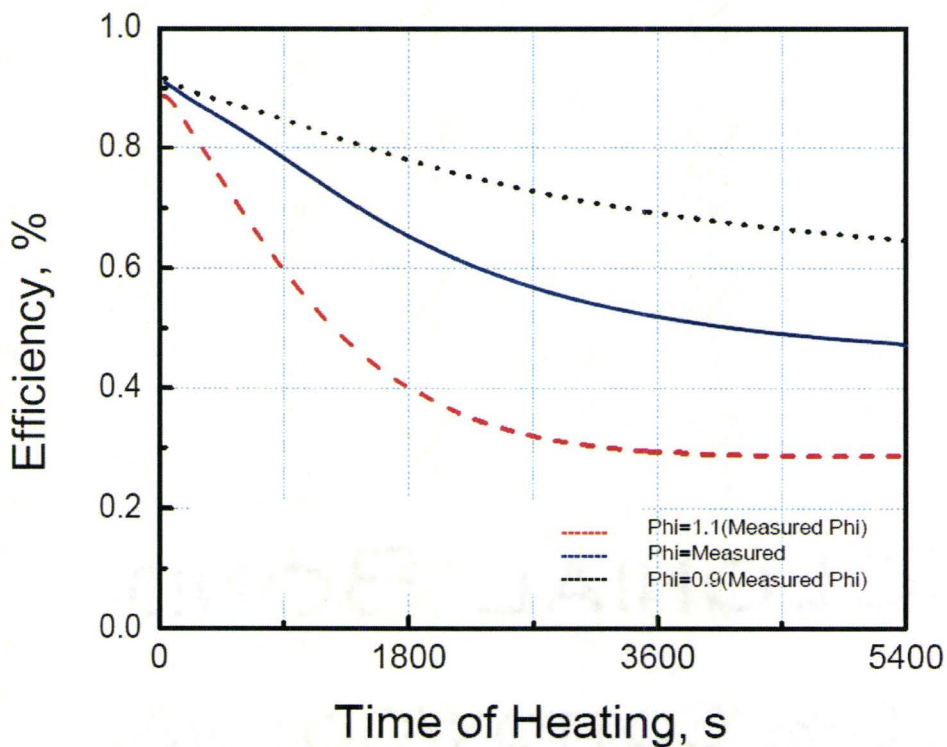


Figure 3.36: Heating efficiency of the burner for different porosity, Power = 12.8kW, Porosity = Measured Value, Small Shredded Scrap.

Figure 3.35 shows that there is negligible dependency of burner efficiency on characteristic particle diameter of the bed on the other hand Figure 3.36 shows that there is strong dependency of burner efficiency on porosity of the bed. The reason behind this dependency is explained here. Table 3.6 shows the values of permeability, K , geometric factor, F , and heat transfer coefficient between fluid and solid, h_{fs} , for small shredded scrap with different characteristic particle diameter and porosity. The corresponding particle Reynolds number is also shown in Table 3.6. It is seen in Table 3.6 that as characteristic particle diameter increases from 0.027 m to 0.0297 m (i.e., 10%) the volumetric heat transfer coefficient i.e., $h_{fs}a_s$, decreases from 651.66 $\text{Wm}^{-2}\text{K}^{-1}$ to 568.19 $\text{W m}^{-2}\text{K}^{-1}$. In this calculation velocity was taken constant. On the other hand volumetric heat transfer coefficient decreases from 651.66 $\text{Wm}^{-2}\text{K}^{-1}$ to 251.35 $\text{Wm}^{-2}\text{K}^{-1}$ when porosity increases by 10%. Volumetric heat transfer coefficient decreases from 651.66 $\text{Wm}^{-2}\text{K}^{-1}$ to 265.18 $\text{Wm}^{-2}\text{K}^{-1}$ when porosity increased by 10% (from 0.86 to 0.946) and velocity increased by 10%, which is shown in Table 3.6. So porosity change has strong effect on heating efficiency of burner compared to characteristic particle diameter.

Table 3.6: Values of K , F and h_{fs} for small shredded scrap with different characteristic particle diameter and porosity ($P_r=0.688$)

d_p (m)	ϕ	$1/K$ $\left(K = \frac{\phi^3 d_p^2}{150(1-\phi)^2}\right)$	F $\left(\frac{1.75}{\sqrt{150\phi^{3/2}}}\right)$	Re $\left(\frac{\rho u d_p}{\mu}\right)$	h_{fs} $\left(K_f \frac{(2+1.1Pr^{1/3} Re^{0.6})}{d_p}\right)$ ($Wm^{-2}K^{-1}$)	a_s $\left(\frac{6(1-\phi)}{d_p}\right)$ (m^{-1})	$a_s \cdot h_{fs}$ ($Wm^{-3}K^{-1}$)
0.0270	0.860	6340	0.179	280*	20.94	31.11	651
0.0297	0.860	5240	0.179	308*	20.08	28.28	568
0.0270	0.946	708	4.130	280*	20.94	12.00	251
0.0270	0.946	708	4.130	308**	22.09	12.00	265

* Velocity was taken constant as 0.1 m/s.

** Velocity was taken as 0.11 m/s, velocity increased by 10%.

3.11.2 Sensitivity of Burner Efficiency on Scrap Distribution inside the Furnace

Figure 3.37 shows the fluid flow pattern if a piece of scrap is placed in front of the burner i.e., flame blocking. Figure 3.38 shows the heating efficiency of burner for the same. It is seen from Figure 3.37 that heating efficiency decreases if a piece of scrap blocks the flame. A piece of scrap restricts the flame to go deeper into the furnace, hence lower efficiency. It is seen from Figure 3.37 that scrap blocking forces the hot combusted gas to take shorter path i.e., near the wall, therefore the contact length between hot gas and scrap decreases, hence lower heating efficiency. It indicates that if a heavy scrap is placed in front of the burner refractory and burner could be damaged due to high local temperature from blow back of the flame. Figure 3.39 shows the heating efficiency of the burner with different center porosity of the furnace. Figure 3.39 shows that the heating efficiency increases drastically with changing center porosity of

0.75 to 0.5. Heating efficiency does not change significantly if porosity is decreased below 0.5. The volumetric heat transfer coefficient increases as porosity decreases, but after a certain point the hot gases take the path of least resistance and go around the denser section in the middle of the furnace, hence heating efficiency of the burner does not improve below the porosity of 0.5. Figure 3.40 shows the fluid flow pattern if a big piece of solid scrap is placed in the middle of the furnace. In this case efficiency of the burner also decreases, which is shown in Figure 3.41. Here the combusted gas short circuits the high density scrap in the middle so the overall burner efficiency decreases. So it can be concluded that the uniformity of the scrap inside the furnace is important.

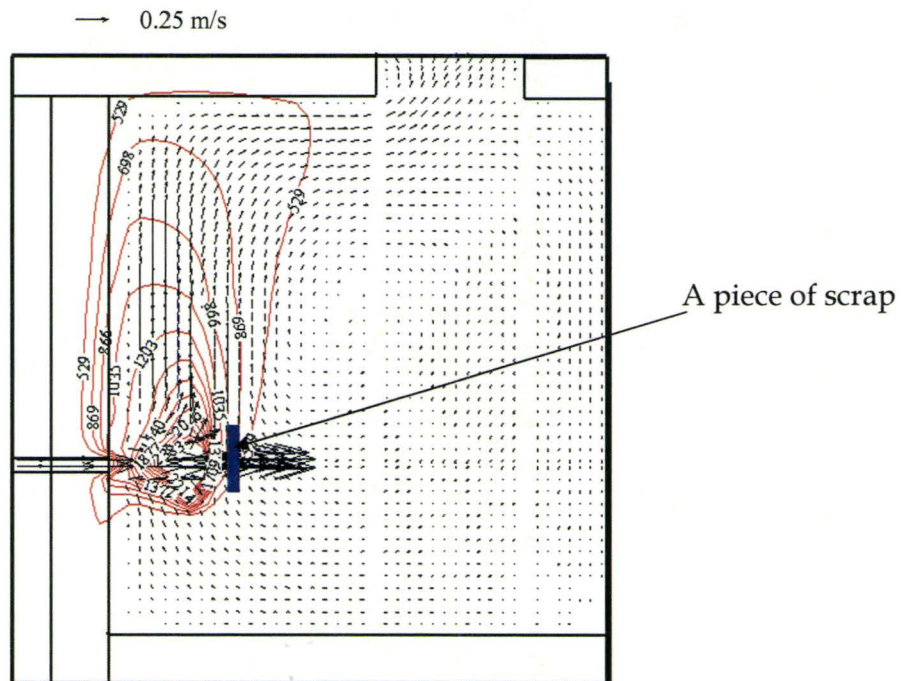


Figure 3.37: Vector plot and temperature contour after 60 minutes of heating, Power = 12.8kW, Porosity = Measured Value.

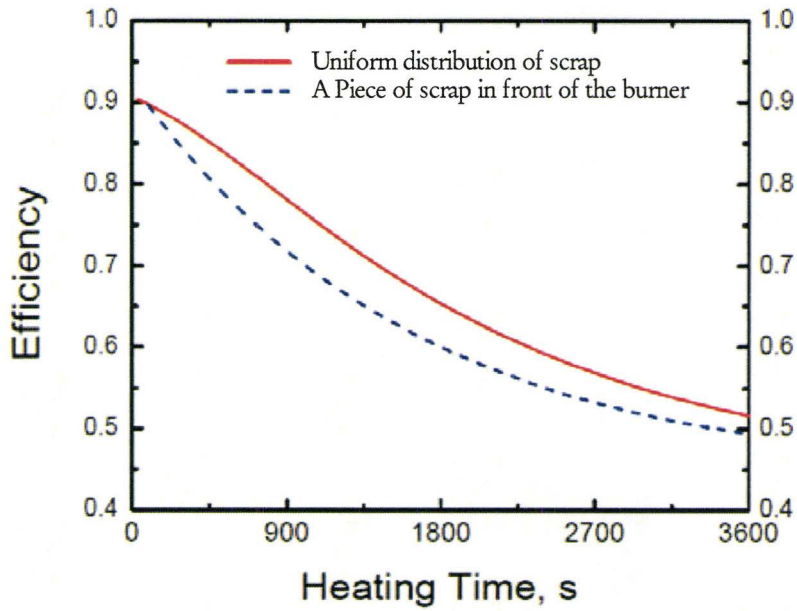


Figure 3.38: Heating efficiency of burner for Small Shredded Scrap, Power = 12.8kW, Porosity = Measured Value.

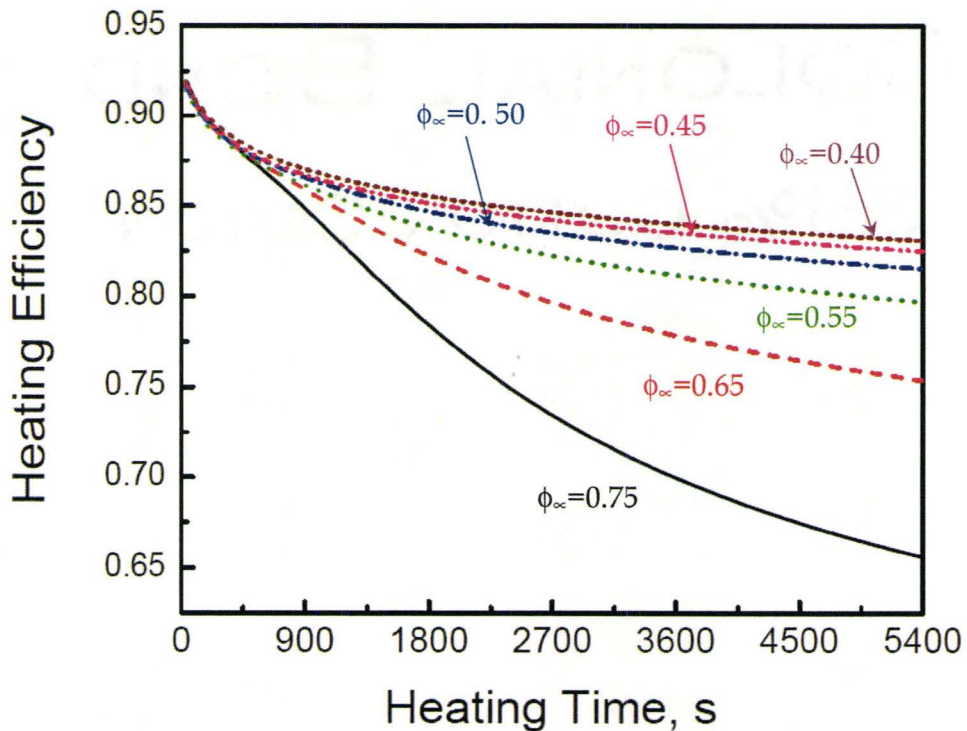


Figure 3.39: Heating efficiency of burner for Small Shredded Scrap, with different porosity of the furnace, Power = 12.8kW.

→ 0.25 m/s

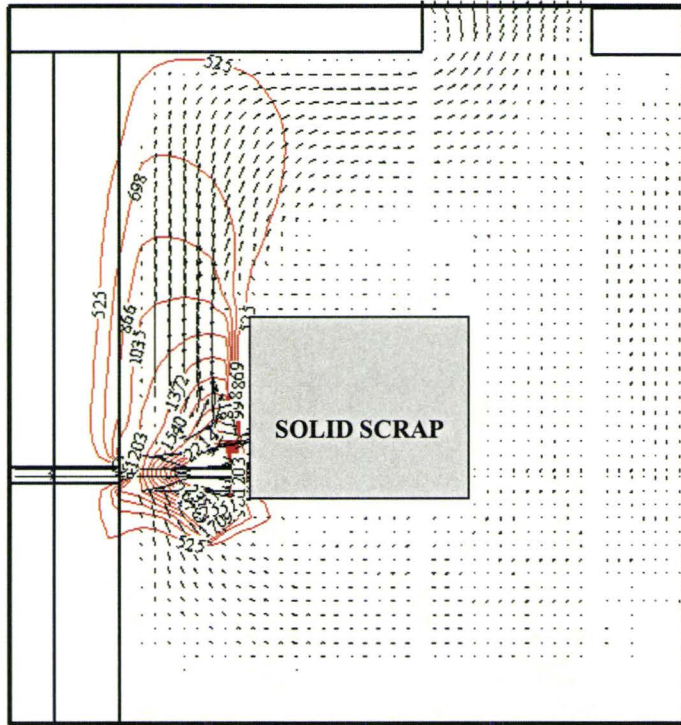


Figure 3.40: Vector plot and temperature contour after 60 minutes of heating, Power = 12.8kW, Porosity = Measured Value, A solid scrap in the middle of the furnace.

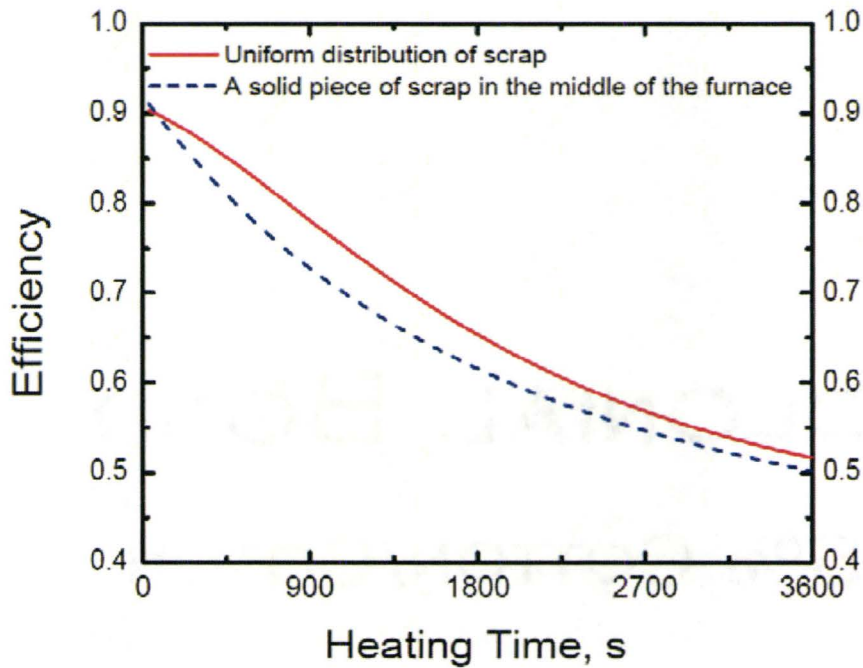


Figure 3.41: Heating efficiency of burner for Small Shredded Scrap, Power = 12.8kW, Porosity = Measured Value.

3.11.3 Sensitivity of Burner Efficiency on Radiation

A simulation was carried out to study the effect of radiation on the burner efficiency on heating. Figure 3.42 shows the heating efficiency of the burner with burner power of 12.8 kW and small shredded scrap, considering radiation and without radiation inside the scrap bed. Figure 3.42 shows that the difference between efficiencies of burner with radiation consideration and without radiation, increases with time. As heating time progress as the overall scrap temperature increases hence heating efficiency difference increases with heating time.

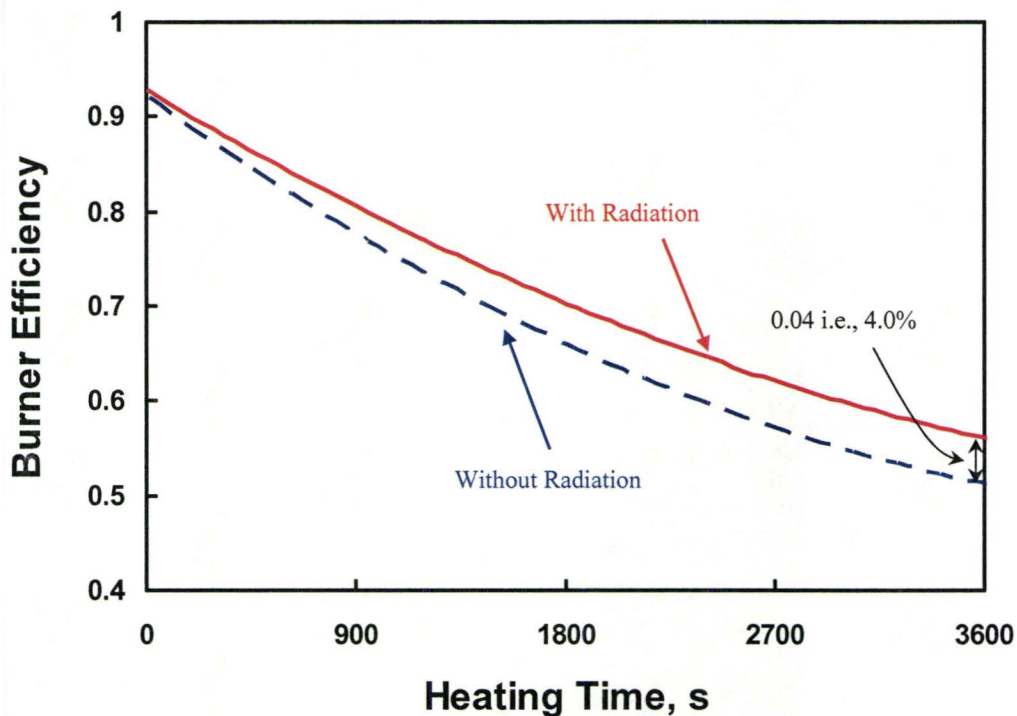


Figure 3.42: Heating efficiency of small shredded scrap using burner power 12.8kW considering radiation and without radiation

3.11.4 Sensitivity of Burner Efficiency on Turbulence

A simulation was carried out to study the strength of turbulence consideration (Section 3.3), on burner efficiency. Figure 3.43 shows the heating efficiency of the burner with burner power of 12.8 kW and small shredded scrap, considering porous media turbulence and without porous media turbulence and laminar. It is seen from Figure 3.43 that turbulence does not have impact on burner efficiency, because heat transfer between burner and scrap is governed by the heat transfer coefficient and the heat transfer coefficient already has turbulence effect included.

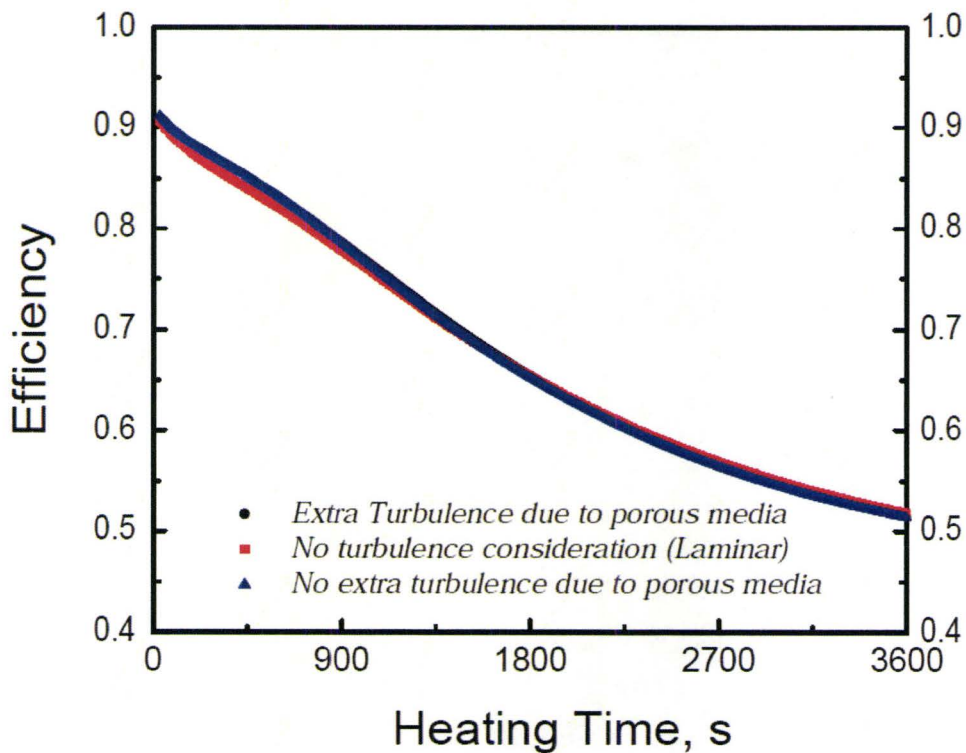


Figure 3.43: Heating efficiency of small shredded scrap using burner power 12.8kW considering extra turbulence due to porous media and without extra turbulence

Chapter 4

Conclusions

In the present research an experimental and numerical study of steel scrap heating phenomena was carried out using an oxy-fuel burner in a small-scale furnace (1 m³) for a range of burner power, scrap type and furnace configurations.

Several measurements were carried out during the research, which include; scrap size and density, porosity distribution, extent of combustion, scrap oxidation and temperature distribution during heating.

The key conclusions from the experiments include:

1. The porosity approached 1 near the wall, and decreased towards the center of the bed, and remained constant after an average particle length for both small shredded scrap and large shredded scrap. The porosity distribution pattern for busheling and large spherical shaped particles from the wall to the center of the bed was random. This anomaly was due to large size of busheling and large spherical particles compared to the plexiglass measurement vessel.

2. The furnace roof caused the combustion gases to flow across the furnace to reach the chimney on the other side, which changed the flow pattern and consequently the heating pattern. There was better heating with the furnace cover on compared to furnace cover off because the contact length between the scrap and gas was increased in the case of furnace cover on.
3. Apparent heating efficiency decreased with time as the scrap heated up; the thermal driving force was decreased. Measured efficiencies were very high in the initial stage of heating.
4. A steel sheet placed horizontally in the middle of the furnace had a strong effect on heating ("sheet metal" experiments). The steel sheet modified the flow and increased the effectiveness of the heating, which could be used for the design of separate scrap heating furnaces.

For accurate prediction of flow and temperature field for the scrap heating by burners variable porosity, non-Darcian, turbulent flow with separate temperatures for gas and solids need to be considered. To handle these issues an in-house computer model was developed, considering non-uniform porosity inside the furnace, turbulence, and dynamic behavior of porosity due to localized melting.

The major challenges during numerical modeling were to use appropriate model parameters such as; porosity variation inside the furnace, permeability of the bed, drag coefficient of the bed, effective thermal conductivity of the bed, fluid to solid heat transfer coefficient and radiation inside the bed. Porosity variation inside the furnace was modeled according to the experimental data. Due to lack of literature of porous media fluid flow and heat transfer for irregular shaped particles and complexity of the problem a detail analysis and considerations of the model parameters were performed. Model parameters were dependent upon porosity of the bed and characteristic particle diameter. Measured porosity variations were used for numerical simulation and characteristic particle diameter for different scrap was tuned to match the experimental results with numerical simulation. Using tuned characteristic particle diameter simulations were performed for different scrap with different furnace configurations.

This appears to be the first time a numerical model for heat transfer between flame and scrap was developed and validated with the experimental data. The key conclusions include:

- 1 The thermocouple temperature must also be modeled since it is between the gas and solid temperature. A simple balance between

radiation and convection at the thermocouple surface provided good agreement between the experiments and model.

2. Tuned characteristic particle diameter for small shredded scrap, large shredded scrap and busheling were 27 mm, 28.5 mm and 26 mm, respectively. So, scrap size is not an important factor for heat transfer between burner and scrap.
3. Burner heat transfer efficiency increased dramatically as porosity was decreased (scrap density increased) because the surface area of the scrap increased. However, decreases below 0.5 did not improve the heating efficiency of the burner because of short circuiting of the gas at the walls.
4. On the other hand burner efficiency decreased slightly as characteristic particle size increased.
5. Model shows a scrap piece in front of the burner reduced the efficiency of the burner, as did a large piece of scrap in the furnace. Therefore, uniformity of scrap porosity is important for high efficiency of heat transfer.
7. Therefore, it is better to have dense scrap of uniform density in front of the burners for highest heating efficiency. Large pieces which deflect the gas flow are detrimental to efficiency and can create damage to the burner or wall.

8. In front of the burner, scrap melted and due to localized melting a narrow channel formed and flame penetrated deeply, which heated the scrap more.
9. Heating efficiency drops as the scrap heats. The present model may be useful for determining the most economical time to turn off the burners.
10. Heating efficiency was highest for the "sheet metal" experiments in which a horizontal sheet of steel increased the contact time between the gas and steel scrap. This concept may be useful for scrap preheating chambers.

The scope of the present research can be further expanded considering the following:

1. In the present work, subsonic burner was used for the experimental study. So, present experimental study can be modified for supersonic burner. Also, a large scale heating furnace can be considered for the heating experiments (e.g., full scale).
2. The temperature variation inside the scrap was ignored due to low Biot number for small scrap size. So, for larger scrap temperature variation inside the scrap can be examined. Perhaps, thermocouples should be imbedded in the scrap.

Appendix A

CO₂ Adsorption/Elution Phenomena by Different Drying Agents

Carbon dioxide is a common component in gas streams that either enter or leave metallurgical processes. Often water vapor is in the gas stream as well, so the first step in the chemical analysis of the streams for CO₂ is to remove the water vapor by passing the gas through a packed bed of a drying agent, such as silica gel, calcium sulphate or calcium chloride. CO₂ is also adsorbed on these drying agents, so considerable error in CO₂ analysis may arise. In this Communication the problem is assessed and procedures to overcome it are discussed.

Previous work in this area has been restricted to gases containing less than 1% CO₂ (Elia et al, 1986 and Babrauskas and Thureson, 1994). Elia et al, 1986, reported the errors in measurements of CO₂ concentration that takes place in the use of drying agents in medical research. Using standard gas mixtures they assessed the adsorption and elution behavior of CO₂ on calcium chloride, calcium sulphate, alumina, silica gel and magnesium perchlorate. According to their results the response time to achieve accurate results is independent of the concentration of CO₂ (0-1%), but is

dependent of flow rate, amount and type of drying agent used. Babrauskas and Thureson 1994, tested the adsorption and elution behavior of silica gel, calcium sulphate and calcium chloride, but they did not report the amount of materials used. Their standard gas composition was around 0.12% CO₂. In the present processes, the CO₂ content of the gas mixture is far more than 1%, yet there is no information available regarding CO₂ adsorption and elution phenomena. Therefore, the present study was carried out to evaluate the errors that may arise during drying of the gas mixtures with high concentrations of CO₂, by using silica gel, calcium chloride and calcium sulphate.

Gas mixtures were prepared by mixing a metered rate of CO₂ with a metered rate of N₂ from cylinders to obtain 5, 15 or 25% CO₂. The gases were analyzed continuously with a Horiba gas analyzer (Model: VIA-510), based on non-dispersive infrared analysis method. The results were also compared with samples taken by syringe and analyzed in a Gas Chromatograph. A certified gas composition from BOC Canada of 5.02% O₂, 6.24% CO, 6.8% He, 25.08% CO₂ and the balance N₂ was used for calibration. It was found that the error in CO₂ composition was in the range of ± 1 percent of reading for all the cases.

Silica gel, grade 49 of mesh size 6-18, was obtained from EMD Chemicals, Darmstadt, Germany. Calcium chloride of mesh size 4 -20 was obtained from Fisher Chemicals, New Jersey, USA. CaSO_4 of mesh size 8, was obtained as DrieriteTM which contains less than 2% of COCl_2 as a color indicator from W. A. Hammond Drierite Company Ltd, Xenia, Ohio, USA.

A schematic of the experimental setup is shown in Figure A1. Glass tubing was used in the entire gas train. Before starting each experiment the Horiba gas analyzer was calibrated with the certified gas mixture. After calibration a controlled gas flow of known composition was passed through the drying agent for the various experiments. The results are presented in terms of the time for the Horiba gas analyzer to respond to the gas composition. When the response reaches 100% of the reading, it means that the drying agent has reached steady state and the analyzer is reporting the true CO_2 gas composition. The transit time of the gas through the system was 5.5 seconds, much shorter than the measured response times.

The effects of adsorption and elution of CO_2 at a fixed flow rate are shown in Figures A2 and A3, respectively, for calcium chloride, calcium sulphate and silica gel. It is clear that the CO_2 adsorption capacity decreases from silica gel, to calcium sulphate and finally calcium chloride. Figure A2 and

A3 are inversions of each other, suggesting that the CO₂ adsorption/elution phenomena for different drying agents are reversible.

To study the effect of column shape 3 height-to-diameter ratios, (9, 17 and 26) with a fixed mass of 105 grams of silica gel was tested in the adsorption mode. The results in Figure A4 show that there is no appreciable shape effect for these conditions.

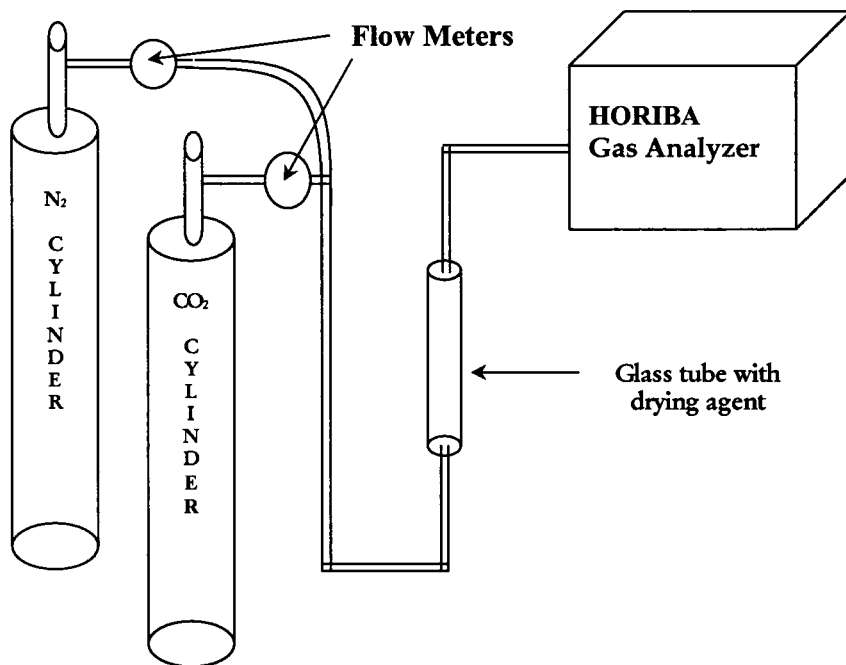


Figure A1: Experimental Setup for CO₂ measurement error analysis

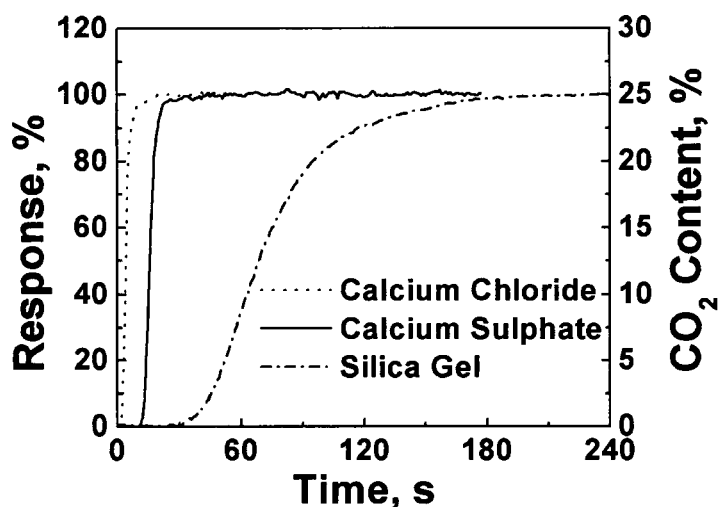


Figure A2: Response time for the anhydrous drying agents to CO₂ adsorption from a gas mixture of 25% CO₂ and 75% N₂. The gas flow rate 1.6 l/m and the mass of the drying agents 105 gm for H/D of 17

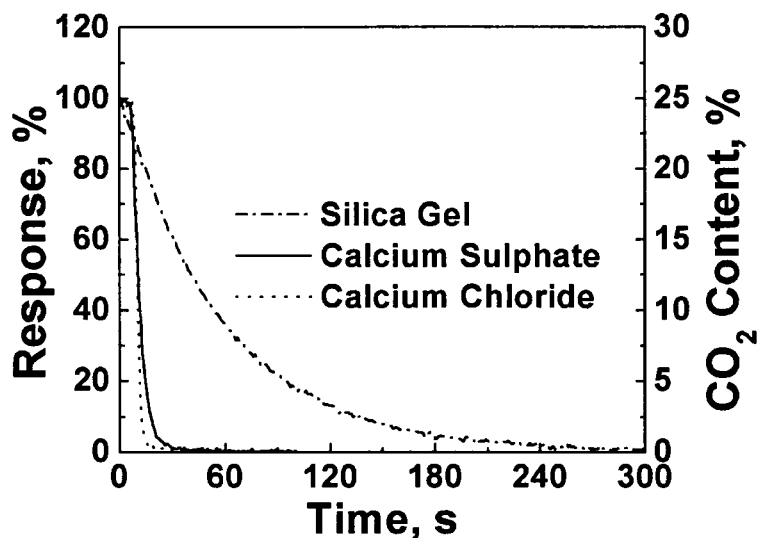


Figure A3: Response time for the anhydrous drying agents to CO₂ elution from a gas mixture of 25% CO₂ and 75% N₂, The N₂ flow rate was 1.6 l/m and the mass of the drying agent was 105 gm for H/D of 17.

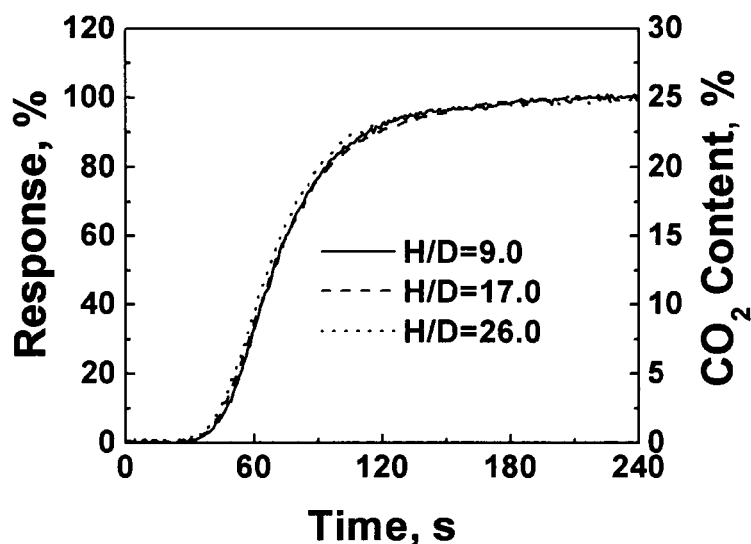


Figure A4: Response time for anhydrous silica gel for different height-to-diameter ratios on CO₂ adsorption from a gas mixture of 25% CO₂ and 75% N₂. The gas flow rate was 1.6 l/m and the mass of the driving agent was 105 gm.

Silica gel was used to study the CO₂ adsorption response time for different gas compositions and different gas flow rates. It was observed that when the CO₂ composition increased from 5 to 25 there was no significant change in the response time. This is consistent with the previous findings (Elia et al, 1986) in the range of 0-1% CO₂. On the other hand, the gas flow rate affects the response time as shown in Figure A5. The time to reach various response levels is in inverse proportion to the flow rate. Therefore, adsorption depends on the number of moles passing through the bed for these selected conditions.

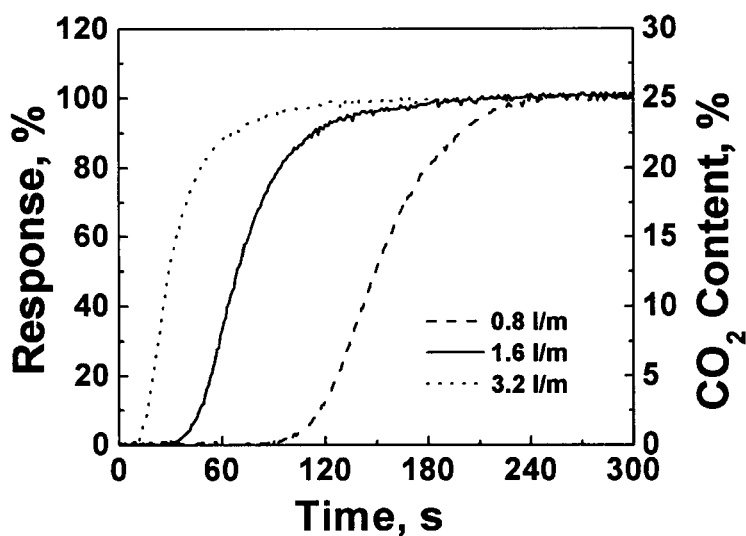


Figure A5: The response time for anhydrous Silica Gel for gas flow rates 0.8, 1.6 and 3.2 l/m to CO₂ adsorption from a gas mixture of 25% CO₂ and 75% N₂, for a mass of 105 gm.

To study the effect of the extent of hydration of the drying agent, moist air was passed through the column for several hours to ensure that it was saturated with moisture. Figure A6, shows that the saturated drying agent adsorbs very little CO₂, and has a very rapid response time. It is similar to the findings of Elia *et al.* 1986.

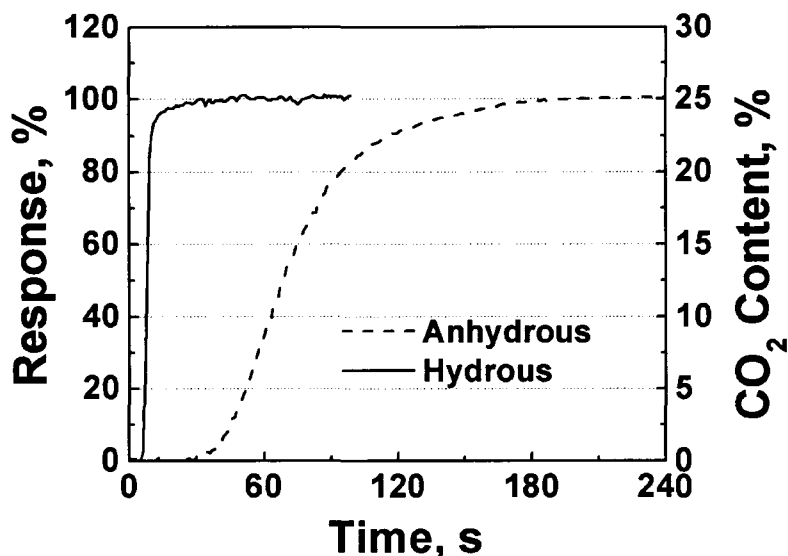


Figure A6: Percent of response time for hydrous silica gel, on CO₂ adsorption from a gas mixture of 25% CO₂ and 75% N₂, gas flow rate 1.6 l/m, mass of the silica gel is 105.00 gm.

This study of CO₂ adsorption/elution phenomena by different drying agents shows that precautions should be taken to ensure that samples of gas contain the true CO₂ content for chemical analysis. The present results show that times of the order of 2 or 3 minutes are required for a proper reading; this time varies depending on the drying agent, flow rate and amount of drying agent, so preliminary tests should be performed for each apparatus. Figure A2 shows that calcium chloride has the fastest response. The disadvantage of calcium chloride is that when it absorbs water, the particles bond together and become solid and the permeability of the bed drops. Therefore, calcium chloride may not be practical when

the moisture content of the gas is high. Calcium sulphate has a higher moisture capacity compared to calcium chloride, but a slower response for CO₂ analysis. Silica gel has the highest capacity to absorb water, but takes much longer to obtain a true CO₂ analysis. However, for gases with high moisture contents, silica gel may be the best choice for a drying agent. Both calcium sulphate and silica gel are available with color indicators that turn pink after hydration. Finally, with the knowledge of CO₂ adsorption/elution phenomena of calcium chloride, drierite and silica gel, errors in CO₂ measurements were avoided.

Appendix B

Tri-Diagonal Matrix Algorithm (TDMA)

The resultant set of discretization equations for both boundary and internal nodes were solved using the Tri-Diagonal Matrix Algorithm (TDMA) adopting a line-by-line solution procedure. In this, a particular grid line, say in X-direction, was chosen and the dependent variables were guessed in Y and Z-directions, the problem was thus reduce to a pseudo one-dimensional situation and subsequently solved by TDMA. This was applied to all the grid lines in one direction and the entire process was repeated for the other two space directions to obtain a tentative solution of the dependent variable, ϕ . This typically constituted one iteration. The total number of iterations required was decided by the convergence criteria adopted, which in the present study was defined according to;

$$\sum \sum \sum (A_p \phi_p - (\sum A_{nb} \phi_{nb} + S_C Vol)) < \epsilon_\phi$$

..... (B-1)

in which, $A_{nb}\phi_{nb} = A_E\phi_E + A_W\phi_W + A_N\phi_N + A_S\phi_S + A_T\phi_T + A_B\phi_B$. The triple sum represents the summation over the entire three dimensional domain. Under relaxation of dependent variables were employed to achieve/enhance convergence. The ε_ϕ value acceptable as an indication of convergence on any variable was set to be smaller than 10^{-3} . The value of ε_ϕ was taken 10^{-4} for temperatures.

Appendix C

Partial Elimination Algorithm (PEA)

Discretized energy equations (Patankar S. V., 1980) for fluid and solid phase for the porous media are:

$$A_p^f T_p^f = \sum A_{nb}^f T_{nb}^f + B^f + \lambda(T_p^s - T_p^f) \dots\dots\dots (C-1)$$

and

$$A_p^s T_p^s = \sum A_{nb}^s T_{nb}^s + B^s + \lambda(T_p^f - T_p^s) \dots\dots\dots (C-2)$$

where, subscripts *f* and *s* identify the coefficients for fluid and solid phases. *B* is discretized source term and λ is given by $h_{fs}A_s\Delta V$, where ΔV is the volume of the control volume around the center point *P*. The discretized fluid and solid phase equations can be re-arranged as:

$$(A_p^f + \lambda)T_p^f = \sum A_{nb}^f T_{nb}^f + B^f + \lambda T_p^s \dots\dots\dots (C-3)$$

and

$$(A_p^s + \lambda)T_p^s = \sum A_{nb}^s T_{nb}^s + B^s + \lambda T_p^f \dots\dots\dots(C-4)$$

In the decoupled solution procedure first fluid temperatures were solved using currently available solid temperatures and then solid temperatures were solved using currently available fluid temperature. In the above equations it is clear that fluid and solid temperatures at a point *P*, are

directly dependent on solid and fluid temperature, respectively, at that point, hence poor convergence. The partial elimination algorithm eliminates the coupling between the two phases directly. Again the solid temperature equations can be written in terms of discretized form as:

$$T_p^s = \frac{\sum A_{nb}^s T_{nb}^s + B^s + \lambda T_p^f}{(A_p^s + \lambda)} \dots\dots\dots (C-5)$$

This T_p^s expression can be used in fluid temperatures equation. Similarly T_p^f is as:

$$T_p^f = \frac{\sum A_{nb}^f T_{nb}^f + B^f + \lambda T_p^s}{(A_p^f + \lambda)} \dots\dots\dots (C-6)$$

The resulting equations for fluid and solid phases using partial elimination algorithm can be written as;

$$\left(A_p^f + \frac{\lambda}{\lambda + A_p^s} A_p^s \right) T_p^f = \sum A_{nb}^f T_{nb}^f + B^f + \frac{\lambda}{\lambda + A_p^s} (\sum A_{nb}^s T_{nb}^s + B^s) \dots\dots\dots(C-7)$$

$$\left(A_p^s + \frac{\lambda}{\lambda + A_p^f} A_p^f \right) T_p^s = \sum A_{nb}^s T_{nb}^s + B^s + \frac{\lambda}{\lambda + A_p^f} (\sum A_{nb}^f T_{nb}^f + B^f) \dots\dots\dots (C-8)$$

The final equations are solved using TDMA, which is already discussed in Appendix B.

Appendix D

Assessments of Computational Procedure

The numerical simulations for laminar flow conditions were carried out using effective viscosity equal to laminar viscosity, i.e., $\mu_{eff}=\mu_i$. In the numerical calculation procedure fluid flow in the cubic cavity, which is shown in Figure A11C-1, ($\rho=1 \text{ kg/m}^3$ and $\mu=0.01 \text{ kg/ms}$) was computed numerically using one of the two horizontal cavity walls moving with a constant velocity, 1 m/s (Reynolds number =100), which is also shown in Figure D1. All other walls were taken stationary, i.e., the velocity components of all other walls were zero. Our numerical model results were compared with the result computed using commercial software named FLUENT 6.0. Predicted variations of horizontal velocity components, u along the center vertical line, Y and vertical velocity component, v along the central horizontal line are shown in Figure D2 and D3. The center vertical line and the center horizontal lines are shown in Figure D1. Figures, D2 and D3 show that our model predictions have a good agreement with the computed results using FLUENT 6.0. It is also important to mention here that a grid independency test was carried out and results in the Figures D2 and D3 are grid independent.

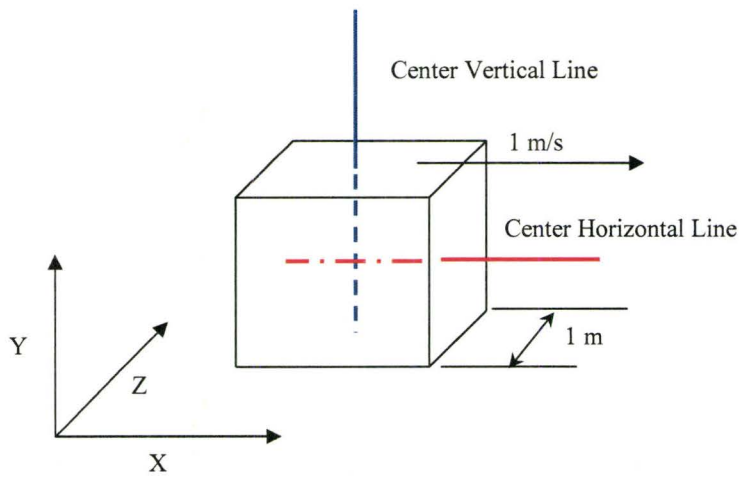


Figure D1: Cubic cavity ($a=1$ m) used for computational domain

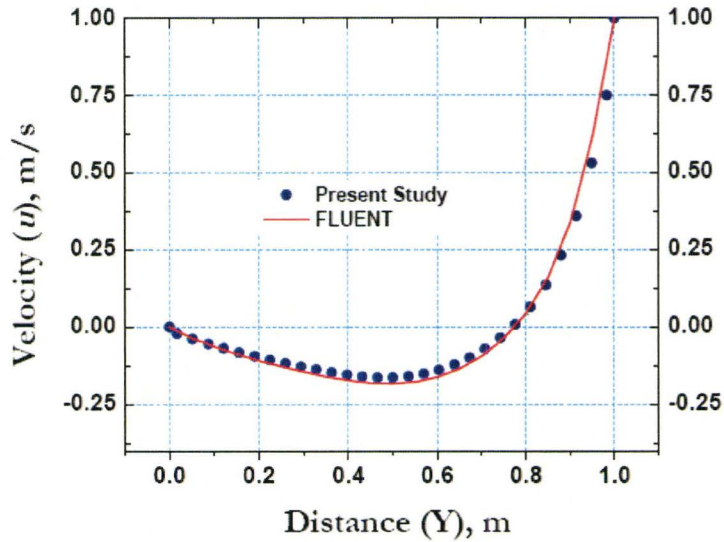


Figure D2: Comparison of present numerical predictions of horizontal velocity component, u , along the center vertical line, Y , with those computed by FLUENT for steady laminar flow in a cubic cavity

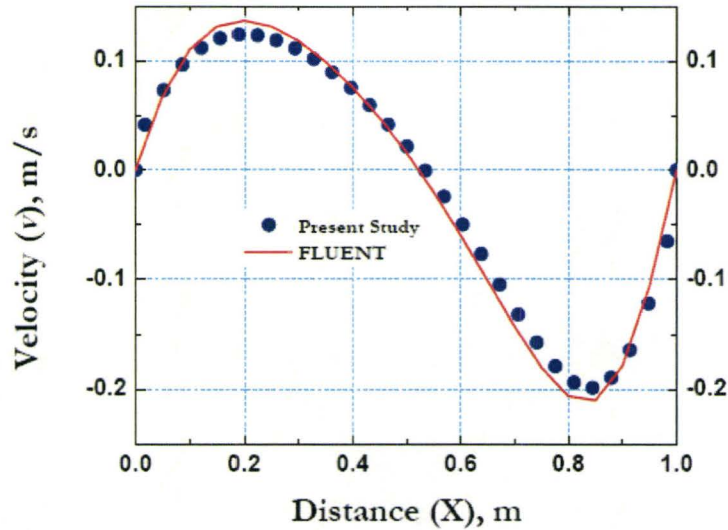


Figure D3: Comparison of present numerical predictions of vertical velocity component, v , along the center horizontal line, X , with those computed by FLUENT for steady laminar flow in a cubic cavity

Changing density from 1 kg/m^3 to 100 kg/m^3 (turbulent flow with Reynolds number 10^4) the aforementioned simulation were repeated for turbulent flow. Again, the predicted variations of horizontal velocity components, u along the center vertical line, Y are plotted in Figure D4. It is evident that our model can predict reasonably good compared to FLUENT in case of turbulent flow too.

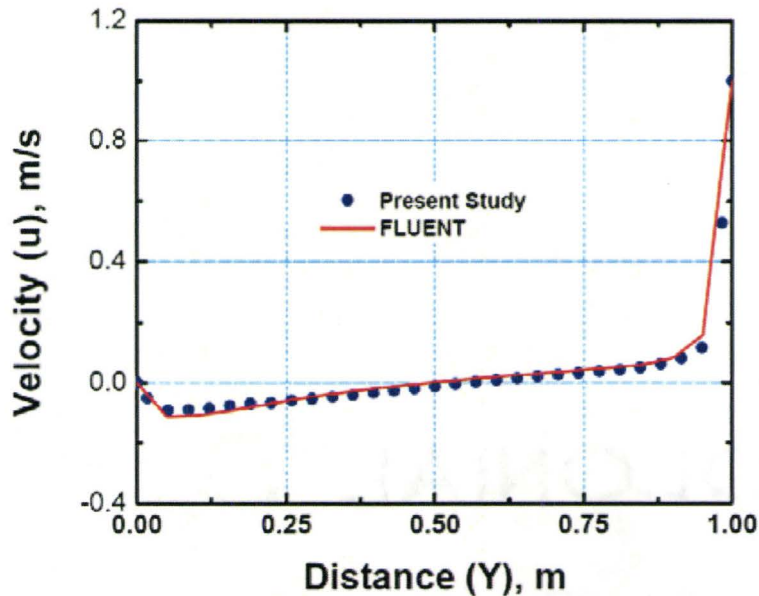


Figure D4: Comparison of present numerical predictions of horizontal velocity component, u , along the center vertical line, Y , with those computed by FLUENT 6.0 for steady turbulent flow in a cubic cavity

A natural convection simulation was also carried out with the present code, where two sides of a cube were fixed at $1000\text{ }^{\circ}\text{C}$. The other walls were taken in adiabatic conditions. The working fluid was considered such a way that the natural convective flow is inherently laminar. The properties of the fluid are listed in Table D1. Direct comparison of the calculated temperature with calculation using FLUENT is shown in Figure D5. A comparison of temperature along the central horizontal line is shown in Figure D6. It is evident that the present numerical modeling results and numerical simulation with FLUENT has good agreement.

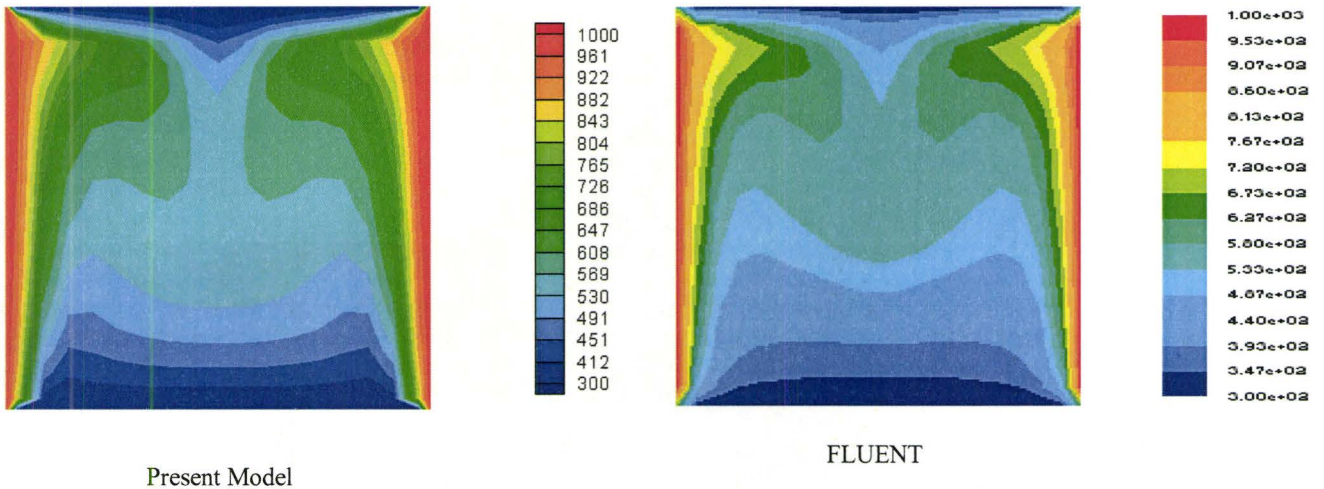


Figure D5: Calculated Temperature field from Present Model and FLUENT

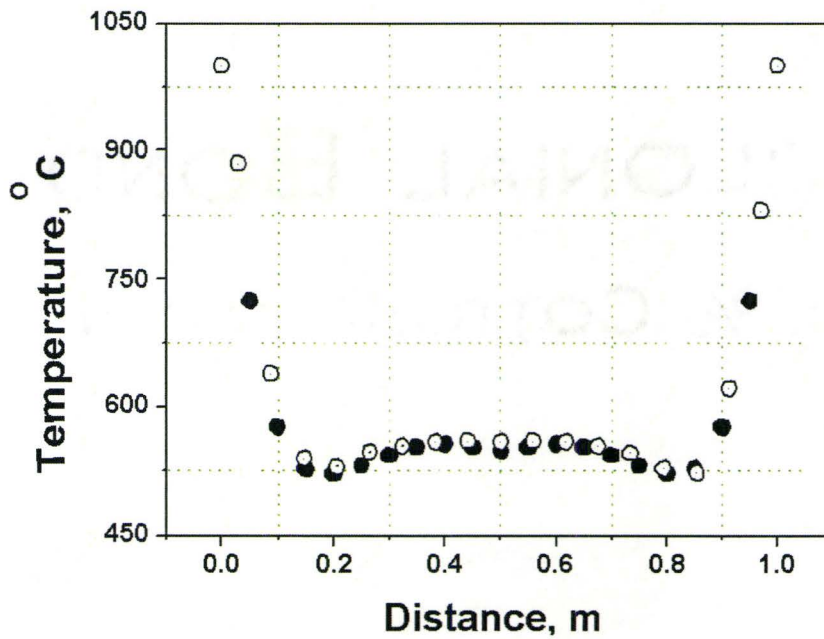


Figure D6: Central Horizontal Distance, X Vs Temperature

Table D1: Properties of working fluid for natural convection study

Density, $\rho = 1000 \text{ kg/m}^3$	Length of the cube, $L=1 \text{ m}$
Specific Heat, $C_p= 1.103e+4$	Rayleigh Number, $Ra=5e+5$
Viscosity, $\mu= 10^{-3} \text{ kg/ms}$	Prandtl Number, $Pr =0.71$
Thermal expansion coefficient, $\beta=10^{-5} \text{ 1/K}$	Gravity, $g=6.96e-5 \text{ m/s}^2$

References

Adolph H, Paul G, Klein K-H, Lepoutre E, Vuillermoz J C and Devaux M., 1989, *Iron and Steelmaker*, February, pp29-33

Al-Amiri A. M., 2002, *Numerical Heat Transfer, Part A*, V41, pp817-834

Alazmi B. and Vafai K., 2000, *Journal of Heat Transfer*, V122, pp303-326

Alazmi B. and Vafai K., 2004, *Journal of Heat Transfer*, V126, pp389-399

Amiri A. and Vafai K., 1994, *Int. Journal of Heat Mass Transfer*, V37, pp939-954

Amiri A., Vafai K. and Kuzay T. M., 1995, *Numerical Heat Transfer Part A*, V27, pp651-664

Amiri A. and Vafai K., 1998, *Int. Journal of Heat Mass Transfer*, V41, pp4259-4279

Argento C. and Bouvard D., 1996, *Int. Journal of Heat and Mass Transfer*, Vol 39, pp3175-3180

Babrauskas V. and Thureson P., 1994, *Fire and Materials*, V18, pp261-261

Baukal C. E., Lanyi M. D., and Winchester D.C., 1990, *I&SM*, October, pp51-56

Beckermann C., Viskanta R. and Ramadhyani S., 1986, *Numerical Heat Transfer*, V10, pp557-570

Benenati R. F. and Brosilow C. B., 1962, *AIChE*, V8(3), pp359-361

Bevers G. S. and Sparrow E., 1969, *Journal of Applied Mechanics*, V36, pp711-714

Byron Bird R., Stewart E. W. and Lightfoot N. E., 1994, *Transport Phenomena*, John Wiley and Sons, Singapore, New York, Chichester, Brisbane, Toronto

Brinkman H. C., 1947a, *Appl. Sci. Res.*, A1, pp27-34

Brinkman H. C., 1947b, *Appl. Sci. Res.*, A1, pp81-86

Camdali, U. and Tunc, M., 2002, *International Journal of Energy Research*, V26, pp935-947

Chandrasekher B. C. and Vortmeyer D., 1979, *Thermo Fluid Dynamics*, V12, pp105-111

Chen J. C. and Churchill S. W., 1963, *A.I.Ch.E., Journal*, Vol 9(1), pp 35-41

Chen H., Chen T. S. and Chen C. K., 1996, *International Journal of Heat and Mass Transfer*, V39, pp1157-1164

Chen X. B., Yu P., Winoto S. H. and Low H. T., 2007, *Numerical Heat Transfer: Part A*, V52, pp377-397

Clayton J., 1993, *Steel Technology International*, pp97-101

Cumberland, D. J. and Crawford, R. J., 1987, *The Packing of Particles*, 1st ed; Elsevier Science: Amsterdam, The Netherlands

Darcy, H., 1856, *Fontains Publiques de la Ville de Dijon*, Librairie des Coros Imperiaux des Ponts et Chaussees et des Mines, Paris

David E., Lauriat G. and Cheng P., 1991, *Journal of Heat Transfer*, V113, pp391-399

Demirel Y., Sharma R. N., AlAli H. H., 2000, *Int. Journal of Heat Mass Transfer*, V43, pp327-332

Dixon A. G. and Cresswell D. L., 1979, *AIChE*, V25, pp663-676

Durlofsky L. and Brady J. F., 1987, *Physics of Fluids*, V30, pp3329-3341

Elia M., McDonald T. and Crisp A., 1986, *Clinical Chimica Acta*, V158, pp237-244

Ergun S., 1952, *Chemical Engg Progress*, Vol 48, pp89-94

FactSage 5.5, 2007

FLUENT 6.0, Website: <http://www.fluent.com>

Forchheimer P., 1901, Wasserbewegung durch Boden, Zeits. Ver. Deutsch. Ing. V45, pp1782-1788

Francisco D. Rocamora Jr. and Marcelo J. S. De Lemos., 2000, *Int. Comm. Heat and Mass Transfer*, V27(6), pp825-834

Franklin J., 1991, *Iron & Steelmaker*, Vol 18, No 5, May, pp 57-58

Fruehan, 1998, *The Making, Shaping and Treating of Steel*, 11th Edition

Furnas C. C., 1932, U. S. Bureau of Mines Bulletin, 261

German, R. M., 1989, *Particle Packing Characteristics*, 1st ed; Metal Powder Industries Federation: Princeton, NJ

Ghosh A. and Chatterjee A., 2008, *Ironmaking and Steelmaking Theory and Practice*, Prentice Hall of India Private Limited, New Delhi

Greenkorn R. A., 1981, *AIChE*, V27, pp529-545

Guo D. and Irons G. A., 2005, *ICS Conference Proceedings*, PP441-448

Guo D. and Irons G. A., 2006, *AISTech Proceedings*, PP425-433

Hamdan M. H., 1994, *Applied Mathematics and Computation*, V62, pp203-222

Hassan K. and Mohamed S. A., 1970, Natural Convection from isothermal flat surfaces, *International Journal of Heat and Mass Transfer*, V13, pp1873-1886

Hassanizadeh S. M. and Gray W. G., 1987, *Transport Porous Media*, V2, pp521-531

Hong J. T., and Tien C. L., 1987, *Int. Journal of Heat Mass Transfer*, V30, pp143-150

Hsu C. T. and Cheng P., 1985, *Int. Journal of Heat Mass Transfer*, V28, pp683-697

Hsu C. T. and Cheng P., 1990, *Int. Journal of Heat Mass Transfer*, V33(8), pp1587-1597

[Http://snap.final.gov](http://snap.final.gov)

Hunt M. L. and Tien C. L., 1988a, *Int. Journal of Heat Mass Transfer*, V31, pp301-309

Hunt M. L. and Tien C. L., 1988b, *Journal of Heat Transfer*, V110, pp378-384

Hwang G. J., Wu C. C., and Chao C. H., 1995, *Journal of Heat Transfer*, V117, pp725-732

IISI, 2007, *World Steel in Figures*

Jamialahmadi M., Muller-Steinhagen H. and Izadpanah M. R., 2005, *Int. Journal of Heat and Fluid Flow*, V26, pp156-172

Janaf Thermochemical Tables, Third Edition, 1985

Jang J. Y. and Chen J. L., 1992, *International communication of Heat and Mass Transfer*, V19, pp263-273

Jones Jeremy A. T., 1994, *McMaster Symposium*, No 22, pp172-186

Kitaev B. I., Yaroshenko Y. G. and Suchkov V. D., 1968, *Heat Exchange in Shaft Furnace*, Pergamon Press, New York

Kladias N. and Prasad V., 1991, *Journal of Thermophysics*, 1991, V5, pp560-576

Lapwood E. R., 1948, *Proc. Cambridge Philos. Soc.*, V44, pp508-521

Launder B. E. and Spalding D. B., 1974, *Computer Methods in Applied Mechanics and Engineering*, V3, pp269-289

Lauriat G. and Prasad V., 1987, *Transactions of ASME*, V109, August, pp688-696

Li Y., and Fruehan R. J., 2003, *Met Trans B*, V34B, June, pp333-343

Lu J. D., Flamant G. and Variot B., 1994, *International Journal of Heat and Mass Transfer*, Vol 37, pp 727-736

Lundgren T. S., 1972, *J. Fluid Mech.*, V51, pp273-299

Nakano H., Uchida S. and Arita K., 1999, *Nippon Steel Technical Report*, Number 79, January, pp68-74

Nakayama A. and Kuwahara F., 1999, *ASME Journal of Fluid Engg*, V121, pp427-433

Mapelli, C. and Baragiola, S., 2006, *Ironmaking and Steelmaking*, V33, pp379-388

Martin H., 1978, *Chemical Engineering Science*, V33, pp913-919

Mathur P., and Daughtridge G., 1994, *McMaster Symposium*, No 22, pp121-127

Muller G. E., 1991, *Chemical Engineering Science*, V46, pp706-708

Nield D. A. and Bejan A., 1991, *Convection in Porous Media*, Springer, New York

Nield D. A. 2001, *Journal of Fluid Engineering*, V123, pp928-931

Nithiarasu P., Seetharamu K. N. and Sundararajan T., 1997, *International Journal of Heat and Mass Transfer*, V40(16), pp3955-3967

Pakdee W. and Rattanadecho P., 2006, *Applied Thermal Engineering*, V26, pp2316-2326

Patankar S. V., 1980, *Numerical heat Transfer and Fluid Flow*, Hemisphere publishing corporation, New York

Pedras M. H. J. and Lemos M. J. S. de, 2001a, *International Journal of Heat and Mass Transfer*, V44, pp1081-1093

Pedras M. H. J. and Lemos M. J. S. de, 2001b, *Journal of Fluid Engineering*, V123, pp941-947

Postelnicu A. and Rees D A S., 2003, *International Journal of Energy Research*, V27, pp961-973

Quintard M., Kaviany M. and Whitaker S., 1997, *Adv. Water Resources*, V20, pp77-94

Raptis A., 1998, *International Journal of Heat and Mass Transfer*, Vol 41, pp 2865-2866

Robert A. and Mazumdar D., 2001, *Steel Research*, V72 (3), pp97-105

Roblee L.H.S., Baird R. M. and Tierney J. W., 1958, *AIChE*, V4(4), pp460-464

Rodi W., 1980, *Turbulence models and their applications in hydraulics - A state of the art review*, University of Karlsruhe, Germany

Rosseland S, 1936, *Theoretical Astrophysics*, Oxford University Press, Cl; Arendon, England (1936)

Rudraiah N. and Srimani P. K., 1980, *Proc. Royal Soc London A*, V373, pp199-205

Rudraiah N. and Balachandra Rao S., 1983, *Applied Sci. Research*, V40(3), pp223

Rudzki E. M, Reinbold R. J. and B. K. Pease, 1973, *Journal of Metals*, February, pp38-44

Seddeek M. A., Darwish A. A. and Abdelmeguid M. S., 2007, *Communications in Nonlinear Science and Numerical simulation*, Vol 12, pp 195-213

Shifrin V., Popenov A., Coudurier L. and M. Devaux, 2001, *Steel Times*, September, pp281-282

Sozen M. and Vafai K., 1990, *International Journal of Heat and Mass Transfer*, V33, pp1247-1261

Spalding D. B., 1980, *Recent Advances in Numerical Methods in Fluids*, V1, pp 139-169

Steel Statistical Yearbook, International Iron and Steel Institute, 2007, <http://www.worldsteel.org>

Szekely J., 1988, *Met Trans B*, V19B, August, pp525-540

Talukdar P., Mishra S. C., Trimis D. and Durst F., 2004, *International Journal of Heat and Mass Transfer*, Vol 47, pp 1001-1013

Tang X., Kirschen M., Abel M. and Pfeifer H., 2003, *Steel Research*, V74, No 3, pp201-210

TECPLOT, Version 9.0

Teoh L L, 1989, *Ironmaking and Steelmaking*, Vol 16, pp303-313

The Making, Shaping and Treating of Steel, 11th Edition, 1998

Thomson M. J., Kournetas N. G., Evenson E., Sommerville I. D., McLean A. and J. Guerard, 2001, *Ironmaking and Steelmaking*, Vol 28, No 3, pp266-272

Turkdogan E. T., 196, *Fundamentals of Steelmaking*, The Institute of Materials, London

Vafai K., 1984, *J Fluid Mechanics*, V147, pp233-259

Vafai K., Alkire R. L, and Tien C. L., 1986, *Journal of Heat Transfer*, V107, pp642-647

Vafai K., Bejan A., Minkowycz W. J., and Khanafer K., *Handbook of Numerical Heat Transfer*, Second Edition, Chap. 12, pp. 389-416, John Wiley & Sons Inc., Hoboken, NJ, (2006).

Vafai K. and Tien C. L., 1981, *International Journal of Heat and Mass Transfer*, V24, pp195-204

Vafai K. and Etefagh J., 1988, *Journal of Heat Transfer*, V 110, pp1011-1014

Vafai K. and Amiri A., 1998, *Transport Phenomena in Porous Media*, D. B. Ingham and I. pop, eds, Pergamon, England, pp313-329

Vallomy J. A., 1994, *52nd Electric Furnace Conference; Nashville, TN; USA;* 13-16 Nov. 1994. pp. 255-263

Versteeg H. K. and Malalasekera W., 2007, *An Introduction to Computational Fluid Dynamics - The Finite Volume Method*, Pearson Education Limited, Harlow

Vortmeyer D., 1978, *Proceedings of Sixth International Heat Transfer Conference*, Toronto, V 6, pp 525-539

Wakao N., Kaguei S. and Funazkri T., 1979, *Chemical Engineering Science*, V 34, pp325-336

Weber J. E., 1975, *International Journal of Heat and Mass Transfer*, V18, pp569-573

Wells M B. and Vonesh F. A., 1986, *Iron and Steelmaker*, November 1986, pp13-22

World Steel in Figures, International Iron and Steel Institute, 2007, <http://www.worldsteel.org>

www.postech.ac.kr/dept/mse/cml/Eng/flowchart1.htm

www.steeluniversity.org

Yagi S. and Kunni D., 1960, *AIChE*, V6, pp97-104

Yoshida H., Yun J. H. and Echigo R., 1990, *International Journal of Heat and Mass Transfer*, Vol 33, pp 847-857

Yee S. S. and Kamiuto K., 2005, *Journal of Porous Media*, Vol 8(5), pp 481-492

Yong Y. S, Howell J. R. and Klein D. E., 1983: *Journal of Heat Transfer*, V 105, pp 325-332

Yu W. S., Lin H. T. and Lu C. S., 1991, *International Journal of Heat and Mass Transfer*, V34(11), pp2859-2868